ABSTRACT

SILICON-GERMANIUM NANOWIRE HETEROJUNCTIONS:
OPTICAL AND ELECTRICAL PROPERTIES

by
Xiaolu Wang

Semiconductor nanowires are quasi-one-dimensional objects with unique physical properties and strong potential in nanophotonics, nanoelectronics, biosensing, and solar cell devices. The next challenge in the development of nanowire functional structures is the nanowire axial heterojunctions, especially lattice mismatched heterojunctions. Si and Ge have a considerable lattice mismatch of ~ 4.2% as well as a mismatch in the coefficient of thermal expansion, and the formation of a $Si_{1-x}Ge_x$ transition layer at the heterointerface creates a non-uniform strain and modifies the band structures of the adjacent Si and Ge nanowire segments. These nanostructures are produced by catalytic chemical vapor deposition employing vapor-liquid-solid mechanism on (111) oriented p-type Si substrate, and they exhibit unique structural properties including highly localized strain, and short-range interdiffusion/intermixing revealed by transmission electron microscopy, scanning electron microscopy and energy dispersive x-ray spectroscopy. Our studies of the structural properties of axial Si-Ge nanowire heterojunctions show that despite the 4.2% lattice mismatch between Si and Ge they can be grown without a significant density of structural defects. The lattice mismatch induced strain is partially relieved due to spontaneous SiGe intermixing at the heterointerface during growth and lateral expansion of the Ge segment of the nanowire, which is in part due to a higher solubility of Ge in metal precursors. The mismatch in Ge and Si coefficients of thermal expansion and low thermal conductivity of Si/Ge nanowire heterojunctions are proposed

to be responsible for the thermally induced mechanical stress detected under intense laser radiation.

The performed electrical measurements include current-voltage，conductance-voltage, transient electrical measurements under various applied voltages at temperatures ranging from 20 to 400K. We find that Si-Ge nanowire heterojunctions exhibit strong current instabilities associated with flicker noise and damped oscillations with frequencies close to 10-30 MHz. Flicker (or $1/f$) noise is characterized and analyzed on carrier number fluctuation model and mobility fluctuation model noise mechanism, respectively. The proposed explanation is based on a carrier transport mechanism involving electron transitions from Ge to Si segments of the NWs, which requires momentum scattering, causes electron deceleration at the Ge-Si heterointerface and disrupts current flow. Both Si/Ge heterojunctions and NW surface states are demonstrated to be the two dominant elements that strongly influence the electrical characteristics of nanowires.

SILICON-GERMANIUM NANOWIRE HETEROJUNCTIONS:
OPTICAL AND ELECTRICAL PROPERTIES

by
Xiaolu Wang

A Dissertation
Submitted to the Faculty of
New Jersey Institute of Technology
in Partial Fulfillment of the Requirements for the Degree of
Doctor of Philosophy in Electrical Engineering

Helen and John C. Hartmann Department of Electrical and Computer Engineering

January 2017

APPROVAL PAGE

SILICON-GERMANIUM NANOWIRE HETEROJUNCTIONS:
OPTICAL AND ELECTRICAL PROPERTIES

Xiaolu Wang

Dr. Leonid Tsybeskov, Dissertation Advisor	Date
Professor of Electrical and Computer Engineering, NJIT	

Dr. Haim Grebel, Committee Member	Date
Professor of Electrical and Computer Engineering, NJIT	

Dr. Somenath Mitra, Committee Member	Date
Distinguished Professor of Chemistry, NJIT	

Dr. Hieu Pham Trung Nguyen, Committee Member	Date
Assistant Professor of Electrical and Computer Engineering, NJIT	

Dr. Dong-Kyun Ko, Committee Member	Date
Assistant Professor of Electrical and Computer Engineering, NJIT	

BIOGRAPHICAL SKETCH

Author: Xiaolu Wang

Degree: Doctor of Philosophy

Date: January 2017

Undergraduate and Graduate Education:

- Doctor of Philosophy in Electrical Engineering,
  New Jersey Institute of Technology, Newark, NJ, 2017

- Master of Science in Electrical Engineering,
  New Jersey Institute of Technology, Newark, NJ, 2011

- Bachelor of Science in Microelectronics,
  Jiangnan University, Wuxi, P. R. China, 2008

Major: Electrical Engineering

Presentations and Publications:

X. Wang, L. Tsybeskov, T. I. Kamins, X. Wu, and D. J. Lockwood, "Structural and optical properties of axial silicon-germanium nanowire heterojunctions." Journal of Applied Physics, 118, 234301, 2015.

L. Tsybeskov, S. A. Mala, X. Wang, J-M. Baribeau, X. Wu, and D. J. Lockwood, "Inelastic light scattering spectroscopy in Si/SiGe nanostructures: Strain, chemical composition and thermal properties." Solid State Communications, 245, 25, 2016.

D. J. Lockwood, X. Wu, J-M. Baribeau, S. A. Mala, X. Wang, and L. Tsybeskov, "Si/SiGe heterointerfaces in one-, two-, and three-dimensional nanostructures: their impact on SiGe light emission." Frontiers in Materials, 3, 12, 2016.

D. J. Lockwood, X. Wu, J-M. Baribeau, S. A. Mala, X. Wang, and L. Tsybeskov, "Si/SiGe interfaces in three-, two-, and one-dimensional nanostructures and their influence on SiGe light emission." ECS Transactions, 72, 7, 2016

D. J. Lockwood, X. Wu, J-M. Baribeau, S. A. Mala, X. Wang, and L. Tsybeskov, "Si/SiGe Heterointerfaces in one-, two-, and three-dimensional nanostructures: their effect on SiGe light emission." ECS Transactions, 75, 77, 2016.

D. J. Lockwood, X. Wu, J-M. Baribeau, S. A. Mala, X. Wang, and L. Tsybeskov, "Si/SiGe interfaces in three-, two-, and one-dimensional nanostructures and their influence on SiGe light emission." In Meeting Abstracts of The Electrochemical Society, San Diego, CA, 42, 2096, 2016.

X. Wang, L. Tsybeskov, D. J. Lockwood, X. Wu, and T. I. Kamins, "Strain and stress in axial silicon-germanium nanowire heterojunctions." Material Research Society Symposium, Session S11 (9), December, 2015.

X. Wang, L. Tsybeskov, T. I. Kamins, X. Wu, and D. J. Lockwood, "Laser-induced thermal stress in axial silicon-germanium nanowire heterojunctions." Material Research Society Symposium, Session P1 (3), December, 2015.

X. Wang, L. Tsybeskov, T. I. Kamins, X. Wu, and D. J. Lockwood, "Carrier transport in axial germanium-silicon nanowire heterojunctions: localization, noise and oscillations." Submitted to Journal of Applied Physics.

X. Wang, L. Tsybeskov, S. Mala, T. I. Kamins, X. Wu and D. J. Lockwood, "Silicon-germanium nanowire heterojunctions: raman scattering and photoluminescence." Material Research Society Proceedings, Boston, MA, November 2014.

X. Wang, L. Tsybeskov, T. I. Kamins, X. Wu, and D. J. Lockwood, "Strain and stress in axial silicon-germanium nanowire heterojunctions." Dana Knox Student Research Showcase, New Jersey Institute of Technology, Newark, NJ, April 2016.

To my parents and godparents
感谢我的父亲王俊，母亲胡可儿，义父姚舒拉，
义母徐金凤，多年来给我无条件的爱和教育。

ACKNOWLEDGMENT

I would like to express my genuine gratitude to my dissertation advisor, Dr. Leonid Tsybeskov who have cared for, supported, and helped me all along my voyage of Ph.D. studies with a contagious positive attitude. It is also him who made every single step of our research at full throttle with his highly erudition. I am proud of him as his student and sincerely hope that he would be proud of me some day.

I would give my sincere appreciation to my academic advisor, Dr. Durgamadhab Misra. He brought me into the area of semiconductor characterization.

I would like to thank my committee members who gave me valuable suggestions during the research with their fruitful discussions, Dr. Haim Grebel, Dr. Somenath Mitra, Dr. Hieu Pham Trung Nguyen, and Dr. Dong-Kyun Ko.

I would like to express my gratitude to Dr. David J. Lockwood, Dr. Xiaohua Wu and Dr. Jean-Mark Baribeau for our valuable collaboration. I thank G. Parent for TEM sample preparation. I thank NSF, Hewlett-Packard Laboratories and the Foundation at NJIT for continuous financial support. I thank The Louis Berger Group, Inc. for sponsorship by awarding me the Dr. Louis Berger Memorial Endowed International Fellowship. I would also like thank my friend and colleague, Dr. Selina A. Mala.

Finally, I want to express my gratefulness to my parents and godparents for their endless love and support.

TABLE OF CONTENTS

TABLE OF CONTENTS
(Continued)

LIST OF TABLES

LIST OF FIGURES

CHAPTER 1

INTRODUCTION

Semiconductor nanowires (NWs) are quasi-one-dimensional nanoscale objects with unique electronic, photonic, thermal, electrochemical and mechanical properties. Different fabrication techniques were demonstrated but the most promising approach is based on "bottom-up" growth mechanisms with control of the NW morphology, stoichiometry, and crystal structure. This work is focused on NW based heterojunctions (HJs), more specifically Si/Ge NW HJ grown on Si substrates. Why Si/Ge NW HJs? Germanium (Ge) is a group IV semiconductor with the room temperature fundamental indirect bandgap of 0.66 eV and a direct bandgap of 0.8 eV (~ 1.55 µm) with only 0.14 eV separation energy. These properties make Ge one of the most promising materials for CMOS compatible photonic components including near-infra-red photodetectors [1-4] and, possibly, lasers [5-7] in the important spectral region of 1.3-1.6 µm. However, it is well known that conventional Ge hetero-epitaxy on Silicon (Si) is complicated by the 4.2% difference in Ge and Si lattice constants [8, 9]. Various techniques for building quality Si/Ge heterojunctions (HJs) include multi-step annealing to relax Ge layers and reduce the dislocation density [10, 11], growth of ultra-thin Ge films and superlattices using $Si_{1-x}Ge_x$ alloy transition layers with graded Ge composition x [8, 11-14] and three-dimensional (3D) growth in the form of SiGe clusters and cluster multi-layers using the Stranski-Krastanov (S-K) growth mode [15-18]. Another promising approach is to use one-dimensional (1D) growth in the form of nanowires (NWs) produced by the Vapor-Liquid-Solid (VLS) growth mode or similar techniques [19-22]. These axial Si/Ge NW HJs with the heterointerfaces

perpendicular to the NW axes have a reduced heterointerface area compared to radial or "core-shell" NW HJs, where the Si/Ge heterointerfaces are parallel to the NW axes [22-24]. Since Ge has a larger lattice constant (5.658 Å) compared to Si (5.431 Å), it was theoretically predicted that in axial Ge-Si NW HJs, strain created by the lattice mismatch can be partially relieved by a lateral expansion of a Ge segment of the NW and strain relaxation can be achieved without formation of structural defects [25, 26].

It is well known, that at the Si/Ge heterointerface electron mobility decreases due to the electron deceleration and, possibly, accumulation at the hetero-interface. At the same time, electrons and holes have high mobilities in Ge than in Si, so introducing a $Si_{1-x}Ge_x$ alloy layer offer an interesting opportunity for the development of novel electron transfer devices with a lower value of off-current [27] and faster switching time [28]. Also, there are several limiting factors in homogeneous NW devices and planar devices that can be mitigated by using NW heterostructures [27]. In addition, Si/Ge NW HJ based devices are promising due to the energy barriers built in the Si-Ge heterointerfaces, enhanced carrier injection efficiency, and improved carrier mobility due to compressive strain and controlled Ge composition [29]. The quality of the junctions between two materials is critical for many applications, such as NW resonant tunneling diodes [30] and NW single electron transistors [31], where defect-free tunnel barriers are essential for device performance. The NW structure, shape, composition, local strain, and interface states near the Si-Ge heterointerface do affect the NW heterojunction physical and chemical properties and device performance.

The specific aim of this work is fabrication and studies of Si/Ge NW HJs and their applications in electron-transfer device (ETD) prototypes. More specifically, it was

experimentally demonstrated that Au-assisted VLS growth is capable of producing high crystallinity, constant diameter Si/Ge NW HJs with defect free heterointerface, and the predicted lateral expansion of the Ge NW segments was found to be as high as 10% [32]. This large lateral expansion is, in part, due to a higher solubility of Ge in Au, compared to that of Si, and it provides additional relaxation of strain associated with the lattice mismatch. Also, the VLS-grown axial Si/Ge NW HJs have less than 10 nm thick spontaneously formed $Si_{1-x}Ge_x$ alloy layer. This result is very different compared to traditional Ge heteroepitaxy on Si, which requires precisely grown composition-controlled $Si_{1-x}Ge_x$ alloy layers with more than 100 times greater thicknesses. These properties make Si/Ge axial NW HJs very interesting, if not unique, lattice-mismatched hetero-systems, and their structural and optical properties are studied in details.

The project has a long history. In 2007, Dr. Tsybeskov's team started discussions with HP Labs and NRC Canada on feasibility of the development of axial Si/Ge NWs. From 2007 to 2009, first series of samples are produced. However, Si/Ge NW HJs were not well defined, and HJ electronic properties were controlled by structural imperfections. In 2009, after modifications in the growth procedure, the Si/Ge NW HJs were successfully grown by our collaborators at HP Labs and TEM data confirmed low-defect density and abruptness of the Si/Ge NW HJs. From 2009 to 2011, sample fabrication was optimized and our team has started systematic investigation of optical and electrical properties of the Si/Ge NW HJs. The main motivation of this work is demonstration of a novel ETD prototype. Compared to traditional III-V multi-valley semiconductor based ETDs, where electron transfer involves transitions between different valleys of the conduction energy band, a similar effect involving electron transfer between Si and Ge conduction band

minima is expected in the Si/Ge NW HJs. This approach could lead to the development of cost efficient compact oscillators. However, the major obstacle is the potentially high density of surface/interface trap levels [33, 34]. These surface states are known not only to trap charge carriers but also to enhance the surface conductivity in various field effect based devices [35, 36]. Therefore, studies of Si/Ge NW HJ based ETD prototypes should involve ac and dc electrical measurements at various temperatures and detailed analysis of current noise within a broad frequency range.

Chapter 2 introduces the fabrication procedure and structure of our Si/Ge NW HJ samples. Further discussion about the anticipated physical properties of these structures as well as detailed references to previously published results focusing on structural, optical, electrical and thermal properties of Si/Ge HJs are presented in this chapter.

Chapter 3 describes the details of sample characterization techniques used in the present work. The experimental methods, optical/electrical characterization setups, and details of the measurement procedures are presented.

Chapter 4 presents a detailed discussion of the experimental results. The first section is focused on structural properties of Si/Ge NW HJs based on Transmission Electron Microscopy (TEM), Scanning Electron Microscopy (SEM), and Energy-Dispersive X-ray (EDX) spectroscopy measurements. (These measurements are performed in collaboration with scientists from National Research Council of Canada in Montreal). The result shows that despite the 4.2% lattice mismatch between Si and Ge, the NJI HJs can be grown without a significant density of structural defects. Detailed studies of the optical properties of axial Si/Ge NW HJs are shown in second section of this chapter. Raman scattering and photoluminescence (PL) measurements are performed for Si/Ge

NWs using different excitation wavelengths, broad temperature range, and angles of excitations. We find that the lattice mismatch induced strain is partially relieved due to spontaneous SiGe intermixing at the heterointerface during growth and lateral expansion of the Ge segment of the nanowire. The mismatch in Ge and Si coefficients of thermal expansion (CsTE) and low thermal conductivity of Si/Ge NW HJs are proposed to be responsible for the thermally induced stress detected under intense laser radiation in PL and Raman scattering measurements. The last part of Chapter 4 is focused on Si-Ge NW HJ electrical properties and explanations of the non-linear current voltage characteristics and strong current instabilities associated with flicker noise and damped oscillations with frequencies close to 10-30 MHz. The proposed explanation is based on a carrier transport mechanism involving electron transitions from Ge to Si segments of the NWs, which requires momentum scattering, causes electron deceleration and localization at the Ge-Si heterointerface and disrupts current flow.

In Chapter 5, this dissertation ends with a summary of the presented research and proposed future work.

CHAPTER 2

BACKGROUND

Semiconductor NWs usually (but not always) are crystalline quasi-1D nanostructures (compared to quantum wells described as two-dimensional (2D) and quantum dots as 3D nanostructures). They offer unique access to low dimensional physics and have been regarded as important elements of the next-generation technology. NW based devices could achieve very high device integration densities compared to conventional devices and structures. Silicon based NWs are especially attractive due to the current dominant role of Si in the semiconductor industry. Interesting properties and applications of elemental semiconductor NW have been widely reported [37]. Introduction of semiconductor heterojunctions within NWs opens additional possibilities compare to the traditional 2D semiconductor interfaces formed in thin film quantum wells and superlattices. For example, Si/Ge HJ NWs exhibit unique structural, optical, thermal and electrical properties, which could be adjusted and improved with control over the materials composition, geometry and dimensions. Similar to that in planar Si/Ge heteroepitaxy, the Si/Ge NW heterojunction design allows engineering of the energy bandgap, carrier mobility, density of states, phonon and electron confinement, and exciton binding energy. Because of these, high-performance Si/Ge NW HJs, has become an intriguing and exciting approach in quasi-one dimensional nanostructures [38].

2.1   Growth of Si/Ge NWs

Advances are continuously made in synthesis of growth mechanisms for semiconductor NWs in the past decade, but there are still many problems to solve. Using the gas phase or solution phase synthetic routes is enabled to improve the crystalline and chemical properties and control access to a variety of new material systems and morphologies [39]. Those NW synthesis methodologies developed during the past decade can be categorized into Top-down approach and Bottom-up approach [40]. Top-down approach builds NWs from pre-existing substrate materials by techniques such as lithography and etching. The bottom-up approach, which will be focus on in this study, allows to grow a semiconductor NW on any substrate at low temperatures. However, these techniques constitute serious challenges in the location of the nanowires and compatibility with CMOS components [41]. Various versions of Si/Ge HJs have been previously studied, and it was demonstrated that these nanostructures can be reliable and reproducibly fabricated using annealing to relax the Ge layer, two-dimensional (2D) growth (i.e., thin films) using $Si_{1-x}Ge_x$ alloy transition buffer layers with graded Ge composition x, 3D growth in the form of $Si_{1-x}Ge_x$ clusters using the S-K growth mode [42-46], etc. The most-cited and widely-accepted method for NW fabrication is the VLS growth reported in the first generation of 1D nanostructures by Wagner and Ellis in 1964 during studies of single-crystalline whiskers [47].

2.1.1   Vapor Liquid Solid Growth

VLS growth is a classic 1D structure growth mechanism. The growth rate depending on the diameter of the structure, which is several orders of magnitude higher in one direction than in others. The synthesis is based on Chemical Vapor Deposition (CVD). In the growth of Si and Ge semiconductors, the widely demonstrated efficient catalyst is gold. Although

Au remains the most commonly used catalyst for Si and Ge NWs, other metals (e.g., Au,

Ti, Ga, Pt, Al, Cu, Pd, Mn, and Fe) have been used to catalytically enhance growth of the

NWs. Furthermore, due to the physical properties of Si and Ge, SiGe NW alloys and SiGe

NW heterojunctions can be produced with the specific physical properties and applications.

However, it requires strict control over the SiGe alloy and NW segment compositions.
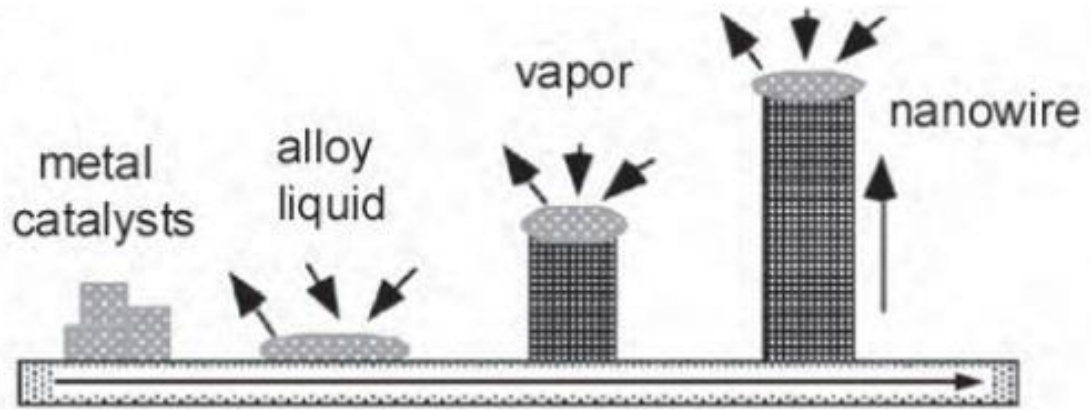
Figure 2.1 Schematic of the fundamental processes during the vapor-liquid-solid growth
of element semiconductor NWs.
Source: [48].

The anisotropic crystal growth in the VLS mechanism is promoted by the presence

of the liquid alloy/solid interface [48, 55]. The VLS mechanism of pure Si NWs is depicted

in Figure 2.1 and it includes four growth stages:

I. Sputtering or thermal evaporation is used for depositing a thin metal (Au) film (~1–
    10 nm) onto a wafer substrate (Si).

II. Au/Si alloy droplets are created on the wafer surface (the thinner the metal film, the
    smaller the droplets), after the wafer is annealed at temperatures higher than the
    metal-semiconductor (Au/Si) eutectic point. The growth temperature is set in
    between the eutectic point and the melting point of the materials. Si NWs are
    synthesized via the VLS process. Because Si/Au and Ge/Au eutectic temperature is
    ~360-370°C much lower than those of the silicide.

III.   The liquid Au/Si alloy droplets on the surface of the substrate act as a catalyst and preferred locations for the adsorbing and decompensating the gaseous precursor. Crystalline Si nanowires grown takes place in a vacuum deposition system by a liquid droplet catalyzed CVD process. Metal-semiconductor droplets on the surface of the substrate correspond to lower the activation energy of normal vapor-solid growth. Furthermore, the increasing surface area-to-volume ratio leading to lower melting points considerably in those nanometer-sized metal-semiconductor droplets [94].

IV.   When the Au/Si alloy droplets are saturated with the Si atoms, the precipitation at the liquid/solid interface and the NW formation occur. Because much higher melting point of semiconductor compared to that of the eutectic alloy leading to saturation and nucleation at the liquid/solid interface for axial crystal growth. At the liquid-alloy/solid-semiconductor interface, and the liquid-alloy droplet rises from the surface and semiconductor atoms sedimentation.

VLS growth by CVD can produce epitaxially aligned, highly crystalline wires. The diameter of the as-synthesized wires can be controlled by selecting different size drops of the catalyst. Although VLS method is the ideal synthetic technique to control NW growth [48, 49], thin metal films do not provide a good NW diameter control due to the randomness of the film breakup at reaction temperatures[50, 51]. Precise growth and epitaxial alignment has only been achieved by lithographically defined regions in NWs growth by thin film evaporation[52-54]. On the other hand, catalyst material is getting incorporated into the NWs. Au in Si and Ge produces deep traps, and it decreases carrier mobility and lifetime. Au is also a contamination for CMOS technology [40].
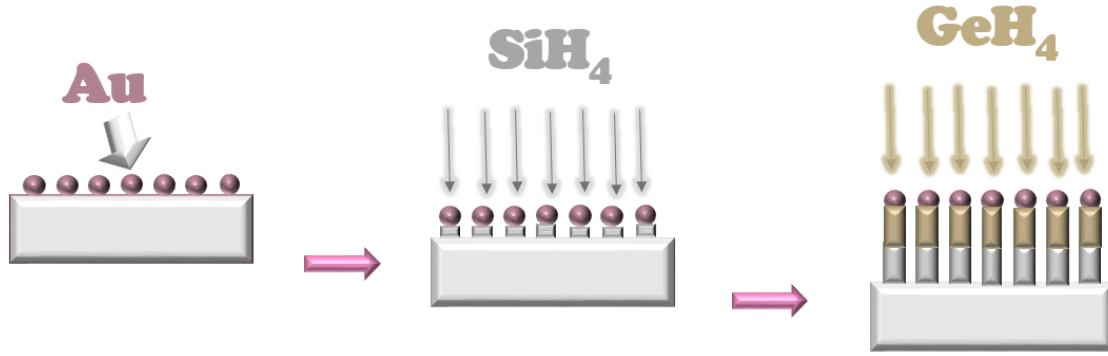
Figure 2.2 Schematic illustration of Si/Ge NWs growth from the reaction of SiH_4 and GeH_4 vapor phases. This reaction is catalyzed by Au/Si and Au/Ge droplet.

2.1.2 Samples Fabrication

In this study, our axial Si/Ge NW HJs samples are grown using the VLS technique (see Figure 2.2) and Au nanoparticles as a precursor in a reduced pressure, lamp heated CVD reactor using the following growth steps [55]:

I.   The growth of Si/Ge NW is using gold as catalyst. Because the proportions and temperatures of the eutectic metal/semiconductor alloy needed are approximately the same for Au/Si and Au/Ge (80 and 70% Au, 360°C). A thin layer of Au (2 nm thick) is deposited on a cleaned, p-type (111) Si substrate with a resistivity of 0.01–0.02 Ω·cm and annealed for 10 min at 670 ℃ at 95 Torr in a H_2 ambient to form nanometer-size clusters. For details, see Ref. [56].

II. The Si segments of the NWs are grown at 680 ℃ at 30 Torr using the gaseous precursors SiH_4 and HCl in a H_2 ambient. The growth rate for the Si NW segment is estimated to be close to 100 nm per minute [same above ref].

III. The reactor is cooled to 350 ℃ at a nominal rate of 75 ℃/min with the SiH_4-HCl-H_2 mixture flowing.

IV. The Ge segments of the NWs are grown at 350 ℃ and 90 Torr, using GeH_4 and HCl as the gaseous precursors in the H_2 ambient. The growth rate for the Ge NW segment is estimated to be 40 nm per minute[57].

V.   To avoid sample oxidation, before samples are exposed to air the reactor is cooled down to room temperature. We find that most of the studied Si/Ge NW HJ samples have a NW diameter ranging from 50 to 130 nm. The total NW length is 1500–2000 nm with the Ge segment as long as 500 nm.

Our grown NW sample is depicted qualitatively in Figure 2.3. Our sample's structural properties have been characterized by TEM, SEM, EDX, PL spectroscopy and Raman scattering spectroscopy.
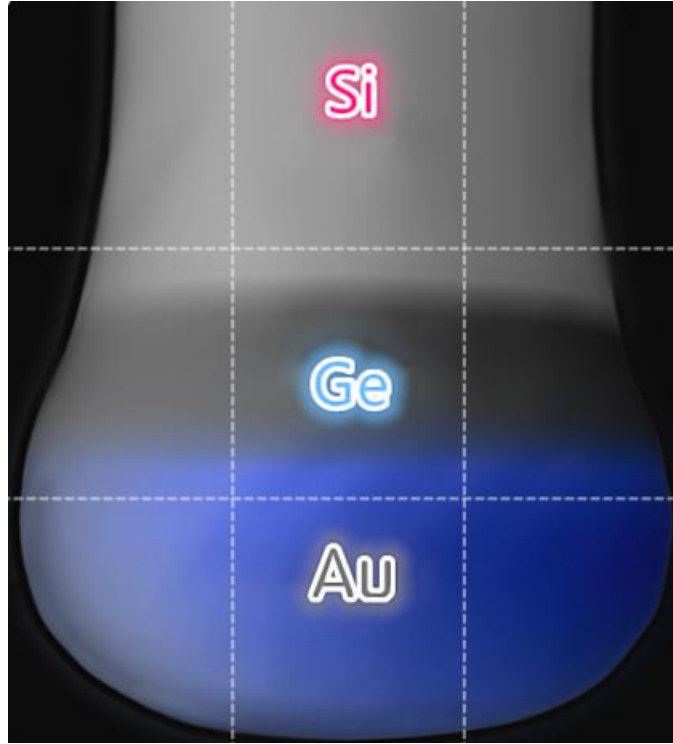
Figure 2.3 Schematic depicting our grown NW sample.

2.2   Properties of Si/Ge NW HJs

Si and Ge have the same diamond lattice structure and similar lattice constants. These properties of Si and Ge physics make it possible to be fully miscible and synthesize a wide union of composition alloys as well as a variety of structures using $Si_{1-x}Ge_x$ alloys. Some specific electronic and optoelectronic properties of their alloys can be reached by adjusting concentration and bandgap engineering, etc. Epitaxial layers of epi-grown Si/Ge crystalline material largely improve the applications in optoelectronics and photovoltaics. For example, in strained Ge layers on Si lasing at ~1.6um has been reported [5-7]. In unstrained

Ge layers on Si, ~1.55 um electroluminescence was found to be due to the direct transition [5-7]. Therefore, the structural, electronic, optical, and thermal properties of Si/Ge NW HJs are of significant interests and will be reviewed in this section.

2.2.1 Structural Properties

Si/Ge NWs offer the possibility to manipulate the physical properties by changing the dimension of the system and engineering the geometry of the Si/Ge interface. Fortunately due to the lateral relaxation of the strain deriving from the ∼4.2% lattice mismatch, NWs with defect-free interfaces can be obtained. But the large value ∼4.2% lattice mismatch between Si and Ge made the growth of defect-free 2D-interfaces challenging in previous reported synthesized Si/Ge NWs [58]. The interfaces between two materials are expected to be as abrupt as possible. However, in all previous reported Si/ $Si_{1-x}Ge_x$ axial junctions in nanowires [58, 59], the interfaces were very diffuse with smooth interface from one to another, rising serious concerning at the efficiency of the envisioned devices.
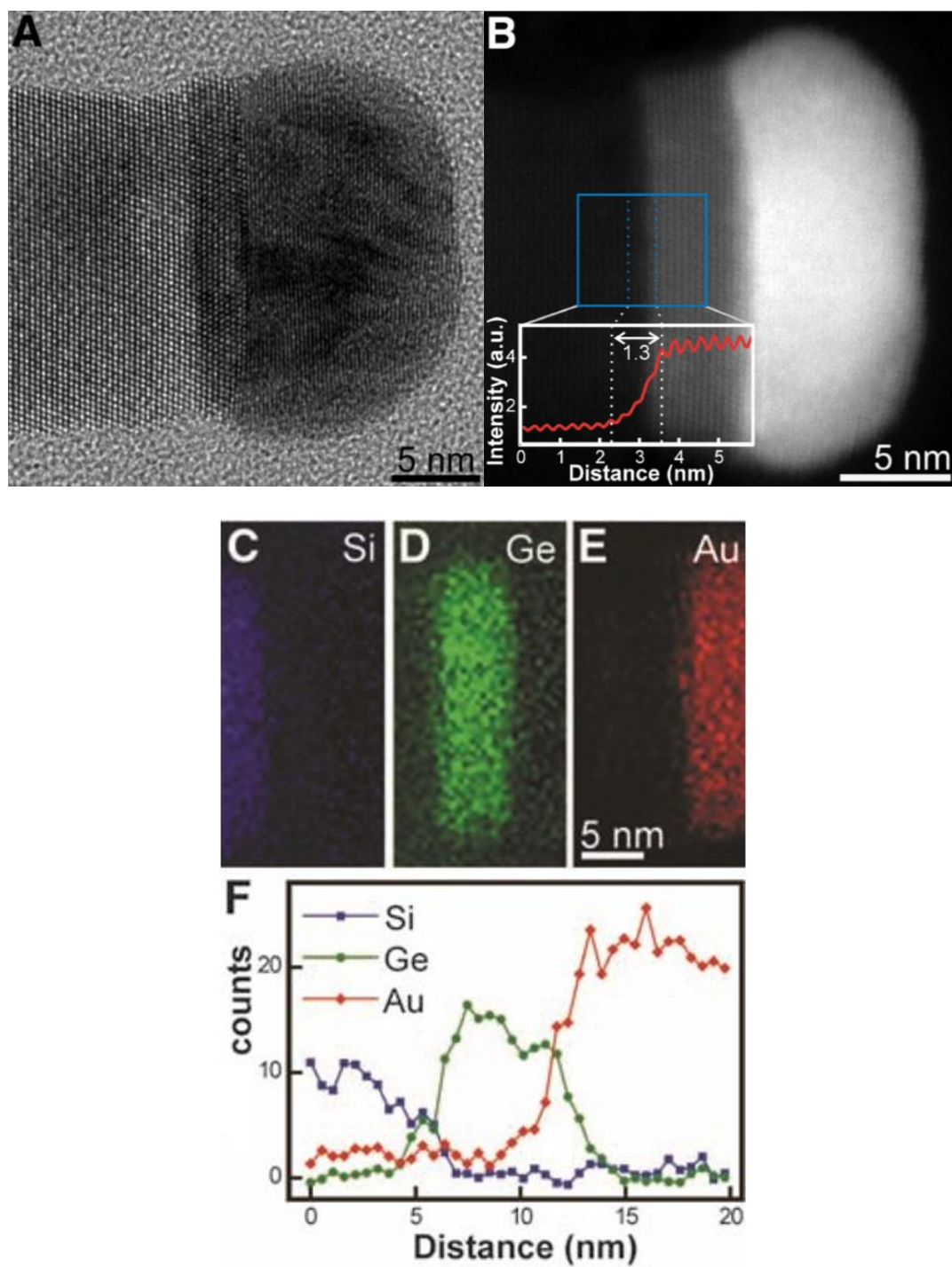
Figure 2.4 (A) HR-TEM image of a Si/Ge NW HJ. (B) HAADF-STEM image of a similar wire grown under the same conditions. The inset shows the intensity profile across the interface. (C) false-color STEM EDS elemental maps of Si, (D) Ge, and (E) Au in the region of the junction in a nanowire. (F) Line profile of the EDX intensities extracted from the elemental maps of Si, Ge, and Au. The intensity is averaged over a 3-nm strip along the midpoint of the wire.
Source: [60].

Figure 2.4 proves that the composition of NWs heterostructure changes along the growth direction of the wire. The structural properties and the compositional abruptness of the Si/Ge axial NW interface are quantified in Figure 2.4 [60]. A highly crystalline structure without obvious structural defects such as dislocations is verified in the high-resolution TEM (HR-TEM) image of the interface of the Si/Ge NW HJ (Figure 2.4(A)). High Angle Annular Dark Field (HAADF) in scanning TEM (HAADF –STEM) in Figure 2.4(B) confirms a compositionally uniform Ge segment is on the Si nanowire. The inset image (Figure 2.4(B), inset) shows a smooth but narrow transition at the interface and the width of the $Si_{1-x}Ge_x$ transition layer is 1.3 nm. EDX maps and line profiles (Figure 2.4) show that Si and Ge diffuse into each other in the composition transition layer formed in less than 2 nm, is consistent with the HAADF analysis.

The formation of high crystallinity, compositionally abrupt and structurally perfect junctions in axial heterostructure NWs are the prerequisite for future transistor applications such as tunnel field-effect transistors, photonic and thermoelectric devices. EDX spectroscopy is critical for us to completely gauge the possibility sharpness from Si to Ge may with small reservoir effect by measuring the widths of the interfaces in the growth direction.

So in our study, EDX spectroscopy is used as the privileged tool to characterize the crystalline structure and the local atomic composition of Si/Ge NWs HJs, apart from the above measurement techniques (SEM, TEM). In order to predict and tailor the electronic and optical properties for desired applications, structure characterization of Si/Ge NWs HJs are further analyzed by other optical techniques such as Raman scattering and PL spectroscopy.

2.2.2 Heterostructure Interfaces Strain

The 2-D semiconductor interface is ubiquitous in optoelectronic devices such as diodes, lasers, and transistors [61, 62]. The interface is troubled by the formation of structure defects such as dislocations (Figure 2.5(a)) due to the 4.2% lattice mismatch between pure Si and Ge. For Si/Ge interface, the onset thickness of relaxation must be greater than the critical thickness [63-66]. Critical thickness in terms of the mechanical equilibrium of a preexisting threading dislocation [65, 66] allows a mismatch between the alloy and the Si be accommodated elastically without misfit dislocations formed [67]. But the heterostructure would be considerably strained due to the mismatch if it is accommodated elastically [68] and if the thickness of the epitaxial layers is kept below a critical thickness. Relaxed, unstrained $Si_{1-x}Ge_x$ layers are only obtained at large layer thicknesses if they are deposited directly on a Si substrate. Thinner layers are biaxially strained. Relaxed layers with low dislocation densities are obtained by applying graded buffer layers [69, 70].
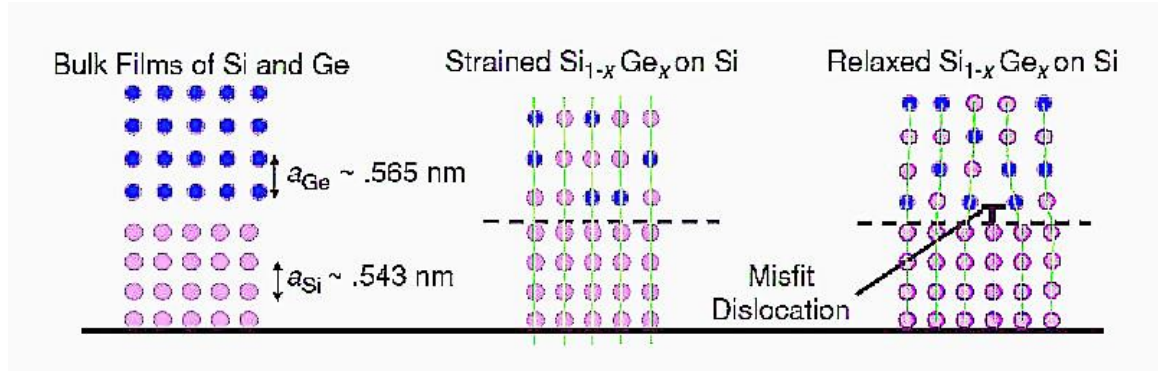
(a)
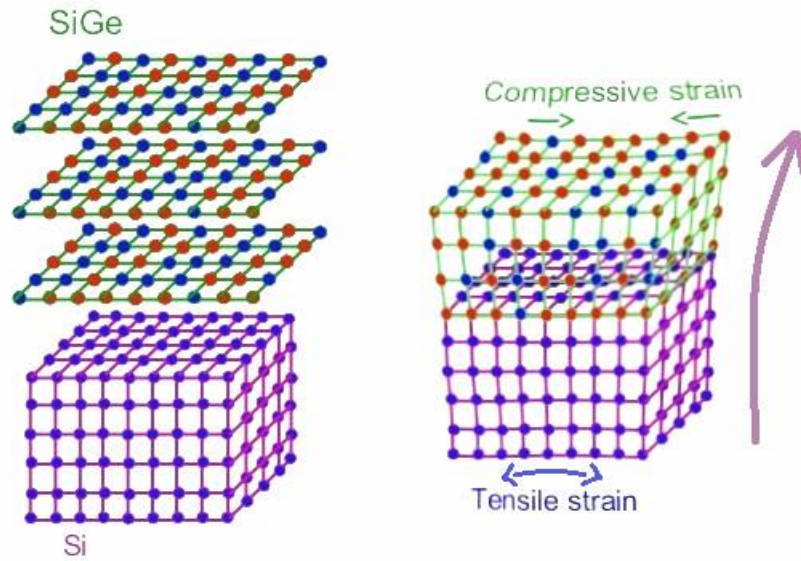
(b)

Figure 2.5 Relationship between lattice mismatch of Si and Ge and misfit dislocations that occur beyond the critical thickness (a) in film epitaxial layers. (b) in Si/Ge nanowires. *Source: [69].*

However, remarkably defect-free interface can be obtained in nanowires [38, 65, 66, 71], which is achieved by the lateral relaxation of the strain building up at the junction (Figure 2.5(b)). Since Ge has a larger lattice constant (5.658 Å) compared to Si (5.431 Å),

the lattice constant increases continuously as the Ge concentration in the $Si_{1-x}Ge_x$ alloy increases from a = 0.5431 nm (x=0) to a = 0.5658 nm (x=1) [72]. This is a small, negative deviation of the monotonically varying experimental data of the lattice constant from Vegard's law [73]. Crystalline silicon-germanium is reported to build a continuous substitutional solid solution with a cubic diamond structure (space group Fd3m) under normal pressure [74]. For silicon-germanium growth on a silicon, when the thickness less than the critical thickness this introduces compressive strain in the newly formed $Si_{1-x}Ge_x$ layer. (Figure 2.5(b)). For the thickness far exceeds the critical thickness of Ge on Si, the Ge is relaxed at growth temperatures. The compressive strain should be introduced to Ge part when these two materials are joined together leaving tensile strain in $Si_{1-x}Ge_x$ layer below Ge (Figure 2.5(b)). The resulting strain in Si is tensile. It was proposed that in axial Si/Ge NW HJs strain created by the lattice mismatch between Si and Ge can partially be relieved at the heterointerface by the lateral expansion of a Ge segment of the NW due to larger Ge lattice constant compared with Si. This relaxation by Ge atoms is the reason of the resulting defect-free interfaces. In addition, strain relaxation in a heteroepitaxial layer is also strongly influenced with solid solubility, interdiffusion, segregation, and generation of defects [121]. The present strain is induced by the misfit of lattice constant and the deference of CTE between Si and Ge when cooling from the growth temperature. Independent of the source of thermal effects or lattice mismatch induced strain, the overall effects on the band structure are equivalent.

Furthermore, since altering the intrinsic interatomic distances leads to modification of the energy levels, the band structure, mobility, the effective mass of electrons and holes, the valence bands split and Δ valleys are strongly affected by strain. For all these reasons

the strain would act as a powerful tool to modulate features of NW HJs in the device engineering.

2.2.2.1 Effect of Strain on Band Structure. Ge forms a covalent bond with Si. Ge is a Group IV material as well as Si, and thus avoids the cross contamination issue [75]. One property of Ge and Si that is the particular interesting nature of their bandgap. Ge has 3d electrons in the core, which is the significant different from Si. So, the main differences in the band structure between Si and Ge appear mainly in the conduction band arrangement. Si has the Γ_{15} band lower than the Γ_2 band and different lowest conduction bands ordering from Ge. Although both for Si and Ge, the maxima of the valence bands and the minimum of the conduction band lie at different momenta, the conduction band minimum in Ge occurs at the L-point along <111> direction of the Brillion zone, while it is near the X-point in Si. It means Ge has a direct bandgap Γ_1 of 0.80 eV ($\sim 1.55\,\mu$m) that is only 140 meV above its indirect bandgap at room temperature (Figure 2.5 (b)) [76]. Silicon has a much larger difference between its minimum bandgap of 1.12 eV at the **Δ**-valley along the <100> direction and its direct bandgap of 4.0 eV with another L-valley minimum at 2.06 eV (Figure 2.6(a)). The equivalent **Δ**-valley in Ge is above its direct bandgap at 0.8 eV. The band structure of Ge enables it transform from an indirect gap material to a direct gap material by introducing the incorporation of tensile strain (in opposite shift direction of Figure 2.6(c)). In addition, the configurations of valence band in both Si and Ge are similar.
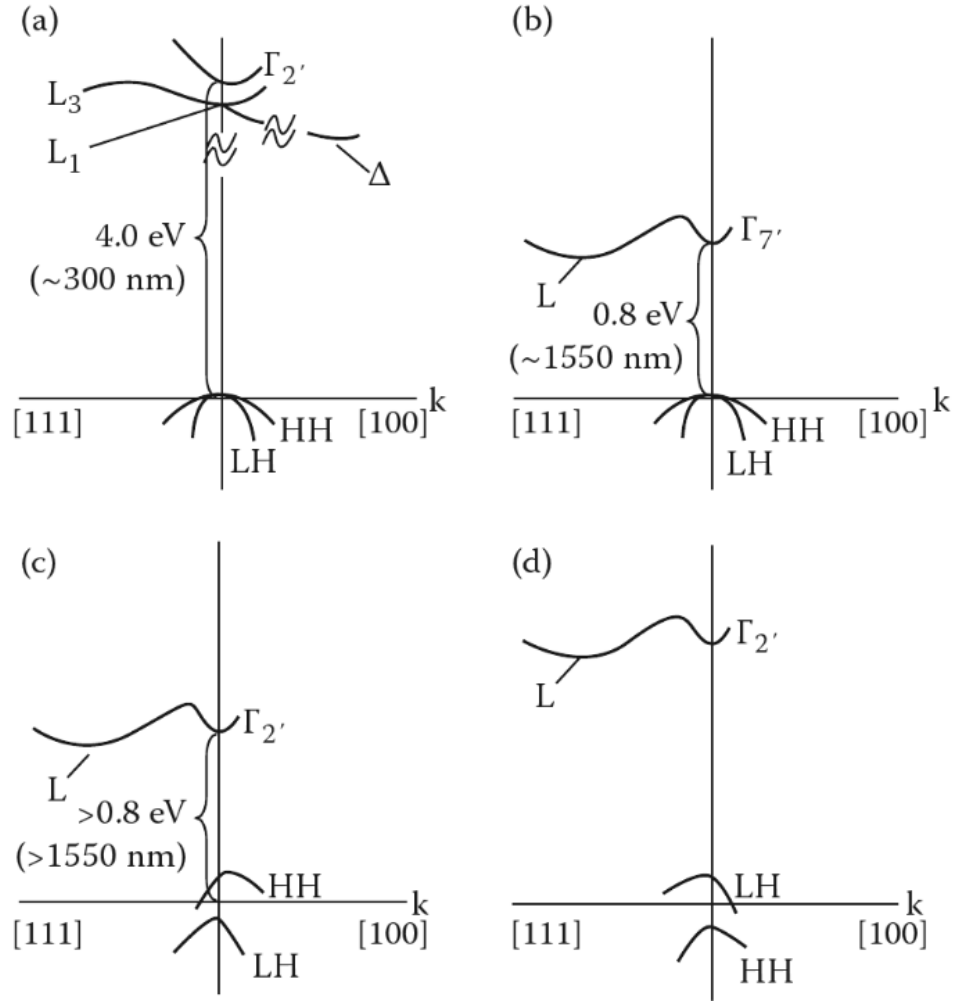
Figure 2.6 The bulk unstrained band structure of (a) Si, (b) Ge, (c) the shift with compressive strain on Ge, (d) the shift with tensile strain on SiGe.
Source: [77].

The strain relaxed $Si_{1-x}Ge_x$ alloy layer induce global strain for tensile strained Si and compressive strained Ge. For tensile strain decreases the direct bandgap and raises the degeneracy of the light and heavy hole bands with shifting the light hole up and heavy hole down in energy. In the opposite, compressive strain increase the direct bandgap and shifting the light hole down and heavy hole up. Figure 2.6 illustrates the band structures of Si, Ge and Ge/SiGe with and without compressive and tensile strain [77].

19

However, after cooling to room temperature, tensile strain, can be formed in the Ge layers due to the different temperature dependent CsTE of Ge compared with Si [78-80]. As the wafer is cooled from the growth temperature, Si has the smaller CTE than Ge leaving to a greater expansion than the Ge. Ishikawa et al. reported that 0.2-0.3% tensile strain would decrease the Γ-point transition energy by 0.03 eV [81], while Liu et al. reported reducing the disparity between the direct and indirect bandgaps of Ge from 136 to 100 meV makes direct band-gap red-shift from 0.8 down to 0.76eV and from an indirect gap to a direct gap material with ~1.8% tensile strain[82, 83].

Figure 2.7 illustrates a schematic view of band structure of Ge part of nanowires unstrained and shifted by tensile strain. With the increase of tensile strain, the energy difference between the direct and indirect bandgaps of Ge weakens transforming Ge from an indirect gap material to a direct gap material. With tensile strain, the direct gap shrinks faster than the indirect bandgaps. In addition, the light hole band effective mass reduces the average density of states in the valence band. Because light hole band determines the top of the valence band due to tensile strain. As a result, this small effective mass further decreases the threshold for optical transparency and lasing.
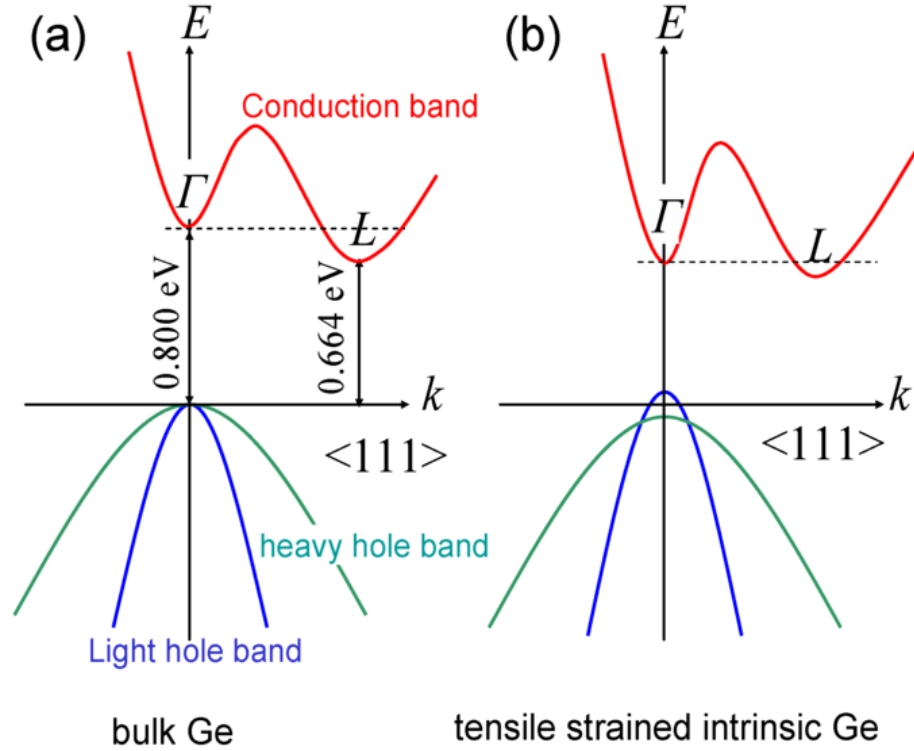
Figure 2.7 (a) A schematic view of band structure of bulk Ge, (b) tensile strained Ge with shifts towards direct bandgaps.
Source: [83].

In general, strain induced two effects are hydrostatic strain shifts the energy position of bands and uniaxial/biaxial strain splits degenerate bands. Figure 2.8 shows two strain affect both overall energies and shape of the band structure of Si. The hydrostatic strain upshift or downshift all conduction and valence bands (tensile lowers conduction bands and raise valence bands, and for compressive strain is just the opposite). However, the uniaxial stress only breaks the degeneracy of the valence bands but not change the conduction bands position as well as the total band energy. The valence band splits in heavy hole, light hole, and spin-orbit-split hole bands while the Δ bands split into four equivalent in-plane valleys and two growth direction valleys. The biaxial strain might decrease or increase the bandgap energy associated with the Δ valley due to the combined conduction

band structure and the bandgap energy associated with the L or Γ valley (increase with compressive and decrease with tensile biaxial strain).
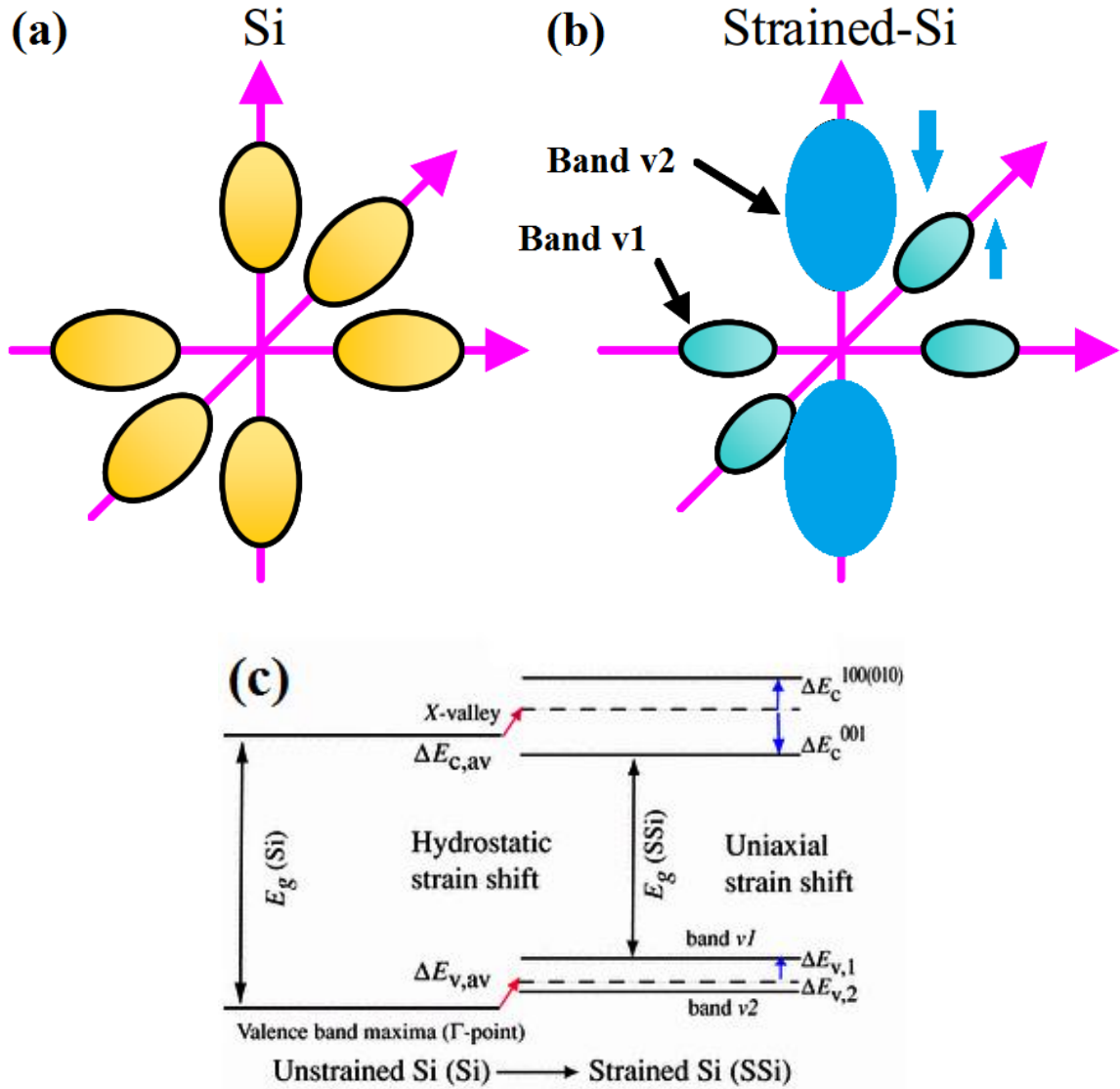
Figure 2.8 (a) A schematic view of bulk Si energy valleys and (b) the difference between the bulk Si and strained Si, (c) the hydrostatic shift and uniaxial splitting of the conduction and valence bands for both compressive and tensile strain.
Source: [84, 85].

For $Si_{1-x}Ge_x$ alloys of all compositions x are indirect bandgap semiconductors. Figure 2.9 illustrates the bandgap variation of $Si_{1-x}Ge_x$ alloys on Si with different Ge

content x. It clearly indicates that the bandgap variation is strongly affected by strain in the Si$_{1-x}$Ge$_x$ crystal. The lower two curves corresponds to the variation of strained Si$_{1-x}$Ge$_x$ alloys. The strain introduces heavy-hole/light-hole splitting of the valence band maximum. An example of valence band dispersion under strain along [100] and [110] for Si$_{0.5}$Ge$_{0.5}$ on Si(001) is depicted in Figure 2.12(b). Besides on the composition, an additional shift of the critical point energies is obtained by strain [84, 85].

Previous studies [72] show E$_1$ and E$_1$+Δ_1 interband transitions are most sensitive to strain and compostion, where E$_1$ denotes a direct transition between conduction band and valence bands, while E$_1$+Δ_1 is the spin-orbit split. For example, the dependence of E$_1$ and E$_1$+Δ_1 on a biaxial (100) strain ε_s is show in shifts [86] [87]:

$$\delta E_1 = E_1(\varepsilon_s) - E_1(0) = \frac{\Delta_1}{2} + E_H - \frac{1}{2}\sqrt{\Delta_1^2 + 4E_s^2} \qquad (2.1)$$

$$\delta(E_1 + \Delta_1) = [E_1 + \Delta_1](\varepsilon_s) - [E_1 + \Delta_1](0) \qquad (2.2)$$

$$= \frac{-\Delta_1}{2} + E_H + \frac{1}{2}\sqrt{\Delta_1^2 + 4E_s^2}$$

where E$_H$ is the hydrostatic shift due to hydrostatic strain and E$_s$ is possible splitting due to uniaxial shear, respectively.
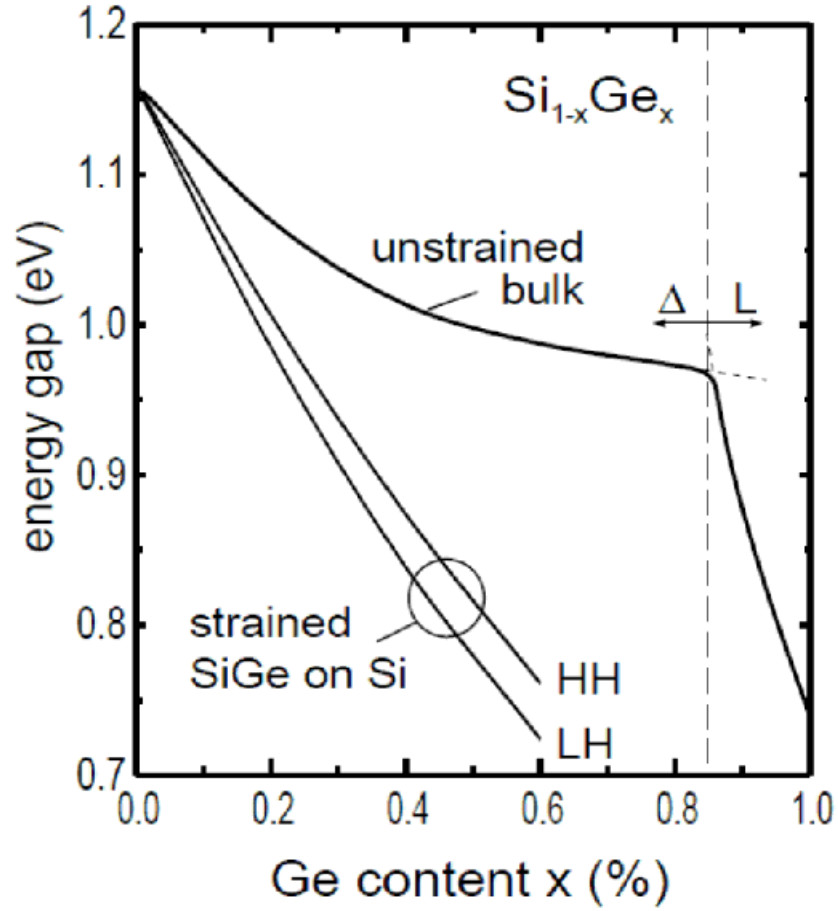
Figure 2.9 Energy bandgap variation of $Si_{1-x}Ge_x$ alloys on Si with different Ge content x.
Source: [88, 89].

2.2.2.2 Effect of Strain on Band Discontinuity. The electrical properties of the Si/Ge

NW HJs are determined by the energy band alignment at the heterointerface. When Si and

Ge form a HJ, discontinuities are created in their valence bands as well as conduction bands

due to the charge distribution near the HJ interface.

The Si/SiGe heterointerface exhibits type II energy band alignment where the

spatial separation of electrons in Si and holes in SiGe (see Figure 2.10) seems to make

carrier radiative recombination very inefficient. Figure 2.10 shows the band lineups of

Si/Ge, Si/ $Si_{1-x}Ge_x$, and $Si_{1-x}Ge_x$/Ge heterointerface with lower energy L-valley and Δ_2,

Δ_4 included. According to the large lattice mismatch and the conduction-band minima in Si and Ge are located at different points away from the Brillouin zone center, band offset is depicted in Figure 2.10(a). Figure 2.10(b) illustrates computed qualitatively analyzing the type-II staggered band alignment of tensile strained Si on compressive strained Ge [90]. However, despite the type-II band alignment, strain makes it still possible to obtain an efficient carrier radiative recombination in favorable conditions. A type-II conduction band edge alignment in Si/Ge NW HJs is proved [72]. This type II band offset of strained Si on relaxed $Si_{1-x}Ge_x$ leads to a potential well in the conduction band. However, the conduction band offset in contrast is learned to be relatively small for $Si/Si_{1-x}Ge_x$ interface (Figure 2.10(c)) [90]. The bandgap difference ΔEg between the Si part and the $Si_{1-x}Ge_x$ layer consists of the valence band discontinuity ΔEv plus the conduction band discontinuity ΔEc. In case of the Si/Ge HJs, most of the bandgap reduction on account of the shift in the valence band-edge since the conduction band edges for Si and SiGe nearly align. The valence-band discontinuity determines the capacitance and threshold voltage of microelectronic devices. The conduction band discontinuity accounts for a low proportion of the total bandgap difference. The calculated value of the conduction band offset ΔE_C, produced by strain but not including the effects of confinement, is 0.45x [91]. Experimental values of ΔE_C is few, and are somewhat larger [92]. For example, Stern and Laux [93] found ΔE_C= 0.18 eV for x = 0.3. The valence-band discontinuity between Si and $Si_{1-x}Ge_x$ is reported as $\Delta Ev = 6.4x$ meV where x is the Ge percent for $0 < x < 17.5\%$. A likely linear dependence is obtained when combining several research groups in Figure 2.11.
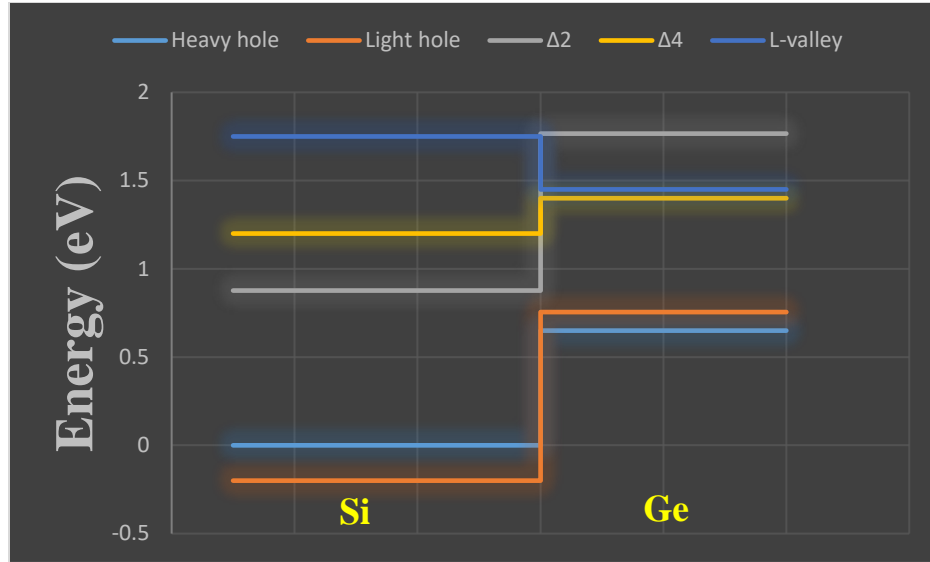
(a)

(b)
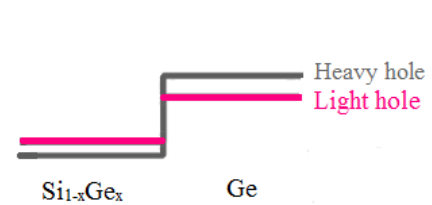
(c)

Figure 2.10 Band lineups of (a) Si/Ge heterostructure, (b) Si/Si$_{1-x}$Ge$_x$ heterostructure, and (c) Si$_{1-x}$Ge$_x$/Ge heterostructure.
Source: [90].
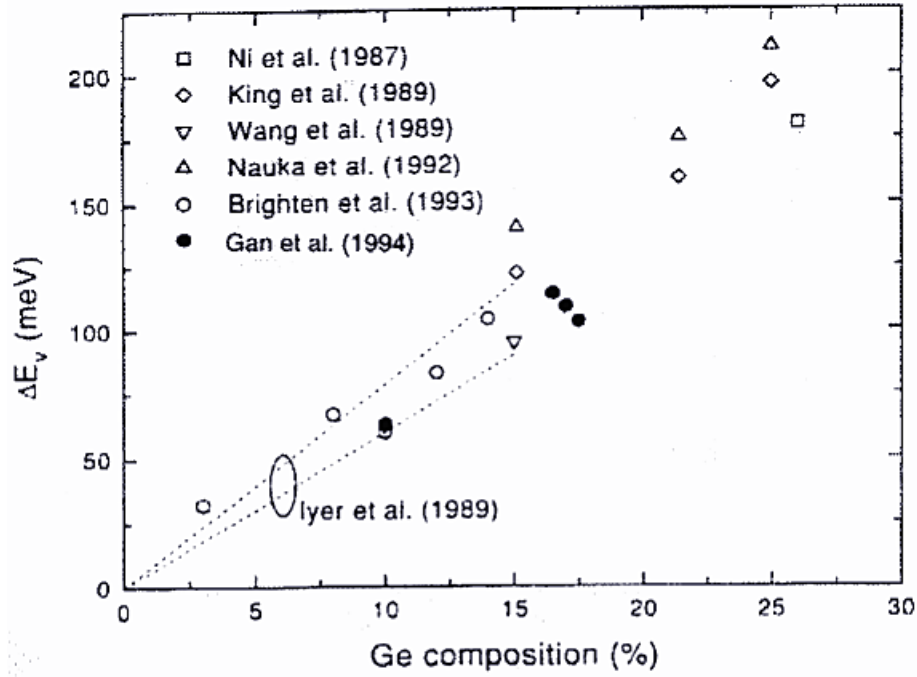
Figure 2.11 Valence-band discontinuity versus Ge composition for $Si_{1-x}Ge_x$ on Si.
Source: [94-96].

In sum, strained Si and Ge are attractive candidates from the perspective of electronic and optoelectronic devices. The research on this strain and ab initio calculations of Si/Ge NWs has been vivid starting from 20 years ago [97-100].
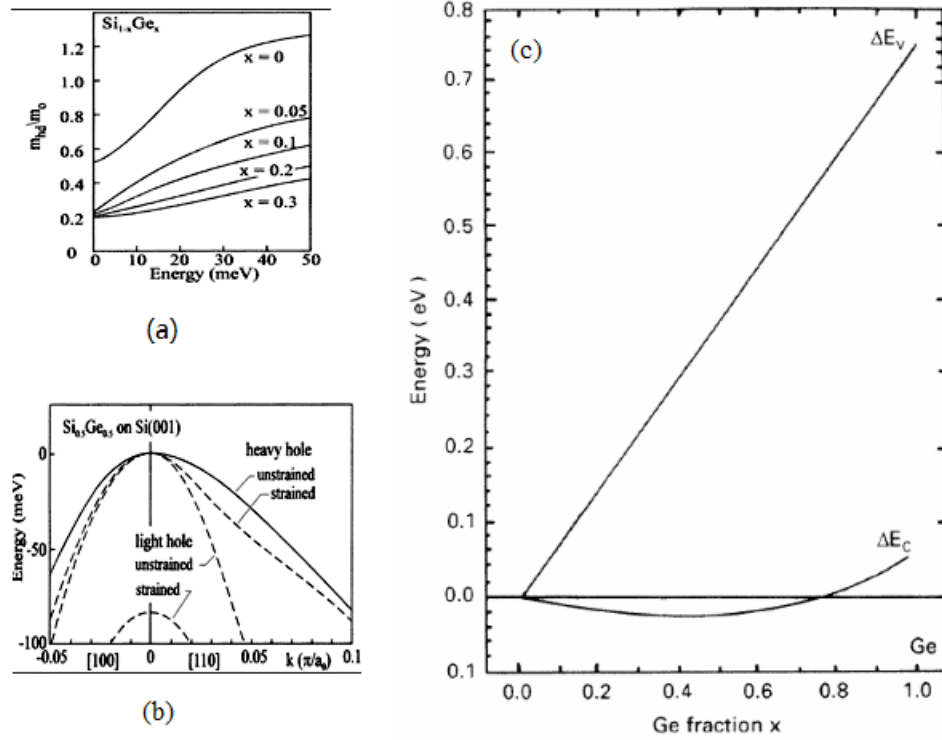
Figure 2.12 (a) Heavy hole effective mass density of states vs. energy at different x. (b) Valence band dispersion along [100] and [110] for $Si_{0.5}Ge_{0.5}$ on Si(001). (schematic view).(c) Valence and conduction band offsets for strained $Si_{1-x}Ge_x$ layers on (100) Si. *Source: [101-103].*

2.2.2.3 Effect of Strain on Effective Mass. According to the above discussion, heavy hole effective mass density of states of $Si_{1-x}Ge_x$ decreases with the increase of Ge composition x (Figure 2.12(a)). The shift of the L and H bands induced by strain results a steep change in the electron effective mass of conduction band [104]. Thus variation of effective mass must take changes of m^* into calculation when interpreting room-temperature carrier mobility data.

The corresponding relationships between effective masses and effective densities of states Nc and Nv are inseperate. Angular dependent calculations of effective masses under strain in Si/Ge HJs are anisotropic. In the other word, the density of states will be different in one crystal orientation than in another. In the calculation of density of states,

the effective mass is the geometric mean of a single band minimum described by a longitudinal mass and two transverse masses. Because the anisotropic density of states is more difficult to visualize and calculate than the isotropic density of states, methods are adjusted through calculating the densities of states from particular points or directions, or calculating the projected density of states. The strain dependent effective density of states in the conduction band Nc for the [110] SiNW is calculated from [105]:

$$N_c = \sqrt{\frac{2kT}{\pi\hbar}} \sum_{i=1}^{N} e^{E_{c\,min} - E_{i}/kT} \sqrt{m_i^*}, \tag{2.3}$$

where m_i^* is the effective mass of subband i. E_i and $E_{c\,min}$ are the bottom of subband i and the lowest conduction subband. kT are thermal energy 26 meV at T=300 K and N is the number of subbands in the 3kT window from $E_{c\,min}$ [105]. The light conduction bands at k=0 primarily contribute to N_c under tensile strain. Hence, N_c is smaller under tensile strain. Under small compressive strains, Nc increases because both the heavy and light conduction bands contribute to Nc. But at larger compressive strains, Nc curve shows a dip due to strains beyond the transition from direct to indirect band.

As the conductivity is inversely proportional to the effective masses, the conductivity is proportional to the sum of the inverse of each mass multiplied by the density of carriers in individual band. Accordingly, due to the large change in effective masses/density of states, the change of conductance would be more than three orders of magnitude within the 2% strain [105].

2.2.2.4 Effect of Strain on Mobility. The electron flow exponentially depends on the effective bandgap between the Si conduction band and the Ge valence band. The strained Si and Ge achieve the effective enhancement of carrier mobility which are proved for future CMOS technology [106]. The mobilities of electrons and holes in non-polar semiconductors are determined by the acoustical vibrations of the lattice, impurities scattering and other lattice defects. When the concentration of carriers is small in pure materials, acoustical vibrations of the lattice is the dominating effect. Semiconductor crystals exhibit a strain induced energy shift for the non-degenerate energy levels of the conduction/valence band and strain induced conduction/valence band splitting. Additionally, there can also be a partially or even complete lifting of degeneracy in degenerate bands, caused by the reduction of symmetry. The deformation potential of valence bands is different than that of the conduction bands, due to the degeneracy at the maximum of the valence bands. Carrier mobilities in strained Si, Ge, and $Si_{1-x}Ge_x$ alloys can be able to obtain by the effect of strain on band-structure, effective masses, and with uniaxial deformation potentials. The splitting of the degeneracy of the valence bands increases the hole mobility in Si and Ge. Both 'heavy' hole mass reduction and the band splitting enhance high hole carrier mobilities. At high value strain, the latter suppressing the elastic scattering and even inelastic non-polar optical scattering (dominates in bulk unstrained material) plays the preferential effect. For the investigated case of holes [107-109], the mobility enhancement is independent of strain type, compressive or tensile (Figure 2.13).

On the other side, only a moderate enhancement of the electron mobility in strained Si has been found based on the splitting band theory. $a_{\parallel}/a_0 > 1$ means tensile strain in the

plane of the layer where $a_\parallel$ is denoted as the in-plane lattice constant of the strained lay (Figure 2.13). In Figure 2.13(a) the in-plane electron mobility $\mu_\parallel$ increases sharply. Electrons populate the two lower energy Δ valleys with longitudinal axis along the [001] directions. The lower conductivity mass is the obvious main cause of the increased mobility. Higher values of the electron mobility at tensile strain can be obtained only by invoking intervalley scattering models [110]. Under compressive strain ($a_\parallel/a_0 > 1$), the in-plane mobility first decreases, but soon, the reduction of the transverse mass in these causes a reduction of the scattering rates, due to a lower density-of-states effective mass, and the mobility increases again and remains higher.
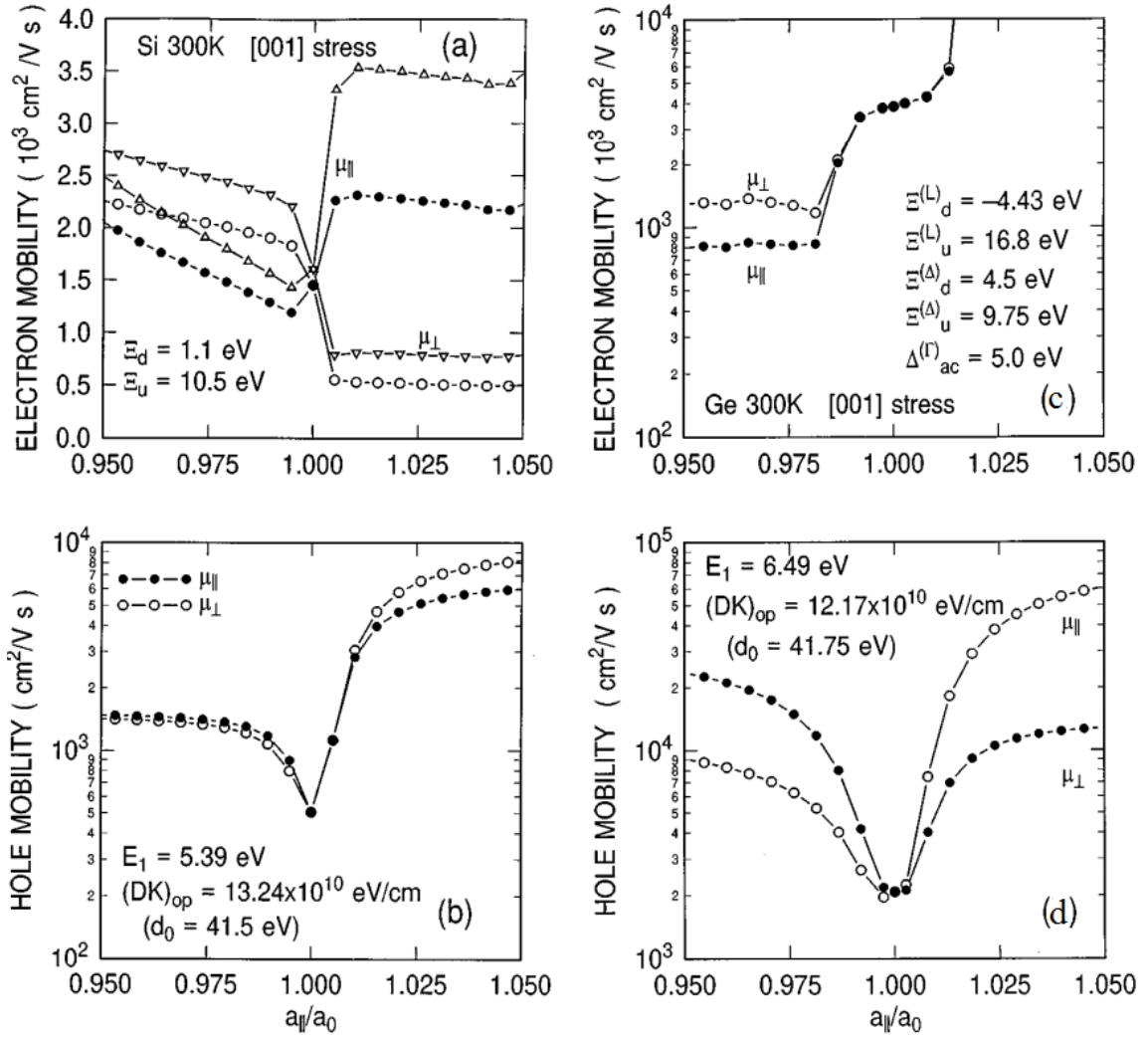
Figure 2.13 300 K (a) electron and (b) hole low-field mobility in Si under strain in the [001] direction. The dots, labeled $\mu_\parallel$, refer to the ''in-plane'' mobility along the [100] and [110] directions, the circles, labeled $\mu_\perp$, refer to the mobility along the [001] direction. The results indicated by open triangles and inverted triangles have been obtained using the intervalley deformation potentials; (c) electron and (d) hole low-field mobility in Ge under strain in the [001] direction.
Source: [110].

In Ge, the situation is qualitatively similar to hole mobility (Figure 2.13(d)). The electron mobility (Figure 2.13(c)), however, strain of opposite sign cause the in-plane and out-of-plane mobilities to exhibit opposite trends. For tensile in plane strain, a dramatic enhancement of the electrons mobility, also due to the decreasing in plane electron

effective mass. The larger intervalley scattering causes, in turn, a lower mobility. For a larger strain, the electrons settle in the $\Delta(100)$ valleys. The mobility now approaches a constant value, approximately equal to the Δ -valleys electron mobility in unstrained Ge [110].

In unstrained $Si_{1-x}Ge_x$ alloy, hole transport has been degraded by the scattering due to the random disorder potential but not affecting electron transport, since the latter occurs in pure Si layers. For electrons, strain breaks the six-fold conduction band degeneracy, splitting into two groups: two lowered valleys that exhibit a longitudinal mass axis normal to the heterointerface, and four raised valleys that have the longitudinal mass axis parallel to the interface [111]. Both effects lead to reduced intervalley scattering [112]. Mobility enhancements saturate for compositions beyond 20% Ge is found by researchers [113, 114] (Figure 2.14). For strained $Si_{1-x}Ge_x$ alloy, alloy scattering mechanisms limits the mobility. The mobility of unstrained $Si_{1-x}Ge_x$ decreases more than that of strained $Si_{1-x}Ge_x$ by alloy scattering since strain reduces intervalley alloy scattering. As a consequence, both mobilities do not show much difference. Carrier mobilities in strained $Si_{1-x}Ge_x$ alloys appear to be completely dominated by alloy scattering. All the advantages expected on the basis of degeneracy lifting are canceled by this strong scattering process.
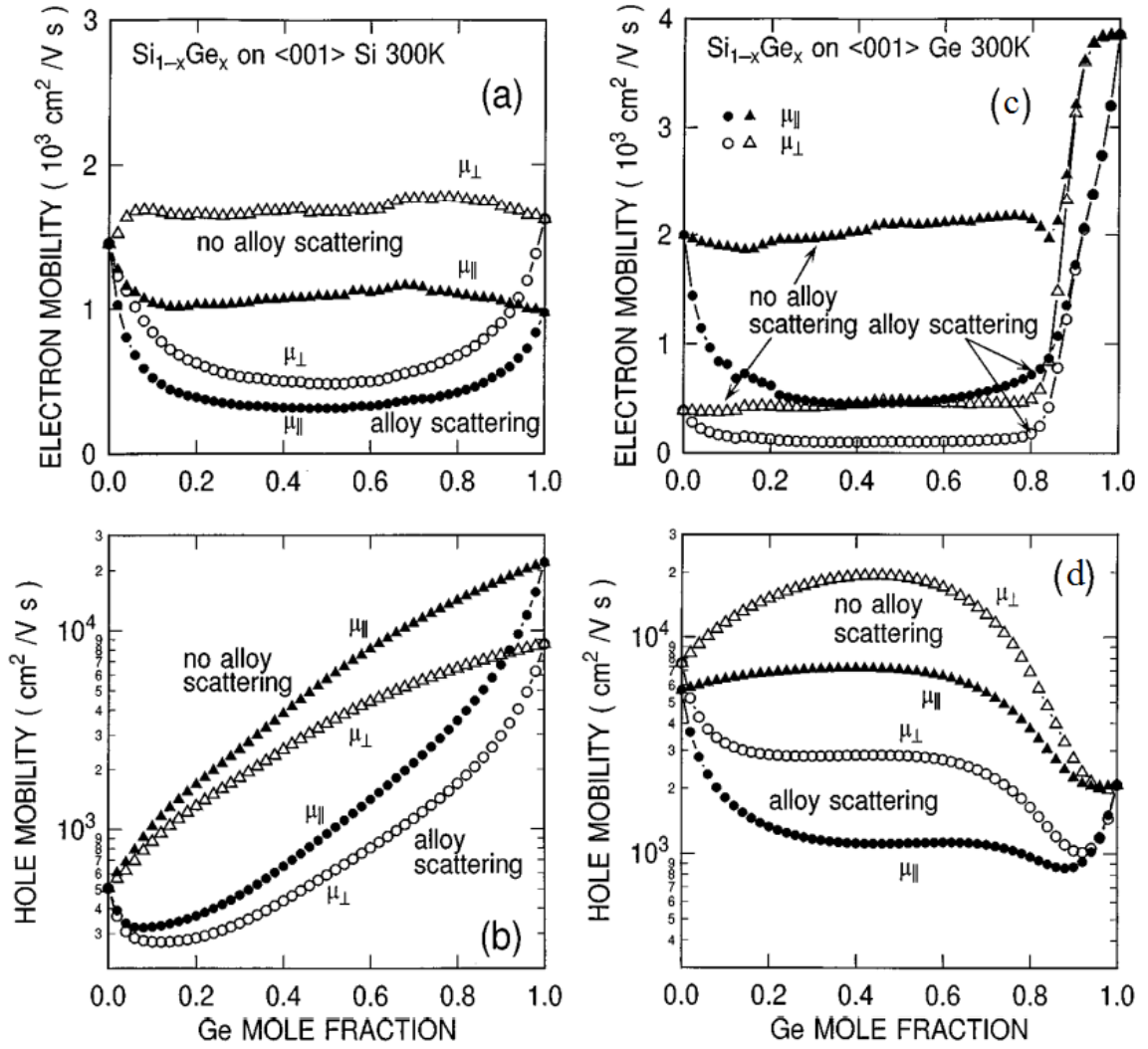
Figure 2.14 300 K (a) electron and (b) hole low-field mobility in $Si_{1-x}Ge_x$ alloys grown on <001> Si substrates; (a) electron and (b) hole low-field mobility in $Si_{1-x}Ge_x$ alloys grown on <001> Ge substrates.
Source: [113, 114].

2.2.2.5 Effect of Strain on Saturation Velocity. Electrons gain energy and their temperature is increased under a strong electric field. The Si electron and hole mobilities are proportional to $T^{-2.4}$ and $T^{-2.2}$, while the Ge electron and hole mobilities are proportional to $T^{-1.7}$ and $T^{-2.3}$ respectively[115]. Si and Ge, as non-polar semiconductors, their mobilitites are dominated by acoustic phonon interaction. When the carrier energy is beyond the optical phonon energy, the probability of emitting an optical

phonon increases shortly. This mechanism results in the carrier velocity to saturate with increasing electric field (Figure 2.15). Miyata et al. found the mobility for strained Si is almost three times larger in low field, 4000 cm^2/V s than that of unstrained Si, 1500 cm^2/Vs. This attributes to the smaller transverse-mass transport. At 300 K (Figure 2.15(a)), While in fields larger than 20 kV/cm, the drift velocity strained Si tends to show a larger value. However, all curves slow down and reach a similar saturation velocity ~ 1.0×10^7 cm/s. In low temperature at 77 K (Figure 2.15(b)), unstrained Si (17 000 cm^2/V s) has higher mobility than strained Si (23 000 cm^2/V s), and the saturation velocity is reached with fields > 5 keV/cm. There is no big difference between strained Si and unstrained Si. The Si saturation velocity is estimated to be ~ 1.3×10^7 cm/s at 77 K.
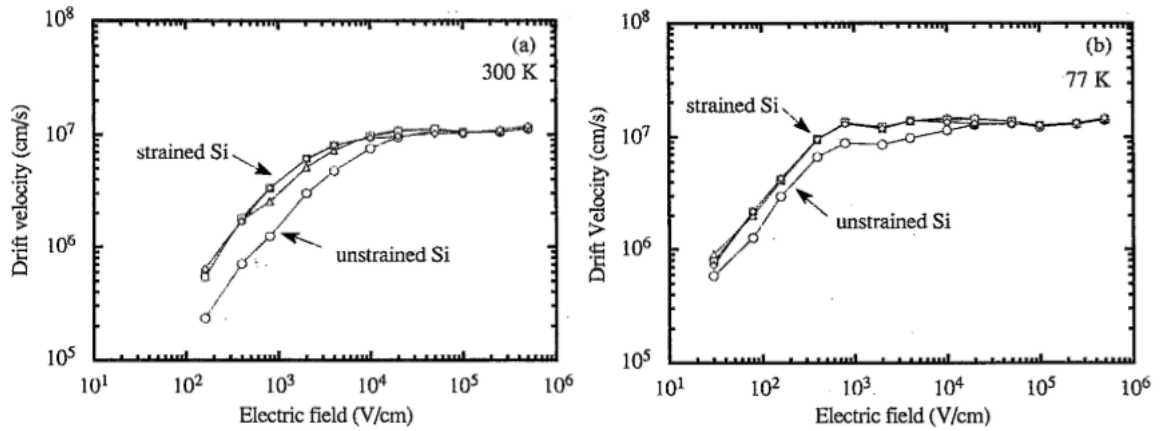
Figure 2.15 (a) Velocity-field characteristics of an electron in a strained Si layer for various valley splitting values ΔE, where unstrained Si corresponds to ΔE=0; (a) 300K and (b) 77K. o for ΔE =0, Δ for ΔE =0.1 eV, ⊡ for ΔE =0.2 eV, and ◇ for ΔE =0.4 eV.
Source: [116].

The low-field mobility in Si$_{1-x}$Ge$_x$ is influenced both by the strain and the alloy scattering. The mobility enhancement or degradation effect, depends on not only the carrier type, i.e., electrons or holes but also the transport direction--parallel or perpendicular to the

growth direction of the strained $Si_{1-x}Ge_x$ layer. In axial Si/Ge HJs the electron transport occurs parallel to the growth direction of the strained $Si_{1-x}Ge_x$ layer. This leads to reduced electron low-field mobility, compared to Si part. Furthermore the electron saturation velocity decreases with increasing Ge concentration x (Figure 2.16(a)). The smaller intervalley phonon energies of Ge phonons as well as the strong alloy scattering contribute to this large reduction effect because as a general rule, the saturation velocity decreases with decreasing phonon energy.

The effect associated with the mobility or drift velocity decrease with an increase in the electric field/voltage lower the current, the Gunn Effect is expected in Si/Ge NW HJs. The Gunn effect has been verified that the transition of electrons from the two-fold valley to the four-fold valley can occur in $Si_{1-x}Ge_x$ layer. After an electric field in the material reaches a threshold level, devices produce negative resistance. With lattice temperature, carrier temperature, doping values and mole fraction, an analytical high-field mobility model is proved [117, 118]. The negative differential slope of electron velocity versus electric field is predicted in Fig 2.16(b). More about Gunn Effect will be discussed in Section 2.2.3.a.

(a)   (b)
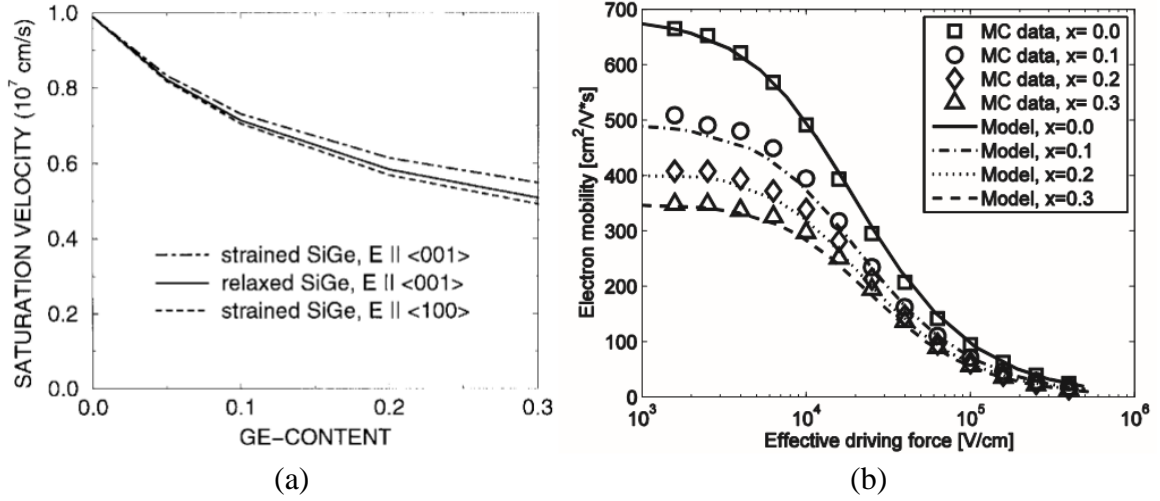
Figure 2.16 (a) Theoretical results for saturation velocity in Si and Si$_{1-x}$Ge$_x$ at 300 K as a function of Ge content x. (b) Electron mobility in Si$_{1-x}$Ge$_x$ as a function of effective driving force for several germanium mole fraction.
Source: [117, 118].

2.2.3   Electrical Properties

The combining Si and Ge provide a strategy to manipulate energy bandgap and electronic structure for the specific needs. Meanwhile, strained Si and Ge are also attractive materials for the promising electronic and optoelectronic devices (discussed in Section 2.2.2). The created a pseudomorphic junction results in band discontinuities and creates energy barriers between Si and Ge at the heterointerface. The HJ's complexity related to the difference in bandgaps of the Si/Ge and to the consequent charge transfer and dipole induced [38, 119] and hence is thriving area for researching (like bulk HJs) [120-123].

Type-II band-offset character with holes and electrons in different momentum is demonstrated that the valence band maximum and the conduction band minimum of the HJ are located on each side. The value of the offset in consequence controls the very nature of the heterostructure. Van de Walle and Martin reported the valence band maximum is on the Ge part, while the conduction band minimum is on the Si part [122, 123]. This type-II offset formed by the smaller bandgap of Ge compared to that of Si (indirect bandgap Si

37

~1.14 and Ge ~0.67 eV, respectively) results a reduction of the bandgap of the pure HJ. This reduction helps to improve the specific function of bandgap engineering (such as increasing the devices inherent switching speeds due to the higher Ge mobility). Indeed, its magnitude can be strongly modified by strain, geometry of the heterointerface and composition of the Ge content. However, the physics nature revealing these phenomena at nanoscale Si/Ge strongly changes compare to bulk Si and Ge. When Si and Ge form an abrupt interface, their bands line-up in order to compensate their bandgap differences. The transition ability of electrons and holes is determined by valence and conduction band offsets. Based on ab initio methods, Van de Walle and Martin estimated $\Delta E_v = 0.58$ eV and $\Delta E_c = 0.28$ eV in the unstrained HJ, in consistent with experiment data. They also suggested the evaluation of the offset could not be correct without including the strain [122, 123]. Thus Si/Ge NWs provide a platform in combining the fabrication, size parameter and heterostructuring (or alloying) for performing further research to develop desired properties.

The exciton energy of Si is smaller than that of Ge [124], hence not only strain have an influence on the band offset, but also the scaling dimensional parameter of NWs would shift the maximum and minimum of the energy band and the band alignment. Moreover, NWs compared to large size wire have an advantage to tolerate a relatively higher degree of lattice mismatch and resulting strain by expanding or bending without introducing significant defects. Analyzing all these conditions at once is too complicated to determinate the band offset in Si/Ge NWs.

A type-II band offset is confirmed as well as the reduction of the bandgap compared to the pure Si and pure Ge NWs by the analysis of wave function localization [125]. Amato

et al. revealed that in abrupt NWs (where Ge content is x_{Ge}) the E_g (x) could be expressed as the following:

$$E_g = 0.98292 - 1.3508x_{Ge} + 1.3478x_{Ge}^2 \qquad (2.4)$$

Besides, at Si/Ge HJs with relatively modest Ge concentrations, interface scattering is the dominant mechanism. Consequently, the optimized Ge content could be selected to minimize the heat conductivity for thermoelectrics applications.

Dyakonov and Shur have discovered that flow of the electron in two-dimensional HJs should be unstable. We predict current instability of our sample with a DC due to the 2D HJs. Another main task of this study is to investigate a possibility of the Gunn generation in 2D Si/Ge HJ structure, as well as the high possibility whether the consequences of the negative differential in the two-dimensional exist. This case may differ substantially from the conventional 3D Gunn Effect since non-exponential diffusion law governs the charge relaxation in 2D HJs.

2.2.3.1 Analogy of Gunn Effect in Si/Ge HJs. As we mentioned above, shown in Figure 2.17, the energy-momentum relationship between Si and Ge contains various energy valleys with the following properties:

a) In the lower valley, electron has a small effective mass but high mobility,

b) In the satellite high valley, electron has a large effective mass but low mobility,

c) The two valleys are separated by a small energy dispersion.

Both in Si and Ge, at the 300K equilibrium, they have high mobility (~ 8000 cm^{2}V^{-1}s^{-1}) in bottom low valley [126]. If a strong electric field is applied, those electrons are scattered

and accelerated (from Si to Ge or from Ge to Si, indicated as blue arrow in Figure 2.17) into the satellite valley separating by the energy dispersion of the intervalleys. This effect leads to a decrease in the average electron mobility. In Gunn Effect [127], if an electric field is raised to a threshold value, the mobility of electrons start to reduce with the increase of electric field.
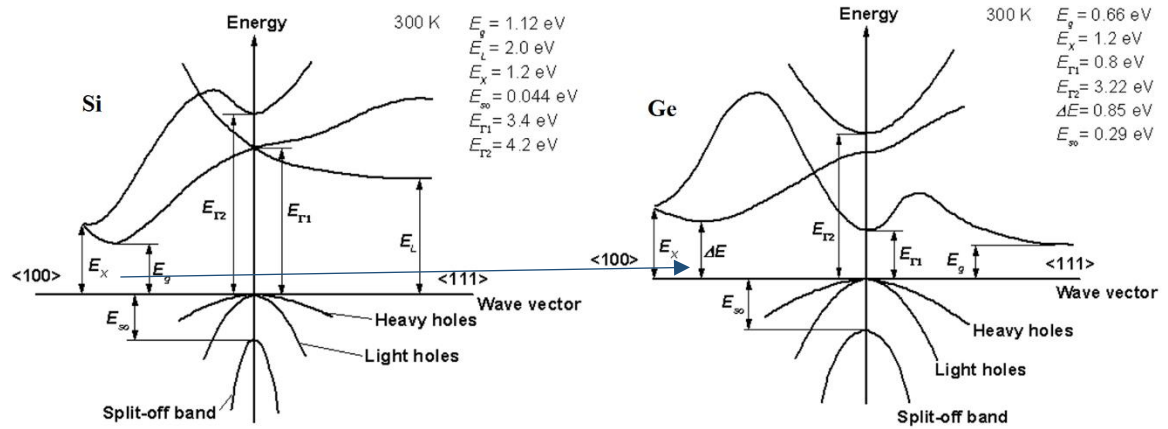
Figure 2.17 The energy momentum transition of band structure from Si to Ge.
Source: [128, 129].

Thus, this Gunn like effect expected in Si/Ge NW HJs would create a negative incremental resistance region in V-I relationship with its frequency primarily determined by the characteristics of HJs internally not by any external circuit. In this negative resistance region, Si/Ge NW HJs is enabled to act as both oscillator and amplifier with adding external component. This property of the Gunn like effect along with its timing properties cause it to behave as an oscillator through adding RCL filters to provide an optimum value of current flows through it. It oscillates as the voltage increases, then the resistance will increase. This is because, the negative resistance property of the Si/Ge NW HJs balances out the effect of any real resistance existing in the circuit. This results in the generation of sustained oscillations under DC bias or damping (resistance in electronic

circuits preventing the growth of oscillations). Further, the amplitude of the resultant oscillations will be limited in the range of the negative resistance region. Till now, although some Gunn effects are reported in III-IV compound HJ, barely none in Si/Ge NW HJs is found. Our results will be present in Chapter 4.

2.2.3.2 Double Injection Space-Charge Limited Current. Under an applied voltage, the flowing current is determined by three processes: charge injection, charge transport and recombination. At low electric field, electrical contacts to semiconductors are commonly non-Ohmic but act as a nearly ohmic contact in most cases. And Ohmic contact will change to non-Ohmic or even a nearly blocking contact with the carrier supply limited by Schottky-type thermionic emission under certain bias conditions [double]. By applying increasing field, they may change again to a nearly ohmic contact. This effect facilitates the reduction of the width of the potential barrier to inject carrier by Nordheim-Fowler type tunneling [130].

The electrical contacts in semiconductors affect the carrier transport (the I-V curve of HJs) for two-carrier current injection. The dominant effect in holes and electron currents are Space-Charge Limited Currents (SCLC). At any voltage, there will be some excess charges injected into the semiconductor. When the concentration of injected excess electron becomes comparable to that of thermally generated free electrons, the SCLC becomes noticeable, and the current-voltage characteristics change. A space charge develops a potential that impedes the carriers. As a consequence, the slowed carriers increase the resulting space charge density and potential. The high density of these charged carriers creates a field gradient, which suppresses the current density. When the space

41

charge suppresses the current, the resulting potential developed by the space charge reduces the number of carrier emitted [144].

One carrier SCLC theory can be simplified, based on the following two assumptions that:

  I.   Only drift currents are considered, neglecting diffusion currents.

 II.   An infinite amount of electrons are available for injection at the cathode.

In low electric field, the velocity of the carriers is proportional to the mobility. Known as the trap free square law, the Mott-Gurney square law, and Child's law for solids. The current density is proportional to V^2, V is the applied voltage. In high electric field, the velocity of the carriers become saturated. The current density is proportional to V [131] [132].

Double carrier injection in solid between dissimilar contacts are concluded in the following five regions [133] (depicted in Figure 2.18):

(a)   **(b)**
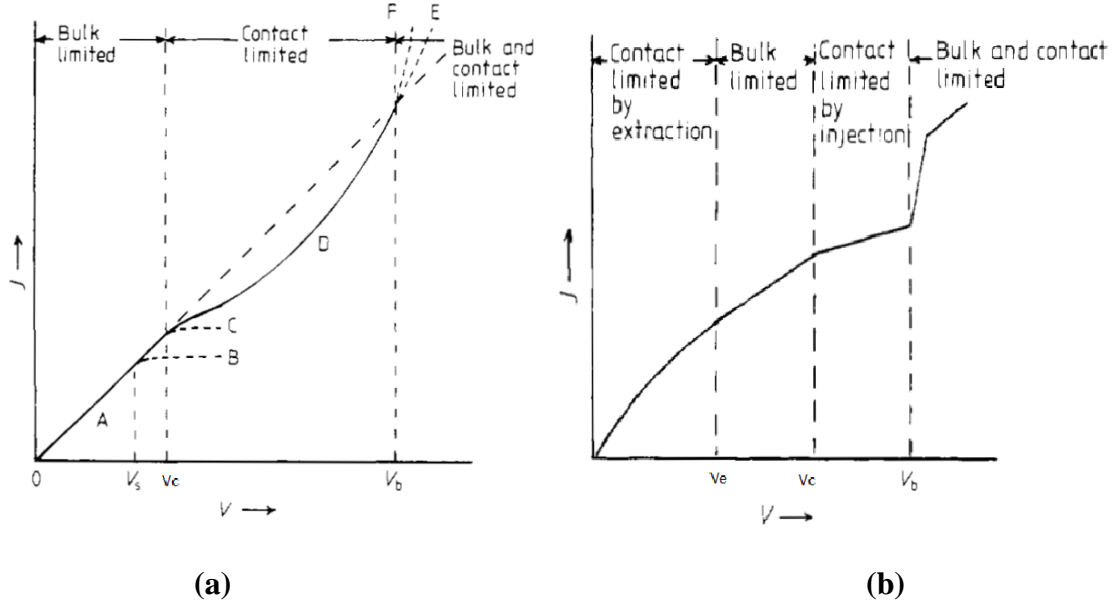
Figure 2.18 (a) The three conduction regimes: the low-field bulk-limited, the medium-field contact-limited, and the high-field bulk and contact limited, in J-I characteristics for a perfect intrinsic solid with neutral contacts: (A) ohmic region, (B) current saturation in the absence of thermionic emission, (C) current saturation due to the limit of thermionic emission without the consideration of the image force lowering of the potential barriers, (D) field enhanced (Schottky type) thermionic emission current, (E) injected carrier densities, (F) the set-in of the tunneling field emission mechanism. (b) The energy band diagrams and the J-V characteristics for dissimilar contacts for both the electron and the hole injection (the metal for the cathode dissimilar to the metal for the anode)-double injection for both the electron and the hole extraction.
Source: [133].

V < Ve Contact Limited At low fields, electron extracting contact is blocked. The electron density n is higher than the hole density p. And the electron injection efficiency at one contact is also higher than the hole injection efficiency at the other contact. As a result, the current is contact limited because of carrier extraction.

V < Vs Bulk limited For a non-ohmic contact, the height and the width of the potential barrier near the contact determine the supply of charge carriers. Thermally generated electrons and holes are balanced out by contact extraction, then the current will saturate at a value Vs. In physical concept, the neutrality of carriers leads to the linear J-V relation.

By expressing J $\propto V^m$, at very low fields, both electron and hole are contributing to the current with m > 2. For large applied voltages, the single injection Mott-Gurney equation becomes dominant with m = 2. In other word, at high fields, the current may become SCLC mainly due to single electron injection from the cathode.

Vs < V < Vc With thermionic emission, the contacts continue to supply carriers to the semiconductor before reaching the maximum rate of their supply.

Vc < Vs One thing to note here is that if the threshold voltage for the onset of the field emission at the cathode is lower than the threshold voltage Vc, for the onset of the current saturation at the anode, no contact-limited regime will be observed.

Vc < V <Vb Contact limited At V > Vc, the field-assisted thermionic emission current is rising slowly with m < 1 for J $\propto V^m$ as shown in Figure 2.18. In this regime, carrier concentration is lower than intrinsic carrier concentration.

Vb < V Bulk and Contact limited At ever higher V, high-field mechanisms including field-enhanced thermionic emission, field emission and thermionic field emission could further affect carrier injection processes [134]. Both the potential barrier height and the width are much reduced by the high field. The concentrations of n and p injected are now larger than intrinsic concentration n_i. When the applied voltage reaches the threshold voltage Vb, two-carrier transport instead of present one-carrier transport will dominate. The important effect here to note is at voltages first reaching Vb, current jumps due to previous low homo-space charges near the contacts (Figure 2.18(b)).

Impedance spectroscopy is used in our experimental measurements to DC and AC currents in one-carrier or two-carrier SCLC, and get the carrier and field distributions inside the HJs.

2.2.3.3 Electrical Noise. For a physical quantity, noise and fluctuation, in general, is inevitable as a basic element. In the electrical application of nanowires, noise should be treat as an important parameter. Every current or voltage within a given electrical circuit can be viewed as consisting of a deterministic signal and of noise. Electrical noise is a random process, and as such cannot be described in a deterministic sense.

The equilibrium Nyquist noise (the white thermal noise) of a NW of resistance R at an absolute temperature T can be estimated $\approx 4k_BTR$, where k_B is the Boltzmann constant. Its power spectral density is nearly constant everywhere of the frequency spectrum. The Nyquist noise occurs in any conductive semiconductor and is caused by the random motion of the current carriers.

However, in the current of a NW a significant contribution to the electrical noise is suggested to arise from the conductance noise [135]. This noise has a spectral power inversely proportional to the frequency of the signal $\sim 1/f^\alpha$, where f is the frequency of the noise signal, α is the Hooge parameter and is known as '1/f noise'. In Hooge's model, the flicker noise is attributed to carrier density or mobility fluctuation mechanisms. A. Bid et al. call this model the intrinsic resistance fluctuation model [135], which is given by the following phenomenological equation due to Hooge [136]:

$$S_I = I \times \frac{e\alpha\mu V}{fL^2} \qquad (2.5)$$

where α is the dimensionless Hooge constant, μ the mobility and L the NW length.

There is a direct link between 1/f noise and defects. Annealing helps to diminish Hooge parameter. The oldest model of 1/f noise is McWhorther's model of electron

random trapping and detrapping in surface states [137]. Modern analyses of the noise of complicated devices often reach to the conclusion that the surface generates only a fraction of the flicker noise, whereas the greater part is bulk noise, the mobility fluctuation type. Thus whether it is a result of the modulation in the number of carriers, or in the mobility of the carriers in a given material are associated with Flicker noise from the surface or bulk of the semiconductor device. A wide range of mechanisms including thermal modulation effects, diffusivity fluctuations, trapping mechanisms with distributed time constants, and variations in surface recombination velocity [138] attribute to Flicker noise. Decades ago, an experiment about 1/f noise decreased by one or two orders of magnitude with time was reported after applying mechanical stress [139, 140]. This suggests a link between 1/f noise and strain. In many devices, flicker noise is attributed to a combination of all these mechanisms.

Since no single theory explains the cause of flicker noise in every device, estimating the actual value of the 1/ f noise should include many different sources [141, 142]. In the issue, estimating the noise component must depend on experimental measurement.

Kinetic noise is associated with temporal fluctuations in the velocity of carriers accruing from scattering [143]. In experimental figures, kinetic noise introduces a peak in the noise power spectrum.

The last one, shot noise ~ 2qI, where I is the average current created by the electron stream, q is the electron charge, results from the time-dependent variation of the electrical current due to the quantization of charge. The random arrivals of discrete charge and the statistical variation in the arrivals results shot noise. Shot noise is independent of frequency at low and intermediate frequencies, frequency-dependent at higher frequencies. In

absolute zero temperature, shot noise is the only electrical noise. Terman pointed out shot noise is reduced by space charge [144]. As we discussed in Section 2.2.3.b, space charge surpresses the carriers by developing a potential and those slowed carriers increases the resulting space charge density and potential. In addition, Terman suggested the potential developed by the space charge could further eliminate the number of carriers emitted. In conclusion, when the space charge surpresses the current, the various arrivals of the carriers are reduced; the depressed variation results in less shot noise.

2.2.4   Thermal Properties

Since electrons have much shorter mean free paths than phonons, the structure of NWs affects heavily more on the thermal conductivity than the electrical conductivity [145]. Building with different interfaces or compositions structures, the thermal properties of Si/Ge NWs is enhanced. Thermal conductivity in pure Si NWs was demonstrated 100-fold smaller than bulk Si while charge transport remains unaltered [146, 147]. This effect is mainly caused reduction of thermal conduction due to the strong phonon boundary scattering in NWs. Moreover, high crystallinity arrangements of atoms of two different materials were demonstrated resulting in higher thermal conductivities than the two constituent materials [148]. Although the dimension of our NWs is well beyond the mean free path of phonons (Figure 2.19) and confinement effects limit region, we still expected that the Si/Ge interface offers the possibility of engineering heat conduction and phonon scattering. Because the difference in the mass between Si and Ge influencing the phonon dispersion.

Si and Ge contribute unequally to the overall thermal conductivity because of the large difference in Si and Ge masses. Hu and Poulikakos [149] has reported the more the

device is heterostructured, the more the thermal conductivity is reduced. They suggested the phonon velocity is significantly reduced in Si/Ge NWs with respect to pure NWs[149] due to heat conduction suppressed by the phonon interface and boundary scattering.

The $Si_{1-x}Ge_x$ alloy layers of Si/Ge NW HJs has low thermal conductivity due to generally alloying and surface boundaries. Phonon boundary scattering mainly associated long-wavelength phonons is frequency independent and, alloy scattering mainly associated short-wavelength phonons is frequency dependent.

Accounting to Fourier's law, the standard macroscopic approach to estimate heat flux density is expressed in the following formula [150]:

$$J = -k\nabla T \tag{2.6}$$

the quantity κ is the lattice thermal conductivity of the semiconductor.

In addition to the critical role of Si and Ge alloy, the thermal conductivity of $Si_{1-x}Ge_x$ alloy NWs vary with Ge concentration was observed[151]. Thermal conductivity reduction in Si/Ge NWs is mainly due to the alloy scattering mechanism in $Si_{1-x}Ge_x$ regions, while the boundary scattering effects contribute to further decrease κ.

Then Yin et al. [152] reported the thermal conductivity of $Si_{1-x}Ge_x$ alloy region of Si/Ge NW has a small dependence from the NW length as well as Si:Ge ratios. In addition to boundary and alloy scattering, Martinez et al. suggesting the carrier-phonon scattering mechanism is also found in doped Si/Ge NWs [153].
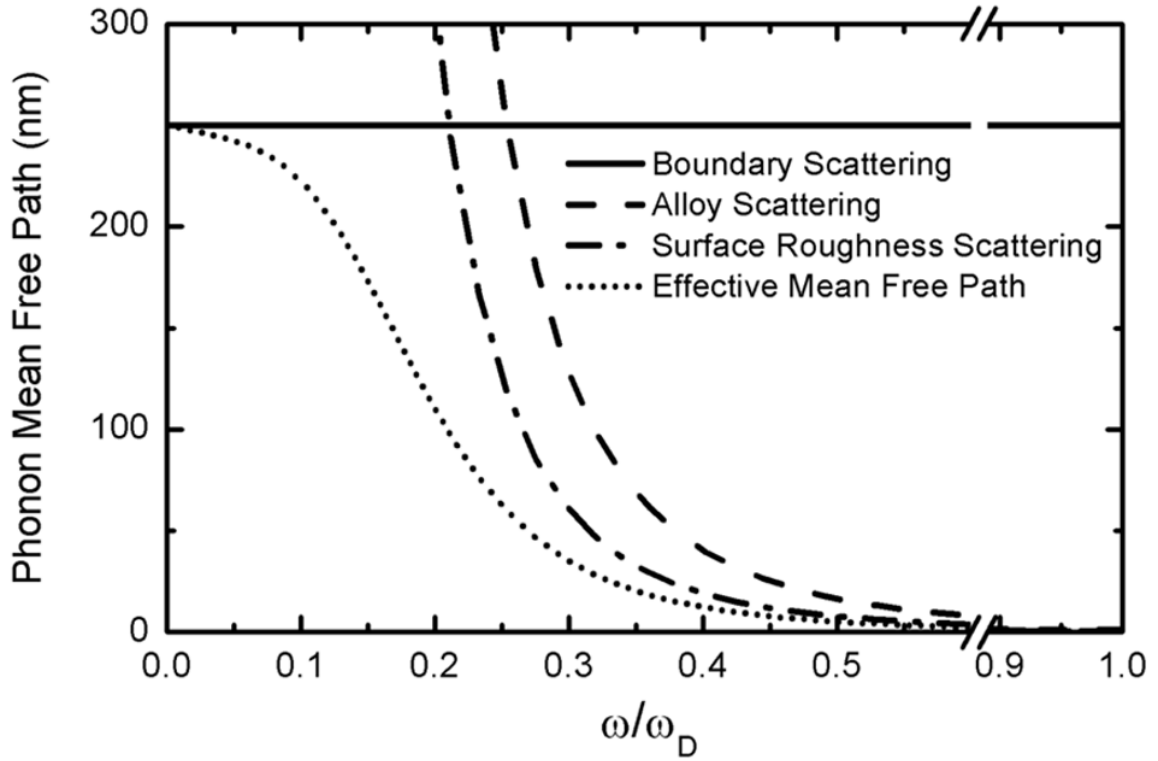
Figure 2.19 Phonon mean free path of various scattering mechanisms versus normalized phonon frequency. ω_D is the Debye frequency.
Source: [38, 154].

At the Si/Ge interface layer, the wavelengths of the particles reduced and compressed, which hinders the heat transport largely. The low energy modes at the disordered surface or the Si/Ge interface may lower the value of κ with increasing temperature. In order to improve the thermoelectric efficiency, Si/Ge HJ structure contributes the enhanced phonon scattering to compress the lattice component of the thermal conductivity. Figure 2.20 illustrates the thermal conductivity for several NWs [156]. It proved that thermal conductivity is reduced due to surface-boundary scattering for NWs with diameter over $\simeq$100 nm. For smaller diameters NWs, the alloying scattering play a main role in suppressing phonon transport.

Shelley and Mostofi confirmed the significant reduction of thermal conductivity induced by the axial Si/Ge HJ [155]. They also evaluated by adding a single layer of Ge

into a pure Si NWs could decrease the thermal conductivity by five orders of magnitude

for the ⟨111⟩ direction, four orders for ⟨110⟩ and ⟨112⟩ directions.
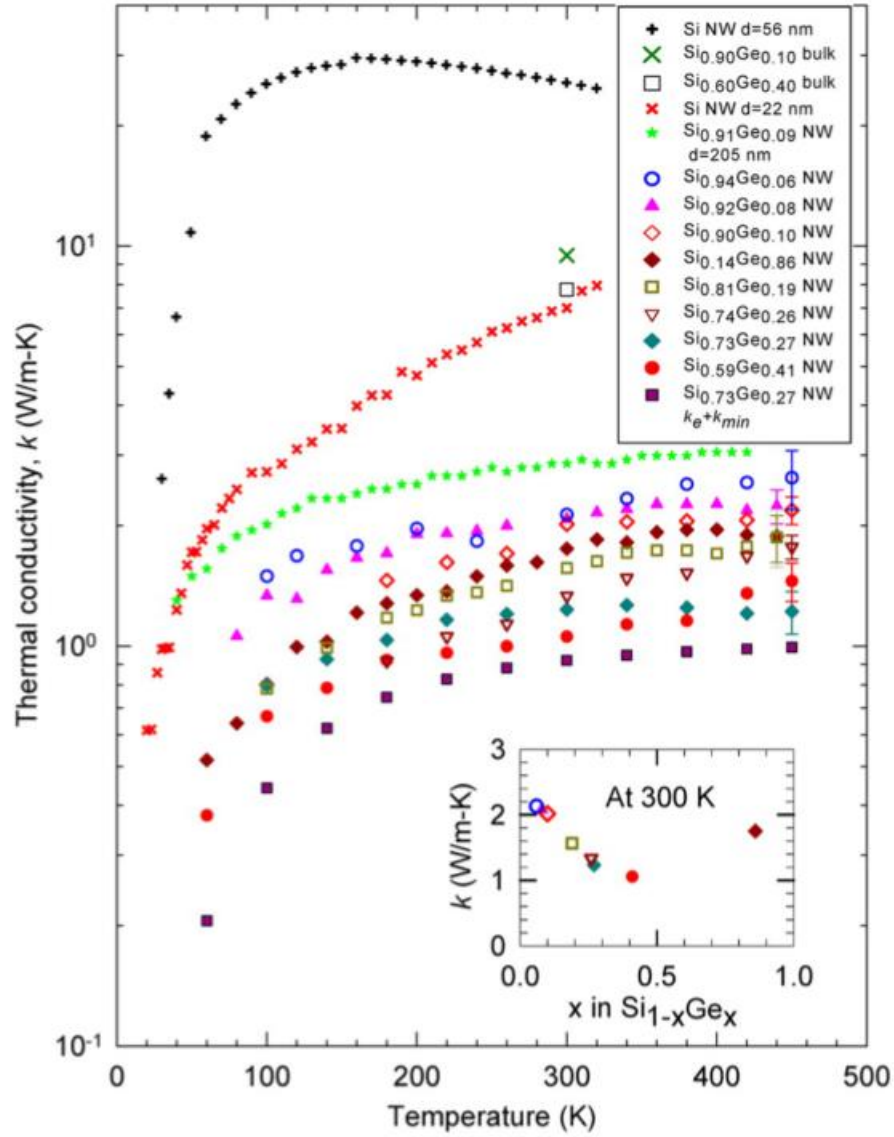
Figure 2.20 Thermal conductivities of several $Si_{1-x}Ge_x$ NWs. The inset shows the thermal conductivities as function of Ge concentration at 300 K.
Source: [38, 156].

2.2.5 Optical Properties

The optical response of Si/Ge NWs depends on intrinsic and extrinsic parameters. Since direct bandgaps can be obtained with strong oscillator strengths, Si/Ge NWs have potential application in the new generation light emission devices. The visible light absorption and the strong charge separation will promote an important position for Si/Ge NWs in the future photovoltaics. All effects, such as size, geometry, alloying and strain associated with carrier interactions, electron addition, carrier lifetime, or removal energies, even correct spectroscopic experimental data analysis, strongly influence the studies of optical absorption and emission properties.

The dependence of Si and Ge refractive index n and extinction coefficient k on the photon energy are depicted in Figure 2.21(a). Si exhibits very typical indirect bandgap absorption behavior. The optical absorption coefficients α of Si (Figure 2.21(b)) depends linear on the square root of the energy. For Si, the optical processes for absorption and emission are very inefficient. While Ge both has the absorption curve part similar to Si and other part similar to the direct bandgap III-V compounds. The optical absorption coefficients α increases fast according to the fundamental absorption associated with the band transition. The rise is large for direct band transitions ($E_g^{dir} = 0.81\ eV$ at 300K). For indirect band transitions, the rise is smaller (Si: $E_g^{dir} = 1.12\ eV$ at 300K; Ge: $E_g^{dir} = 3.03\ eV$ at 300K) [72].

Amato et al. [128] have generated a strong electron−hole separation in Si/Ge NWs with the inclusion of many body effects. This Si/Ge NWs have an abrupt heterointerface and the type II band offset. Studies [157, 158] have pointed out that adding Ge atoms to Si NWs for different types of geometries and different crystallographic directions would red-

shift the first absorption peak remnant of the direct absorption peak of the bulk Ge. Si/Ge

NWs is further confirmed their application in high efficiency photovoltaic devices. The

structure change from pure NWs to Si/Ge HJs NWs is high enough to extend the energy

edge for covering strong absorption wavelength band. As a result, the small effective mass

in the new energy level further decreases the threshold for optical transparency and lasing.
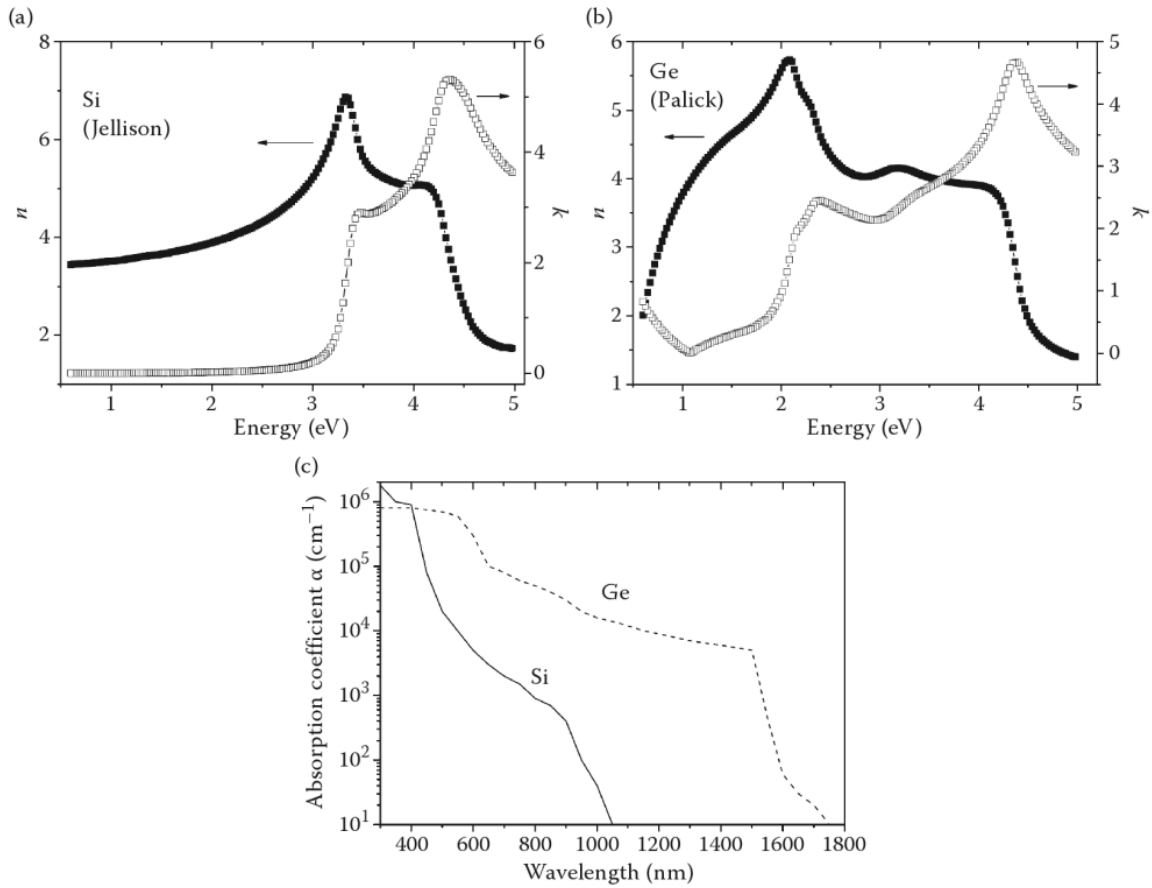
Figure 2.21 Silicon and germanium (a) refractive index n, (b) extinction coefficient k, (c) absorption coefficient vs. wavelength.
Source: [159, 161].

CHAPTER 3

EXPERIMENTAL METHODS

3.1 Characterization Techniques

The NWs' morphology and dimensions are characterized by SEM. The NWs' crystalline quality and orientation are determined by TEM. The composition x of the $Si_{1-x}Ge_x$ intermixing layer of NW is mostly identified using EDX by the Vegard's law and Raman scattering spectroscopy by the shift of the Si-Si Si-Ge Ge-Ge peaks. In order to quantitatively understanding the type-II staggered band alignment of tensile strained-Si on compressively strained-Ge, the local strain structure is estimated by TEM and Raman spectroscopy for relatively high strain and high spatial resolution. The composition dependence of the fundamental absorption edge in $Si_{1-x}Ge_x$ is determined by PL. At the same time, PL spectra are also used to determine the surface, interface, and crystal defects, such as atomic vacancies and substitutions as well as internal strain. The optical constants of interband transitions in the IR-UV region are most sensitive to strain and composition. The absorption coefficient of strained $Si_{1-x}Ge_x$ layers was also dependent on different Ge concentrations.

3.1.1 TEM, SEM, and EDX

Electron microscopes using electron beams have much higher resolution compared to that in optical microscopes. TEM is the most efficient and versatile microscopy technique for structural, compositional, and chemical characterization of materials. As the name transmission electron microscope (TEM) implies, an electron beam of uniform current density is transmitted through a thin specimen. Schottky, thermionic, or field emitted the

electron beam from a small area tip called the electron gun. Before transfer this electron beam to the sample, the illumination system, which consists the condenser lenses of different apertures manipulates an electron beam with desired diameter. The typical range of acceleration voltage is 100 – 200 kV. After the beam interacts with the sample, a diffraction pattern is formed by the objective lens in the imaging system of TEM. Two imaging modes (bright field and dark field) are achieved by changing the aperture position of the objective lens. Bright field means all area with no sample reached the beam will appear bright. This is the most common mode of TEM operation formed by occlusion and absorption of electrons in the sample. In contrast, no sample-beam interaction area appears dark in the dark field image. Because no sample scattering is included in the reflections, the setup of SEM, like that of TEM, consists of an electron optical column, a vacuum system, electronics, and software. The difference between them is in SEM the electrons is focused into a fine spot on the sample surface with shorter column comparing to a transmission into the sample in TEM. SEM is based on scattered electrons, while TEM is based on transmitted electrons. SEM has much lower resolution (tens of nm) than TEM, which has spatial resolution (1nm or less). However, the specimen chamber is larger in SEM than in TEM because there is no restriction on sample size. SEM produces accurate 3D images of the sample surface in the dispersion on the control monitor, while TEM generates 2D images interpreting internal composition details, such as crystallinity and lattice structure.

EDX identifies the elemental composition of samples by X-Ray. EDX performs qualitative, semi- quantitative and quantitative elemental analysis and spatial distribution of elemental maps inside electron microscope with detection limit ~0.1%. The setup of

EDX includes the X-Ray beam excitation source, the X-Ray detector, the pulse processor and the analyzer. The X-Ray associated with the elemental composition emitted from sample after exciting by electrons beam, the similar beam used in SEM or TEM.

3.1.2 Raman Scattering

Although Raman and PL data can be obtained with the same optical arrangement, the Raman signal is much weaker in comparison with the PL signal. Moreover, this weak signal can be routinely measured by providing orders-of-magnitude larger laser signal. The typical Raman shift $\omega_{phonon}/\omega_{laser}$ is very weak only about 10^{-6}. The photon frequency shifts during the scattering process because of energy changed by interacting with molecular vibrations. This is called Raman scattering process. They gain energy by absorbing a phonon (anti-Stokes shifted), or lose energy by emitting one (Stokes shifted), according to the energy and momentum conservation rules:

$$\omega s = \omega i \pm \Omega, \tag{3.1}$$

$$qs = qi \pm K, \tag{3.2}$$

where ωi and ωs are the incoming and scattered photon frequencies, respectively; qs and qi are the incoming and scattered photon wavevectors, respectively; and Ω and K are the phonon frequency and wavevector, respectively. Raman measurements record the Raman shift peaks by filtering out the undesired Rayleigh peak. Since the Raman signal is weak compared to the excitation, the use of a double monochromator or even triple monochromators is necessary to separate the Raman signal from the strong Rayleigh light that accompanies it. A resolution $\Delta f = 0.1$ cm^{-1} is typical for a good double monochromator.

The orientation of a crystalline sample is characterized in the polarized Raman spectra. The polarized Raman system using the exciting polarized light analyze the polarization of the scattered light. The angle between the incident light and the sample surface must be carefully arranged. The scattered light remaining in the visible region is detected by light photomultiplier tubes (PMT). For a low dark count, PMT is cooled to further reduce dark count and a cooler is used.

Fluorescence overwhelming the Raman signal could be suppressed by operating in the infrared region than in the ultraviolet-visible region[162].
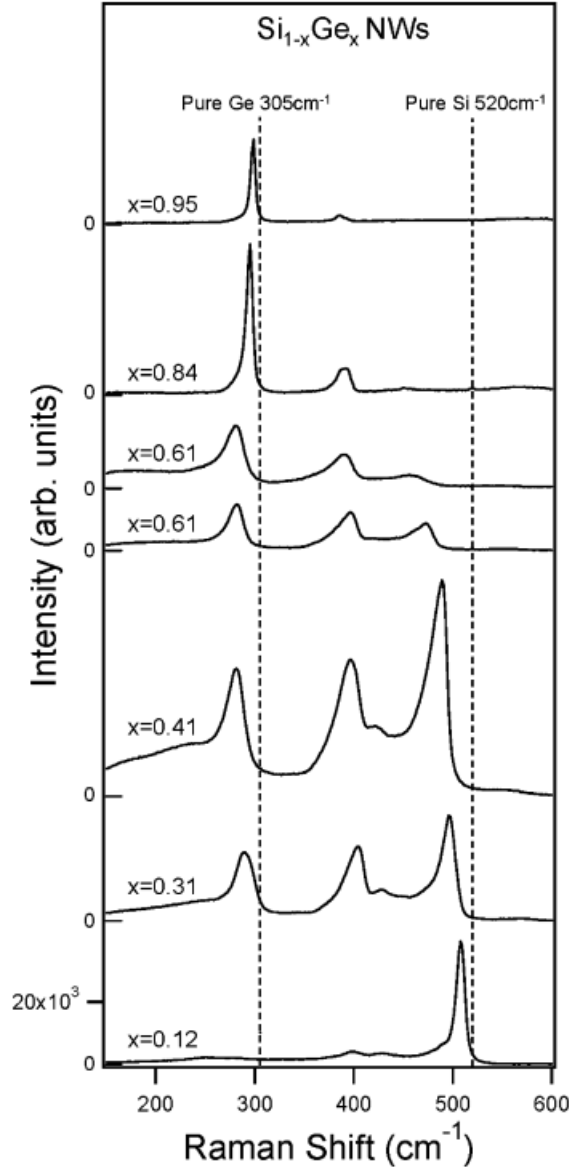
Figure 3.1 Micro-Raman spectra from seven batches of crystalline $Si_{1-x}Ge_x$ alloy nanowires collected at room temperature with 514.5 nm excitation. The spectra were collected from wires remaining on the growth substrate and contain contributions from ~100 nanowires with random orientation relative to the incident polarization. Three prominent bands are observed as the Ge-Ge band (~300 cm-1), the Si-Ge band (~400 cm-1), and the Si-Si band (~500 cm-1). The dashed vertical lines refer to the position of the k = 0 LO-TO Raman band in pure crystalline Ge and Si.
Source: [163].

Raman spectra measured by Lu et al. [163] in crystalline $Si_{1-x}Ge_x$ nanowires

(80−100 nm) grown along the ⟨111⟩ direction are shown in Figure 3.1. In Raman spectra,

the intensity and the position of the Raman peaks strongly depend on the composition are shown. Raman spectrum of Si/Ge NWs displays three prominent peaks corresponding to the Ge-Ge, Ge-Si, or Si-Si bonds are observed as the Ge-Ge peak ($\sim$300 cm^{-1}), the Si-Ge peak ($\sim$400 cm^{-1}), and the Si-Si peak ($\sim$500 cm^{-1}). In this case, the Si$-$Si band position which is the most sensitive to the Ge concentration from the Si$_{1-x}$Ge$_x$ NW is shifted to the left of the Si-Si peak from the substrate. Due to anharmonic and mass substitution effects, these vibrational frequencies of the atomic bonds are dependent on the strain state and Ge fraction of the Si$_{1-x}$Ge$_x$ alloy. This shift between the alloy Si-Si Raman peak and the bulk Si Raman frequency are used to estimate the Ge fraction in the alloy [40, 164] Additionally, another broad band around 75$-$110 cm^{-1} has been observed in Lu's work and identified as due to transverse acoustic modes [163].

Lattice characteristic corresponded to two vibrational modes either optical or acoustical. In the optical mode, atoms of opposite charge vibrate out of phase to give an oscillating dipole moment which couples to light. In the acoustical mode, the displacement of both atoms has the same amplitude, direction and phase. The acoustic branch frequency increases linearly and the slope represents the group velocity of phonons. The group velocity of optical phonon modes is negligible and therefore, they do not contribute to the heat transport. Each type can be either transverse or longitudinal. Resonant absorption occurs when the incoming frequency ω matches transverse optical frequence ω_{To}. These modes also participate in Raman and PL processes, where the two other types of phonons— transverse and longitudinal acoustic (TA and LA)—may also play a role. Each TO mode is usually separately visible in Raman spectra, which gives useful information. In an elemental semiconductor like silicon or germanium, where the charge does not alternate

sign from atom to atom, the TO and LO modes coincide at K = 0 (Figure 3.1). Raman

scattering is also excited by absorbed visible light. It examines TO, LO , and other phonon

modes, which reflect the crystalline state of the semiconductor and give alloy information.

For crystals with the diamond structure, and in the backscattering experimental geometry,

only LO phonons are seen when a (100) surface is examined; only TO phonons appear

from (110) surfaces; and both TO and LO modes appear from (111) surfaces. Lattice

inhomogeneity tends to broaden the Raman peaks [163].

Raman modes strengths depend on the count of harmonic oscillators in the lattice

versus temperature. The temperature affects the number of phonons n_K through the phonon

creation and annihilation, K is the wavevector.

Since n_K follows the Planck distribution function [163]:

$$n_K = \frac{1}{e^{\frac{\hbar\Omega}{k_B}}-1},$$ (3.3)

the local temperature can be calculated by the relative strength of the lines as:

$$T = \frac{\hbar\Omega}{k_B \times ln(I_{stokes}/I_{anti-stokes})},$$ (3.4)

In sum, by studying the vibration of the atoms we can discover the chemical

composition and other useful information about the material. By studying changes in the

details of the spectrum (such as the height, width, and position of the Raman bands) and

determine things, including the relative amount of material, layer thickness, crystallinity, strain, temperature.

3.1.3 Photoluminescence

PL and Raman scattering are both activated by being illuminated by a laser. In most cases, Raman scattering setups are suited to the operation of both Raman scattering and PL. Occasionally PL bands may be strong and broad, masking Raman information. However, PL results may cover the useful information in Raman analysis. By selecting a specific laser wavelength, the Raman bands can be staggered from the PL peaks or even avoid generation of the PL entirely.

PL is the process of absorbing energy and emitting it in the material. PL comprises both fluorescence and phosphorescence processes. Fluorescence is fast in the ns time scale while phosphorescence is slow up to hours or even days. The type and count of PL depends on which laser wavelength is chose and which material is being illuminated.
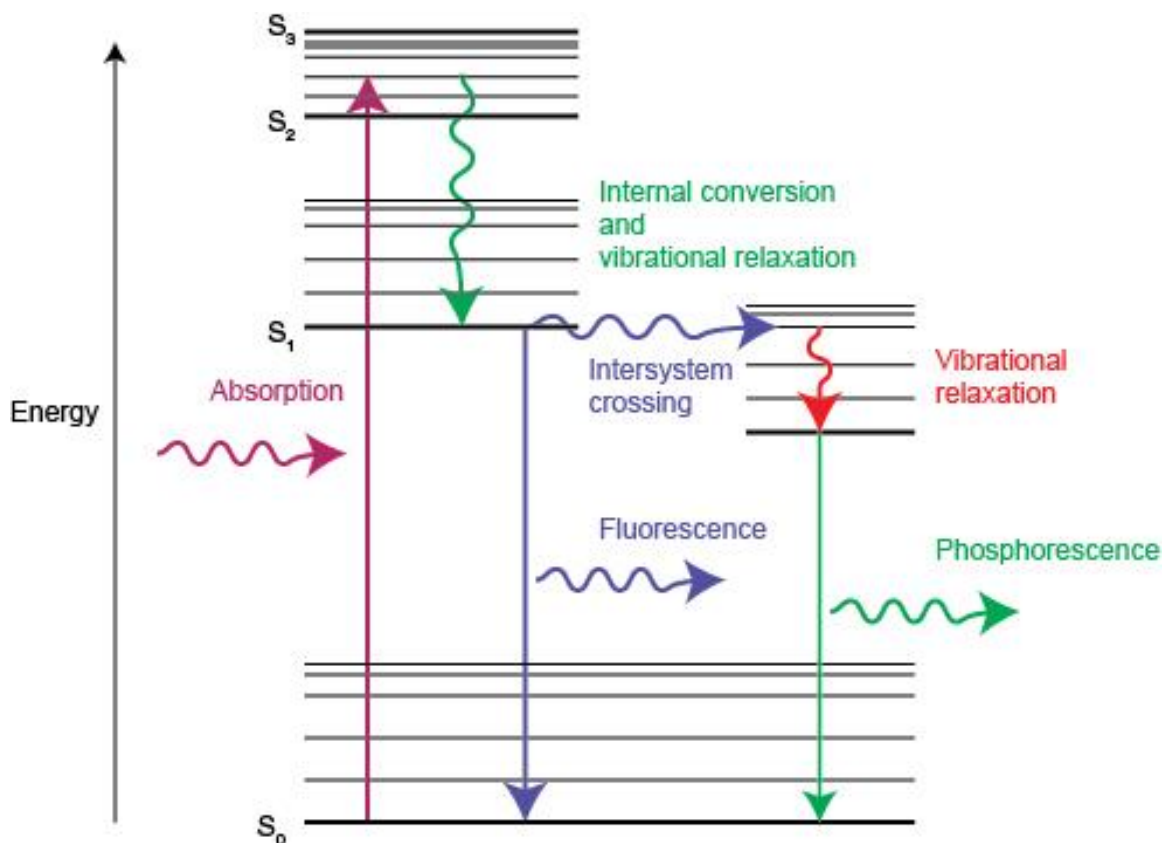
Figure 3.2 The absorption and emission of light in electronic level as fluorescence and phosphorescence.
Source: [165].

Figure 3.2 illustrates diagram in a broad band emission. Both radiative transition and non-radiative transition can help the excited electrons return to the ground state. Radiative recombination accompanied by photons emission is consisting of the returning electron from a luminescent center. This electron jumps from the lowest vibrational level back to the ground state by photon emission.

The excited electron is brought into a high vibrational level and later relax to the lowest vibrational level by giving up energy to the surroundings. This relaxation is non-radiative. Non-radiative recombination mechanisms do not involve the creation of a photon. The Stokes shift is defined as the difference between the wavelengths of the

absorption and emission particles, i.e. the energies between the maximum of the excitation and the emission band (Figure 3.3(a)).

While non-radiative recombination dominates in indirect bandgap semiconductors such as single-crystal Si and Ge due to recombination through phonon assistance for conservation of momentum. The number of photons emitted divided by the number of photons absorbed is equal to the ratio of the measured lifetime to the radiative lifetime [167]. As a result, the radiative recombination lifetime is much longer and indirect bandgap semiconductors exhibit poor photoluminescence efficiency [166]. Other non-radiative recombination process can be through a defect or trapping level. Strain in semiconductors lowers the energy bandgaps of the materials, and as a result, the PL spectra shift toward lower photon energies. That is the reason why for semiconductor materials, PL can be used to study not only bandgap and crystal defects, such as atomic vacancies and substitutions as well as internal strain.

By the crossing of the parabolas, electrons jump to the ground state without photon emission (Figure 3.3(b) (I)). The energy is dissipated to the lattice of materials. In (Figure 3.3(b) (II)), the parabolas of ground state and excited state are parallel. If the energy difference is equal to or less than four to five times the higher vibrational frequency of the surrounding, it can simultaneously excite a few high-energy vibrations, and therefore is non-radiative [167]. Both radiative and non-radiative processes are possible in a three-parabola diagram as shown in Figure 3.3(b) (III). Emission occurs by transporting to the upper excited state (dash line) then relaxing to excited state of the second excited parabola (solid line).
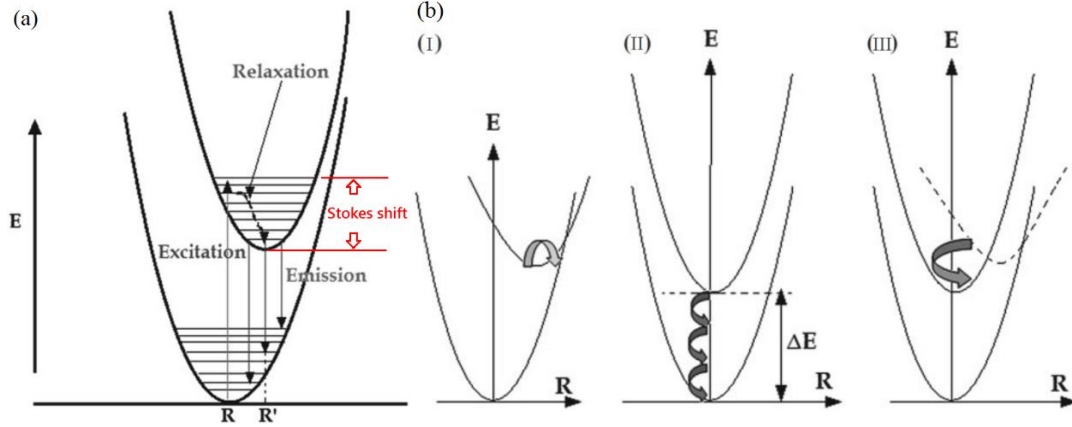
Figure 3.3 (a) Configurational coordinate diagram in a luminescent center and (b) Configurational coordinate diagram representing non-radiative transitions.
Source: [167].

3.2 Measurement Procedures

3.2.1 Optical Measurements

In this research, the SEM images are obtained by using a LEO 1530VP field emission scanning electron microscope in the Material Characterization Laboratories at NJIT. The microscope operates at high voltage mode with voltages ranging from 0.1keV to 30keV, magnification of 20k to 900k times and resolution up to 1 nm. The sample is held in high vacuum on a sample stage that is equipped with motorized controller for moving and rotating laterally, allowing access to multiple samples. The stage also tilts along a central axis with manual control outside the chamber, enabling scans of the sample at angles from -15° to 90°. The images shown in this research are taken by collecting the reflection of electrons with the in-lens detector at moderate voltages of 1k-10k eV.

The chemical composition of the axial Si/Ge NW HJs studied quantitatively by a JEOL JEM-2100F field emission source transmission electron microscope (TEM) operating at 200 kV equipped with an Oxford INCA EDX with a probe size of 0.2 nm.

EDX provides a fast and nondestructive analysis a sample at a single point, along a line or over a plane. The EDX spectra of axial Si/Ge NW HJs shown in this dissertation are done in NRC, Canada using an Oxford INCA Energy TEM 200 attached to the JEM-2100F and electron energy loss spectroscopy (EELS) using a Gatan GIF Tridiem attached to the JEM-2100F. The EDX spectra are calibrated by probing axial Si/Ge NW HJs interface of known germanium composition [17].

Optical measurements were performed in Dr. Tsybeskov's Lab, NJIT. Raman scattering measurements are performed using a Jobin Yvon U1000 double-grating, 1 meter focal length monochromator with a thermoelectrically cooled Hamamatsu R943–02 PMT and a photon counting system via the backscattering geometry. The Raman system spectral resolution is up to 0.25 cm^{-1}. In order to analyze polarized Raman scattering, a rotating thin-film polarizer has been used. A continuous-wave (CW) multi-line Ar$^+$ laser has been used as an excitation source with the focused laser spot size of 50 x 50 μm^2. Ar$^+$ laser providing power from the ultraviolet to the green is a good choice in giving flexibility in penetration depth, and a limited ability to excite resonance Raman scattering. The laser light incident angle is close to Brewster's angle and the measured reflection is ≤ 3%. In these experiments, the excitation intensity has been varied from 10^2 to 10^3 W/cm^2 in a spectral range (200-600 cm^{-1}).

Figure 3.4 shows the experimental setup for Raman measurements. Raman spectra are recorded at room temperature using an Ar$^+$ laser as an excitation source. The used excitation wavelengths were 458, 477, and 514 nm. The measurements are performed with the incident light at an angle close to ~ 78° (Brewster angle in c-Si), and the laser beam was focused to a spot of approximately 10 μm in diameter. The laser power varied from ~1 W

(514.5 nm) to ~0.3 W (457.9 nm) and the power on the sample was ~ 200 mW at 458 nm excitation wavelength with 30 μm slit width. The scattered light from the sample is focused onto the entrance slit of 150 μm of a Jobin Yvon U1000 double monochromator with 1 m focal length [168] and detected by a thermoelectrically cooled Hamamatsu R943-02 PMT and a photon counting system. The PMT has wavelength range at maximum spectral response of 300 – 850 nm and a dark current of 20 counts per second [169]. The Raman system spectral resolution is ~ 0.5 cm^{-1}.
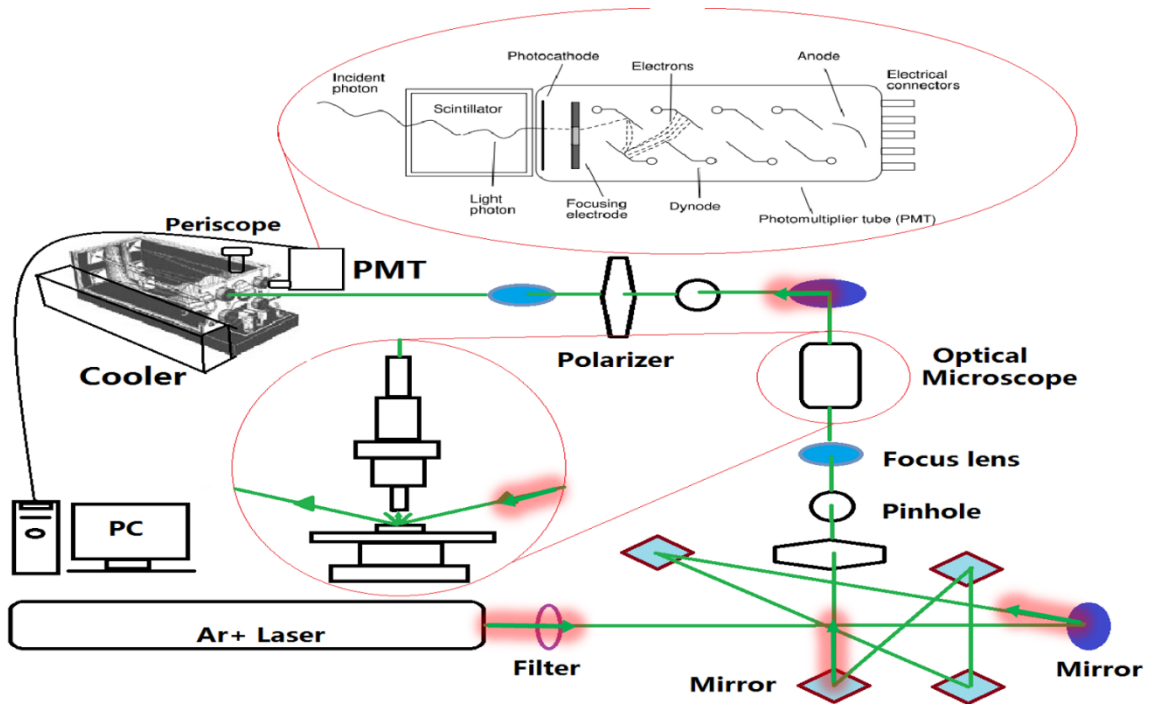
Figure 3.4 Experimental setup for Raman measurements.

The PL source can be any laser whose photon energy exceeds the bandgap of the material to be examined, and whose power is sufficient to excite an adequate signal. Many commercial types of laser including HeNe and Ar + units meet these criteria. But laser power cannot be increased indefinitely, since too high an intensity (watts per square

centimeter) at the focused spot can damage a sample. It is usually possible to obtain an adequate signal-to-noise ratio without damage, by defocusing the laser or reducing its output power. The PL signal passes through a single-grating monochromator which selects a wavelength to transmit to the detector [162]. The resolution of the system, its ability to accurately measure energy, is determined by the focal length of the monochromator, whereas the grating spacing sets the wavelength coverage. Even a modest 0.22m monochromator with a 1200groove/mm grating covers the visible to the near infrared with an energy resolution of approximately lmeV at mid-range. Much higher resolutions are available. A standard photocathode tube with the common S-l response is often adequate for PL work below 1.1μm (above 1.1eV). At longer wavelengths a photomultiplier tube with a GaAs or other composite cathode is useful. Germanium photodiodes are good for the near-infrared range (1.1-1.8μm, 0.7-1.1eV). For the best signal-to-noise ratio these detectors should be operated cooled, at 0°C for a photomultiplier, and at 77 K for a solid-state photodiode. The best PL spectra come from samples held below room temperature. Lower temperatures reduce the thermal broadening of the excited carrier energies, which at temperature Γ is roughly k_BT, where k_B is Boltzmann's constant. This gives a significant broadening of 25meV at room temperature, which reduces to 6 meV at 77 K, and to < 1meV at liquid-helium temperatures, for the finest work. Cooling therefore produces sharper, more readily identified peaks. It also tends to reduce the role of competing non-radiative paths for recombination, giving a higher efficiency for the PL process which results in improved signal-to-noise ratio. Finally, cooling prevents impurity centers from undergoing thermal ionization.

PL measurements are performed at normal incidence with a light spot of $50*50\ \mu m^2$ using a single-grating Acton Research 0.5m focal length monochromator and detected by a Ge photodetector or by a thermoelectrically cooled InGaAs photomultiplier operating in the 0.9-1.65μm spectral region. The samples are held in a He closed-cycle cryostat, wherein the temperature can be controlled in the range of 10 to 300 K. A multi-line Ar+ laser with a wavelength selector is used as excitation source with intensity varied from 0.l to 10W/cm^2. The laser is modulated by a mechanical chopper. The PL signal is dispersed using a single grating Acton Research 0.5 m focal length monochromator and detected by a cooled InGaAs PMT or charged-couple device (CCD) camera in the range of 0.9-l.6pm. The dispersed signal is amplified by a lock-in amplifier in reference to the mechanical chopper and recorded by Spectra Sense software.

3.2.2 Electrical Measurements

For the electro-optical and electrical measurements of the axial Si/Ge NW HJs, the top contacts are fabricated through dropping silver paste as droplets on the top of NWs. The back contacts are made by affixing the Si substrate on thin Cu tape with silver paste connecting normal wires (Figure 3.5). As the most common contact metallization method, silver paste have required a unique processing step called "spike firing". Silver paste needs to fire through and etching of the coatings in the top of the NWs. The primary advantage of short spike firing in silver contact formation is to prevent over-penetrating the underneath Au/Ge and p-Si/Si junctions, which would result in reduction of shunting or junction degradation as well as low series resistance [169-171]. Since the length of NW sample is 1500-2000nm, Si/Ge heterojunctions is far enough to be shunted. In the measurement of noise, a sharp probe touching the NW tips with the Au droplets is used,

while second contact can be at a heavily doped Si substrate. The problem is that the NWs have different heights and a large (compared to NWs) metal needle could easily damage the NWs. To avoid this problem, we used a graphite needle with ~ 2-3μm curvature at the tip with a spring, which controls the applied pressure. Graphite is more than 7 times softer compared to crystalline Si, and there is a very little chance to damage a NW. In addition, during the graphite needle move toward the sample with the uneven NW heights, current has been continuously monitored to establish a reliable electrical contact. Using this technique, we were able to perform reproducible electrical noise measurements at room temperature without removing the Ge-Si NWs from the substrate. Analyzing the SEM images, we estimate that our graphite probe is contacting ~ 20-30 NWs. In these measurements, the Ge-Si NWs are connected in 'parallel'; thus the resistance of n Si-Ge NWs contacted by a probe is $R = \left(\sum_{i,n}^{n} \frac{1}{R_i} \right)^{-1}$. Electrical measurements were performed at room temperature using Keithley 6517A electrometer-programmable voltage source. Time-domain and frequency-domain measurements were performed using a Tektronix digital storage MDO4000 Mixed Domain Oscilloscope and a HP 4192A impedance analyzer. Two LabVIEW programs developed for HP 4192A impedance analyzer and KEITHLEY 6517A electrometer are used for automated system data acquisition and measurement control.
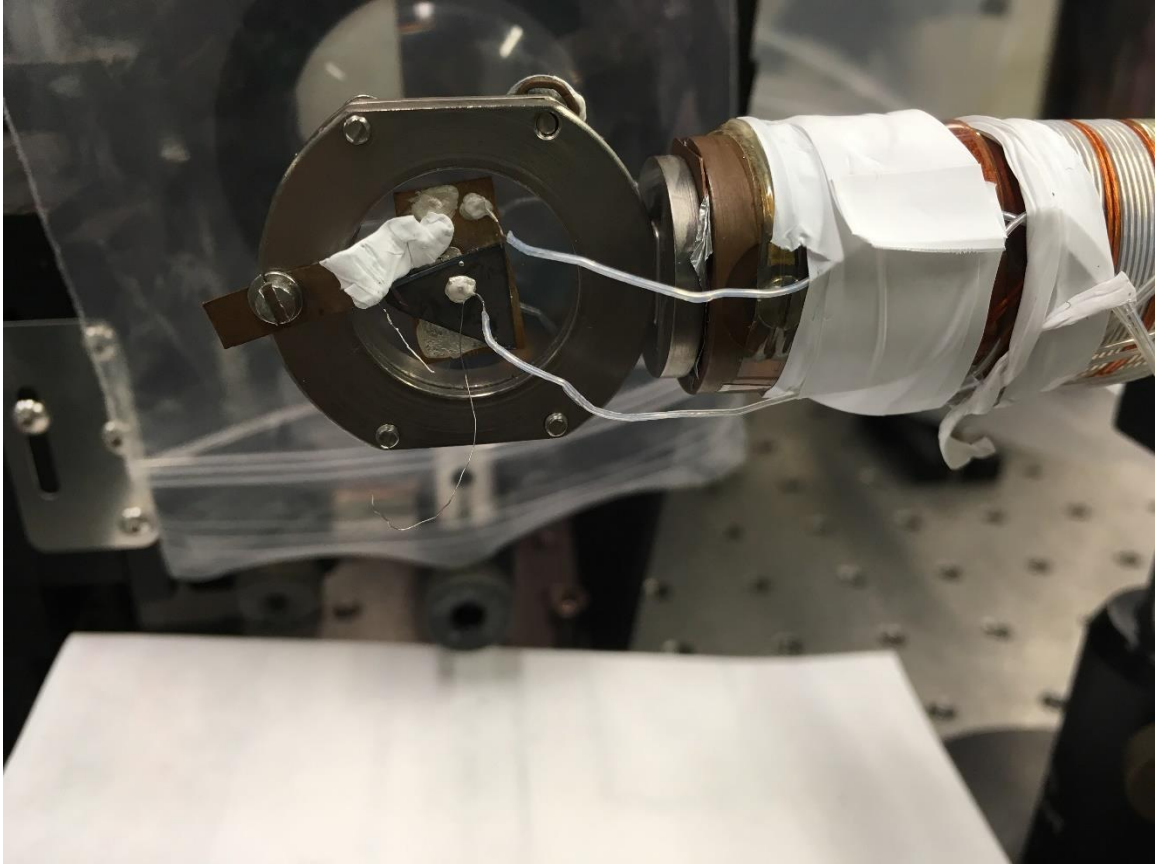
Figure 3.5 Contacts photo of axial Si/Ge NW HJs samples.

CHAPTER 4

RESULTS AND DISCUSSION

This chapter presents experimental data and research results of structural, electrical, optical, and thermal properties of the VLS grown axial Si/Ge NW HJs. In the first section, experimental images of TEM, SEM and EDX will be presented. In the second section of this chapter, the experimental results from PL spectroscopy will be presented. The CW laser has been used for PL excitation and electron-hole recombination schemes have been discussed. In the third section, the quantitative and qualitative analysis of Raman data will be discussed based on the Raman spectra. The Raman peaks at various wavelengths and polarization angles are determined to explain structural, vibrational, and thermal properties of axial Si/Ge NW HJs. The last part of this chapter provides noise, I-V, current oscillation discussion obtained at temperature sweep, frequency sweep and voltage sweep with or without external components.

4.1   Structural Properties of Si/Ge NW HJs

As we mentioned above, scaling of devices is facilitating the tolerance of strain, because of the surface-volume ratio. Nanoscale Si/Ge NW HJs can bear more strain by expanding or bending. Unlike intrinsic strain induced by Si and Ge lattice mismatch, extrinsic strain comes from various reasons, including the temperature difference between room temperature and growth or even illumination high temperature, the pressure, the growth procedure, the substrate, the contact formation process. We demonstrate in this section that

the strain directly modifies structural properties by lateral displacement of Ge without forming structure defects or dislocations.

4.1.1   TEM, SEM and EDX Result

Figure 4.1 shows a moderate resolution TEM image of a single axial Si/Ge NW HJ with a clearly visible Si/Ge heterointerface and smooth NW surface. The diameter of the Si segment of the NW is 105 nm, and it is nearly constant. The diameter of the Ge segment of the NW gradually increases from 105 to 115 nm within 100–150 nm from the Si/Ge heterointerface and then remains constant. The TEM micrograph of a Si/Ge NW HJ shows that Ge is strictly sticking with Si. Lateral nanowire expansion in the vicinity of Si/Ge HJ is clearly observed and marked by the white arrow.

~ 115 nm

Ge

~ 105 nm
Si

20 nm
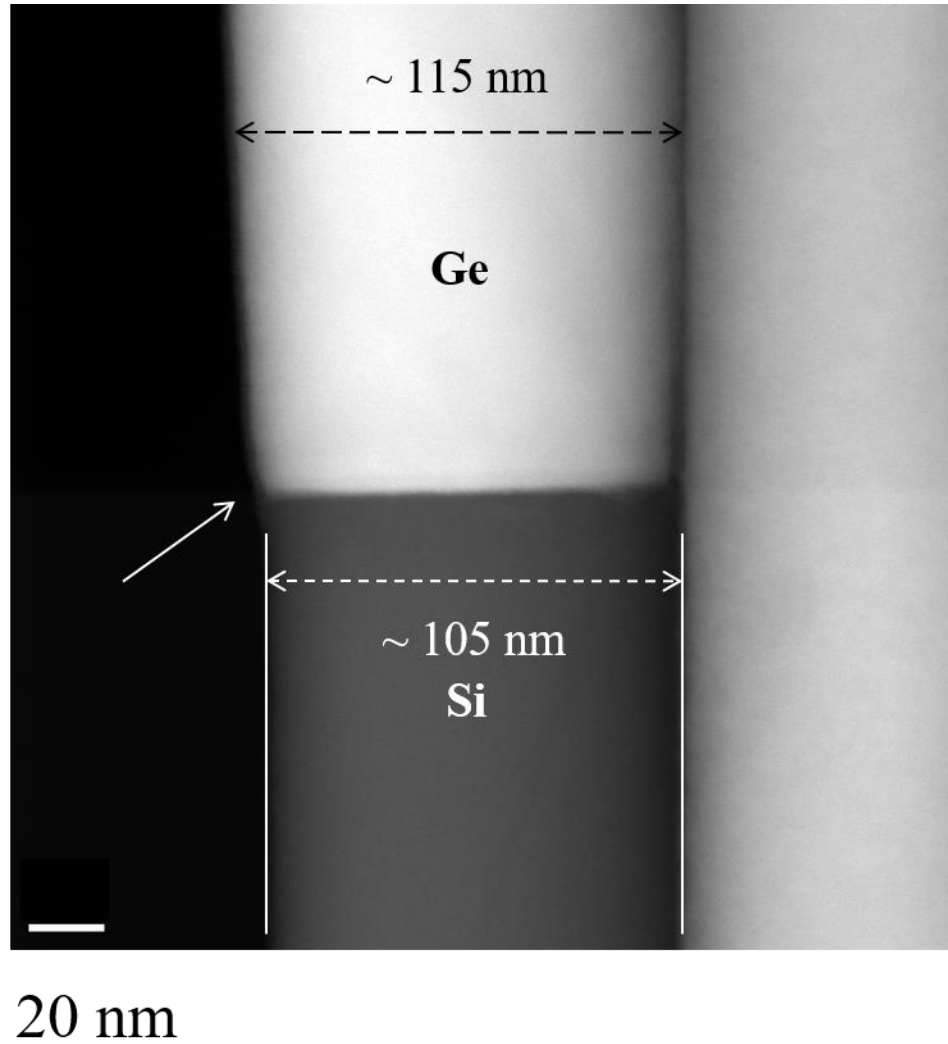
Figure 4.1 TEM image of the axial Si/Ge NW HJ showing an abrupt Si/Ge heterointerface and an increase in the NW diameter from 105 nm in the Si segment to 115 nm in the Ge segment of the NW.
Source: [32].

Figure 4.2 presents a HR-TEM image of the Si/Ge NW heterointerface close to the NW center. The lattice fringe spacing confirms the NW (111) crystallographic direction. The inset shows the corresponding lattice fringe spacing fast Fourier transform (FFT) of the marked area (circle) attesting to the nearly ideal crystallinity of the NW center.
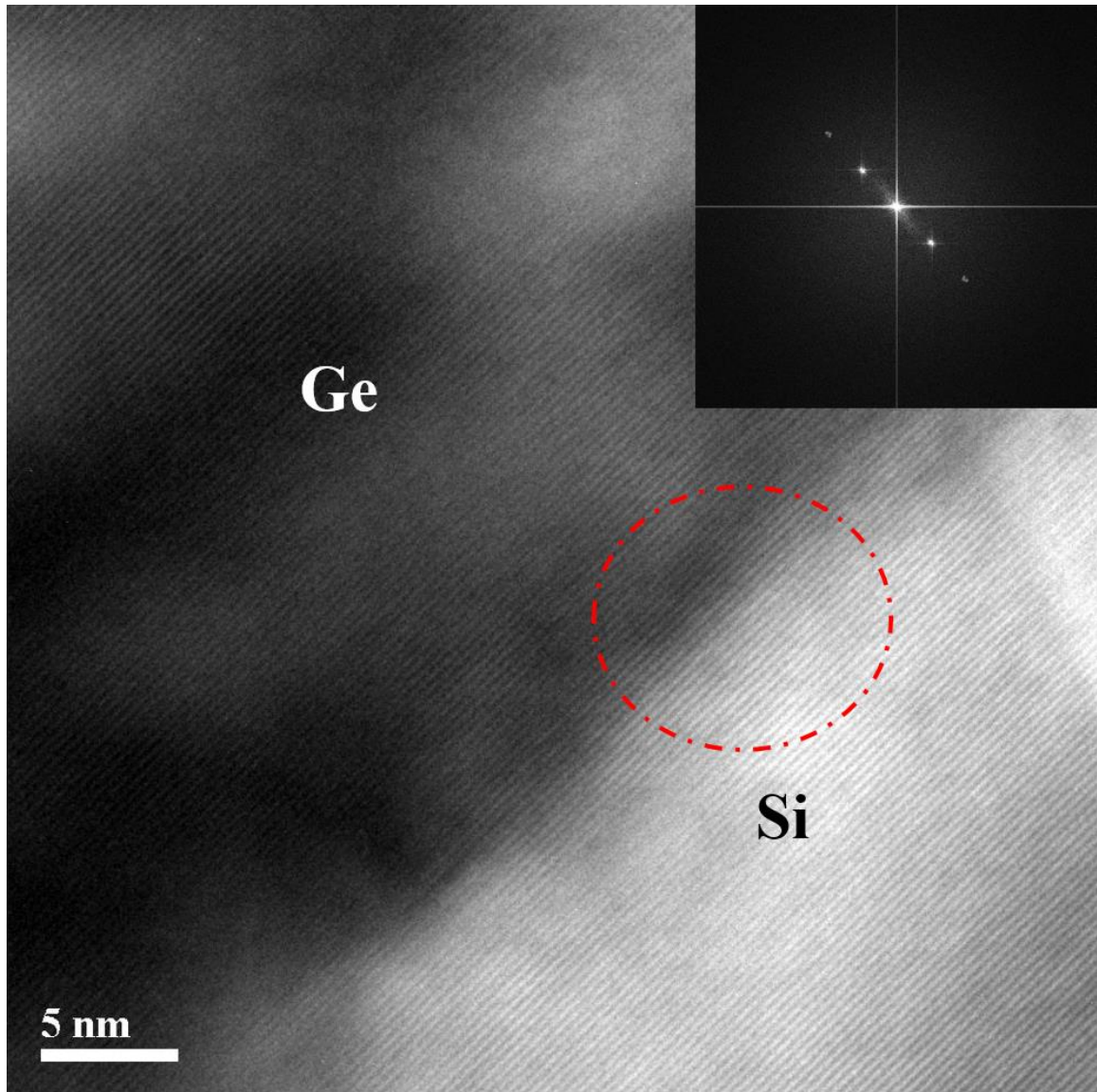
Figure 4.2 HR-TEM image of the Si/Ge NW HJ interface close to the NW center with clearly evident (111) lattice fringes. A fast Fourier transform (FFT) of the circle marked area is shown in the inset.
Source: [32].

Figure 4.3 shows a HR-TEM micrograph of the same Si/Ge NW HJ with focus on the area close to the NW surface where a 1 nm thick amorphous oxide layer can be seen (marked by an arrow) and structural imperfections are confirmed by the FFT analysis (see area marked by circle and inset). Note that no dislocations are observed in the vicinity of the Si/Ge NW HJ. In addition to the observed nanowire lateral expansion, the 4.2% lattice

constant mismatch induced strain could be relaxed by other mechanisms shown in Figure 4.3 including nanowire bending and kinking, formation of structural defects and amorphization. Evidence of strain induced Si and Ge diffusion can be observed at the NW HJ interface. For the strain relaxation via non-dislocation formation and coherent from layer to layer, the critical thickness of Si/Ge is about 5-15 nm depend on the concentration of Ge. That is the additional reason that the diameter of Si/Ge NW HJ is more than 100 nm to cover enough high crystallized area besides all the structure imperfections. The lattice-mismatch is also found to be accompanied a mismatch in CTE, which introduces additional strain, which will be discussed later. Thus, the theoretically predicted surface morphology changes of introduction part near the transition from Si to Ge are confirmed by TEM micrographs.
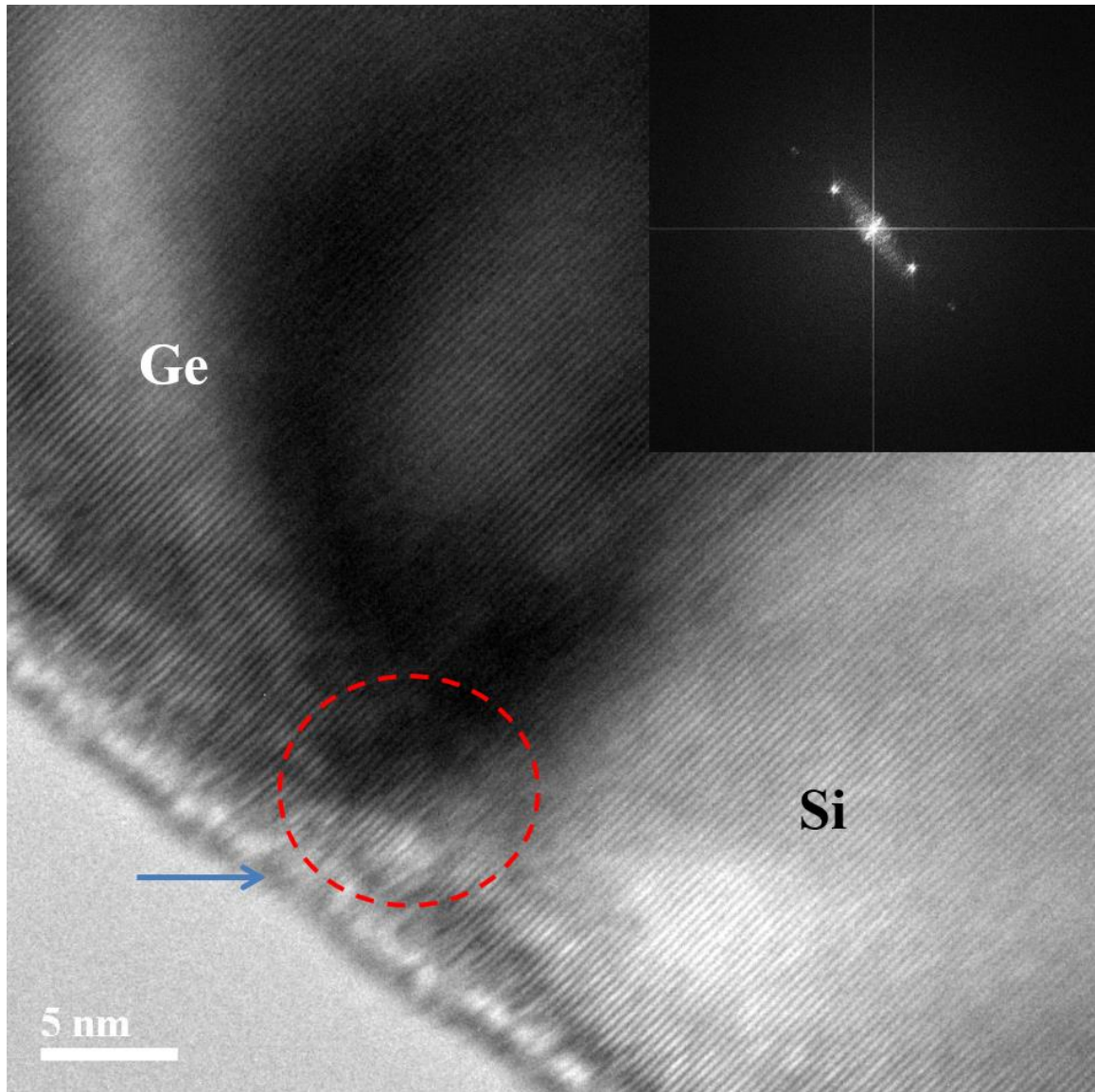
Figure 4.3 HR-TEM image of the Si/Ge NW HJ interface close to the NW surface with clearly observed distortion of the lattice fringes and the corresponding FFT of the circle marked area (inset). An amorphous layer of 1 nm thickness at the NW surface is indicated by an arrow.
Source: [32].

Figure 4.4 (a) shows a SEM image of a sample depicting nearly straight NWs with

a clearly visible interface between the Si and Ge segments (shown by an arrow) and the Au

droplets at the NW tips (indicated). Figure 4.4 (b) shows a bright field transmission electron

microscopy (BF-TEM) image of the Ge-Si heterointerface (Si and Ge segments of the NWs are marked).
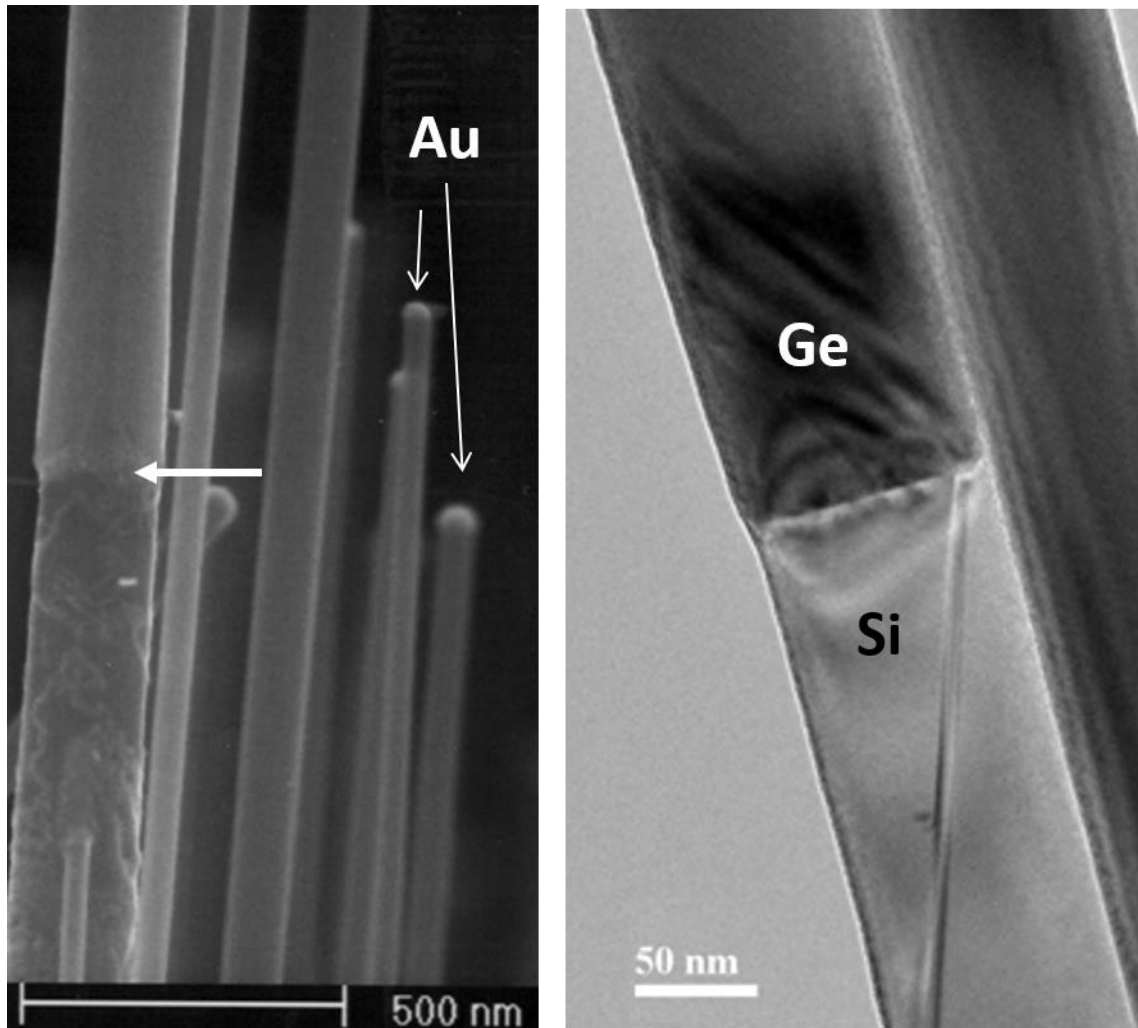
Figure 4.4 (a) SEM image of NWs; (b) BF-TEM image of a HJ.

Results of compositional EDX microanalysis of the Si/Ge NW HJs are shown in Figure 4.5. Similar results were obtained from other EDX scans across the heterointerface near the center and close to the edge of the NW. The Si content is shown in black, while the Ge content is shown in red for comparison, and the direction in which the analysis is done is along the growth direction. The Ge content is gradually decreasing while the Si content is increasing in the measured direction from Ge side to Si side indicating Si/Ge

interface is not abrupt but smooth due to the spontaneous SiGe intermixing found in VLS

grown Si/Ge NW HJs. Pure Si and Ge composed the area ~ 5nm away from the Si/Ge NW

HJ interface. The Si/Ge NW HJ is comprised of Si and Ge NW segments with a clearly

observed ~ 8 nm thick $Si_{1-x}Ge_x$ transition layer produced by spontaneous $Si_{1-x}Ge_x$

intermixing during growth.
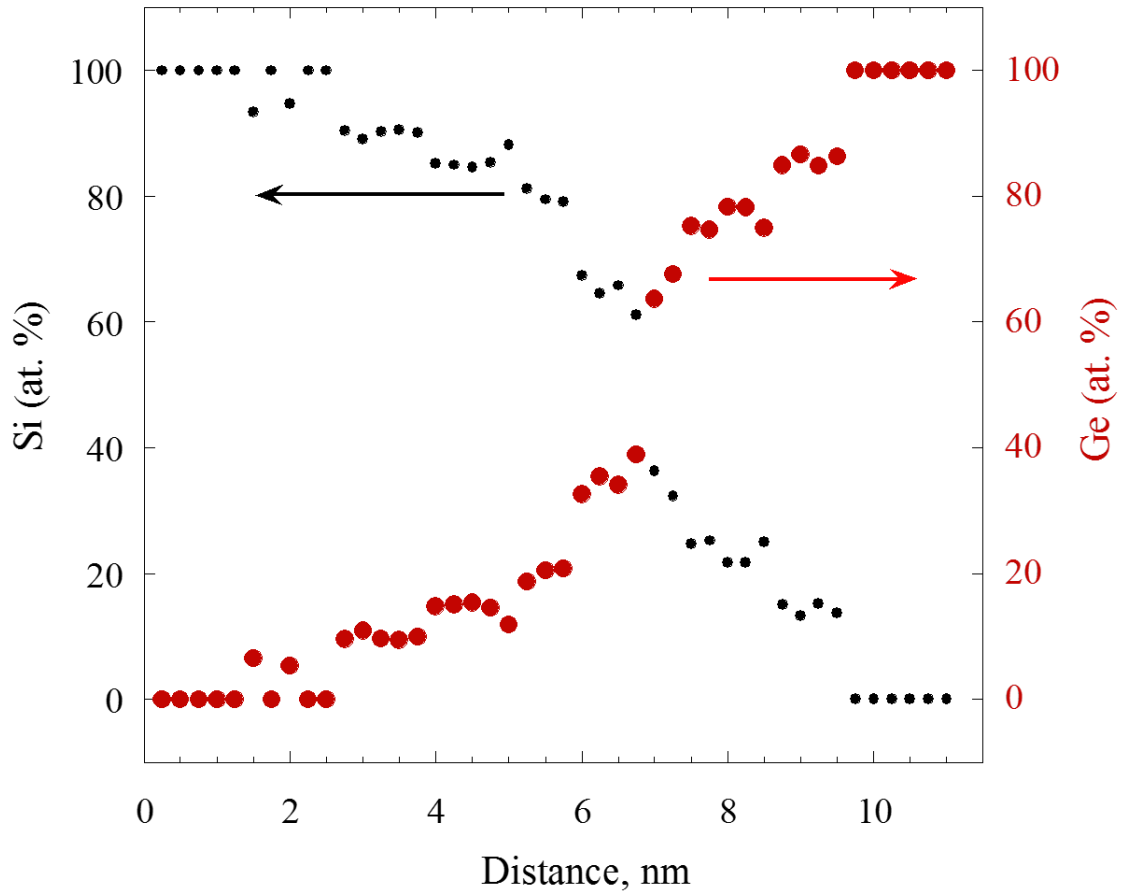
Figure 4.5 Compositional analysis of the NW along the growth direction, showing a spontaneously formed $Si_{1-x}Ge_x$ alloy transition layer at the Si/Ge interface.
Source: [32].

Detailed EDX profile performed as a function of wire distance along the NW HJ

center and the points of intersection where both Si and Ge reached 50 atomic percentage

monotonically move into Ge side (Figure 4.5). This shows the Ge atoms pile-up in one end of shell towards the other, a phenomenon known as Ge condensation. The concentration gradient from Si to Ge within the VLS grown Si/Ge NW HJ is not constant but drops faster in the Si side than in Ge side. And the $Si_{1-x}Ge_x$ alloy composition x does not change uniformly from 0 to 1. Instead, the EDX data suggests the formation of $Si_{1-x}Ge_x$ alloys with preferential compositions of lower x close to the Si part of the Si/Ge NW than x close to the Ge part of the Si/Ge NW. This conclusion, supported by our preliminary TEM analysis, and $Si_{1-x}Ge_x$ composition measurements in $Si/Si_{1-x}Ge_x$ 3D (i.e., cluster morphology) nanostructures where $x \approx 0.2$ is a typical composition of the $Si_{1-x}Ge_x$ wetting layer and $x \approx 0.5$ is a stable composition close to the $Si_{1-x}Ge_x$ cluster core [55]. The EDX signal is noisy due to the rather short acquisition time, the atomic Si and Ge concentration profiles are therefore also noisy. This EDX profile shows the layer composition and local strain relaxation is not uniform from left to right as well as from bottom to top (Figure 4.5), because of the inter-diffusion during growth.

The EDX data indicate that a 2nm thick $Si_{0.8}Ge_{0.2}$ layer is formed close to the Si segment of the NW, and this is known to be a stable $Si_{1-x}Ge_x$ alloy composition produced by spontaneous intermixing [[172, 173]]. This is an interesting observation, because the Ge segment of the NW is deposited using a relatively low (350 C°) deposition temperature. The concentration gradient from Si to Ge within the VLS grown Si/Ge NW HJ is not constant. Most likely, this $Si_{1-x}Ge_x$ transition layer is a result of the presence of residual Si atoms in the eutectic Si/Au alloy after switching to Ge deposition and strain-driven interdiffusion.

4.2 Optical Properties of Si/Ge NW HJs

Two different measurement techniques (Raman and PL) were used to investigate the significant peaks in Si/Ge NW HJs under CW laser excitation. An Ar+ laser (514 nm, 488 nm, 457.9 nm, and a multi-line), a HeCd laser (325 nm), and high-power light-emitting diode with a peak near 365 nm are used. PL dynamics using a Q-switched Nd:YAG pulse laser of 355 nm excitation wavelength were studied. The excitation energy density was varied from 1.5 to 50 mJ/cm^2. We demonstrate in this section that the mismatch in Ge and Si CsTE and low thermal conductivity of Si/Ge NW HJs are proposed to be responsible for the thermally induced stress detected under intense laser radiation in photoluminescence and Raman scattering measurements.

4.2.1 Photoluminescence

Figure 4.6 compares the normalized Si/Ge NW PL spectra to the c-Si PL spectrum measured at the same (T = 20 K) temperature. The Si/Ge NW PL spectra clearly exhibit at least two peaks. A narrower PL peak at ~1.08 eV (PL1) and a broader PL peak at ~1.03 eV (PL2) are clearly observed, and only a very weak PL signal with photon energies close to the bulk c-Si transverse optical (TO) PL peak at 1.1–1.15 eV is found at T = 20 K (marked by an arrow in Figure 4.6). Note that no PL associated with c-Ge at 0.7–0.65 eV has been detected. The relative intensities and spectral positions of the two major PL peaks are found to be temperature dependent (Figure 4.7). Both PL peaks change their positions significantly with temperature. The PL1 peak is detectable even at room temperature and exhibits an asymmetric broadening, which (in agreement with Ref.[174]) can be fitted using Boltzmann thermal broadening on the high photon energy side of the PL spectrum (not shown). The PL peak position temperature dependence is unusual and will be

discussed later. Note that a reliable detection of the PL signal at room temperature requires

an excitation intensity of ~ 600 W/cm^2.
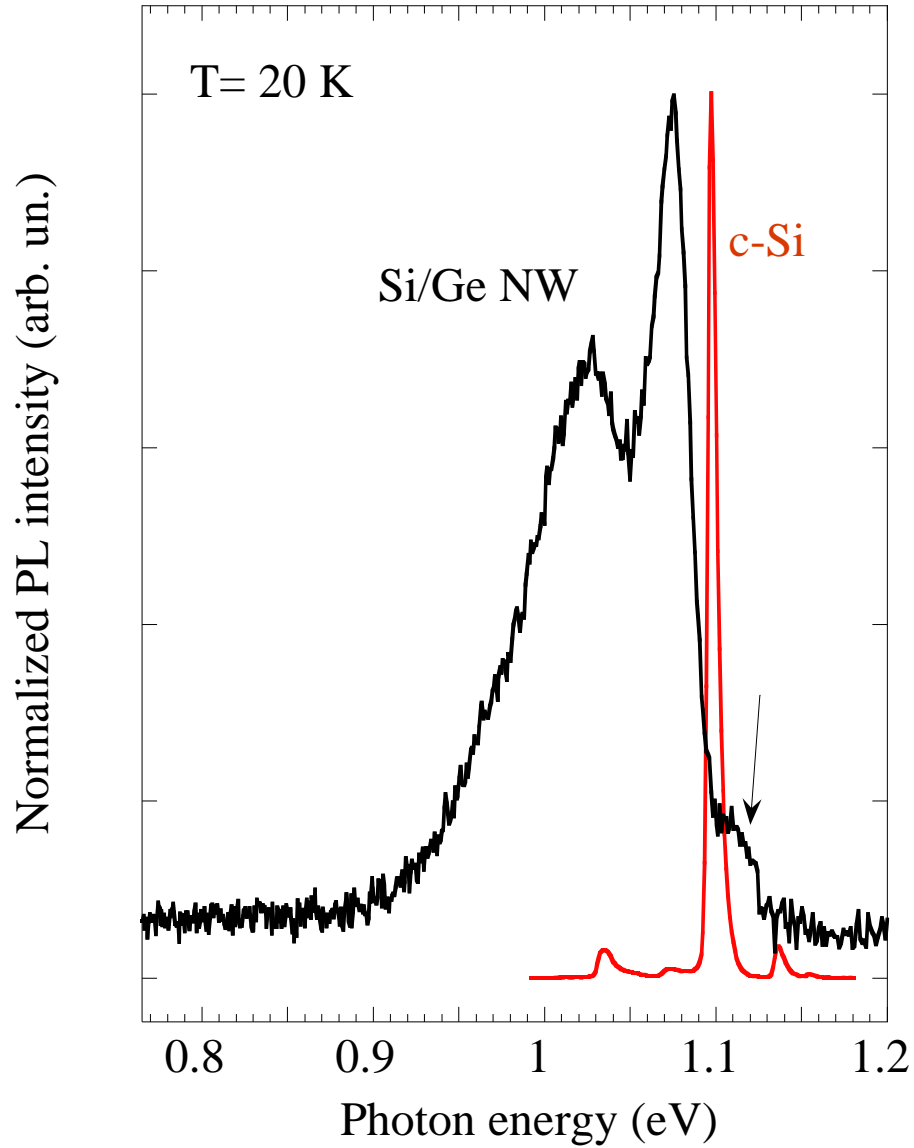
Figure 4.6 Comparison of PL spectra of the Si/Ge NW HJs and c-Si.
Source: [32].

We do not find any significant PL at energies close to the c-Ge energy gap, most

likely due to the following reasons. Both of the Si and Ge segments of the HJs exhibit high

crystallinity (Figure 4.2) and, therefore, should have reasonably long carrier diffusion

lengths, similar to that in bulk Si and Ge. Also, both segments are covered by a thin amorphous oxide layer with visible imperfections near the NW surface (Figure 4.3). Since Si and Ge are both indirect bandgap semiconductors with a long carrier radiative lifetime, excitons/electron-hole pairs have enough time to diffuse toward the surface and recombine at surface defect states, mostly non-radiatively. The GeO_2/Ge interface is more defective compared to the SiO_2/Si interface, and thus no PL associated with the pure Ge segment of the NW is observed [57].
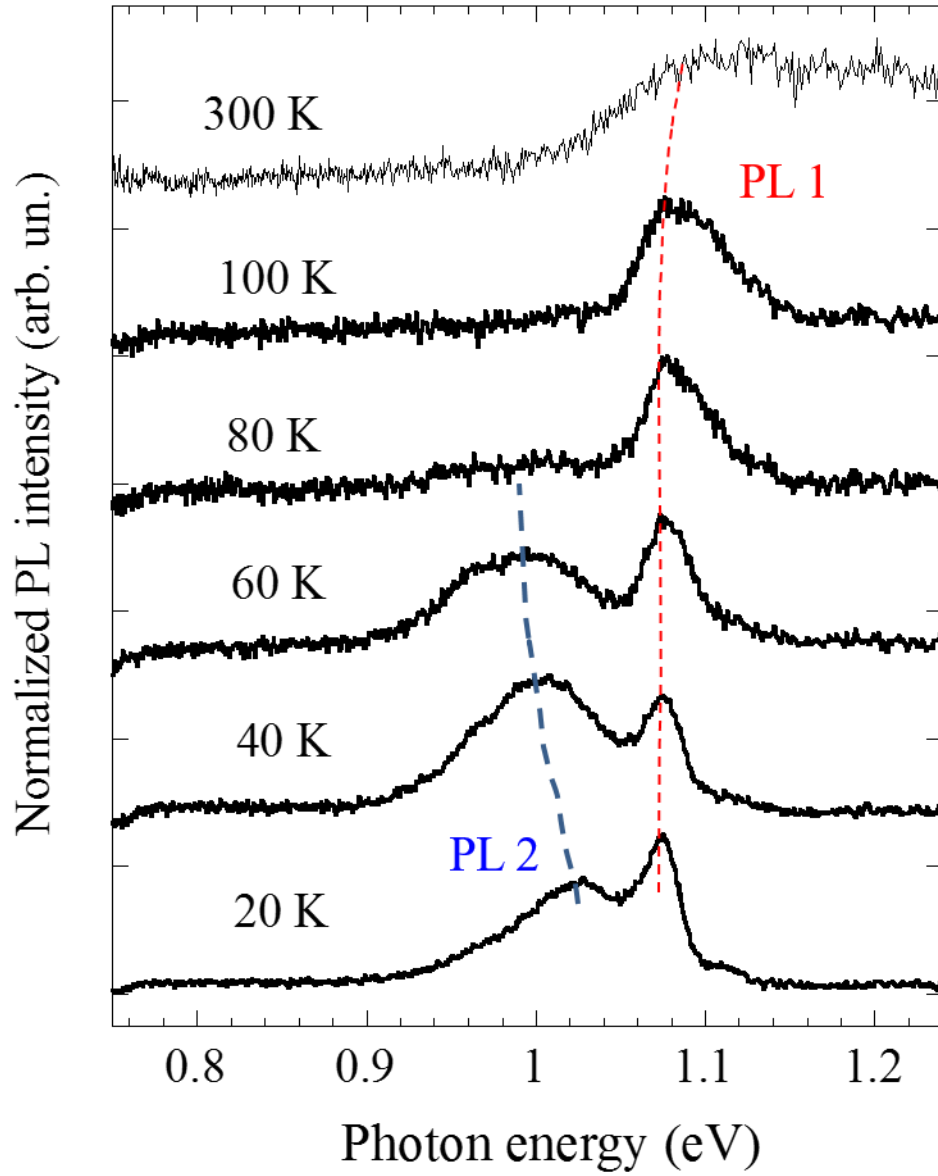
Figure 4.7 The PL spectra of the Si/Ge NW HJs at various (marked) temperatures. The major PL peak shifts with temperature increase are indicated by the dashed lines.
Source: [32].

In the Si segment of the NW, our TEM studies detect a 15-20 nm long strained Si region close to the Si/Ge NW heterointerface. The PL1 peak at 1.08 eV, most likely, is associated with this strained Si region where the energy gap is slightly narrower compared

to that in c-Si [110]. The narrower energy gap Si region of the NW collects excitons (and/or electron-hole pairs) quite effectively. This process is even more efficient at the Si/Ge heterointerface, where the ~ 8 nm thick $Si_{1-x}Ge_x$ alloy layer is found. In $Si_{1-x}Ge_x$ alloys and nanostructures, compositional fluctuation is known to be responsible for low-temperature exciton localization [175]; therefore, exciton diffusion toward the surface is suppressed. Also, $Si_{1-x}Ge_x$ compositional fluctuation is responsible for the reduction of the exciton radiative lifetime [176]. Thus, the low-temperature PL peak at 1.03 eV (PL2) is attributed to radiative recombination of excitons localized at the ~ 8 nm thick $Si_{1-x}Ge_x$ NW heterointerface [55]. This conclusion is supported by the PL2 peak temperature dependence: the PL2 peak disappears at T > 80 K, and this is consistent with a less than 10 meV SiGe composition-fluctuation-related exciton localization energy [173,174].
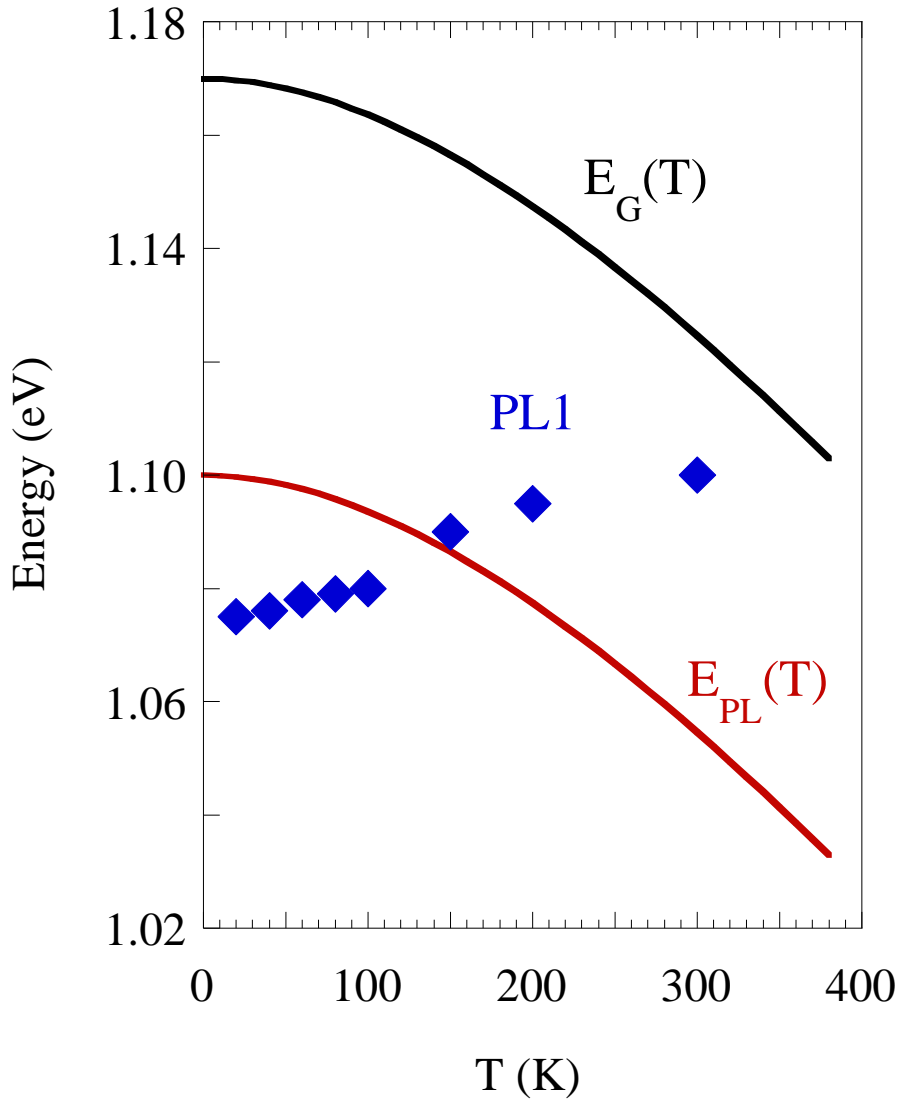
Figure 4.8 Temperature dependencies of c-Si energy gap, c-Si PL peak position, and PL1 peak position in Si/Ge W HJs.
Source: [32].

Considering the PL peak position temperature dependence, the PL peak associated with band-to-band radiative recombination should follow the energy bandgap temperature dependence $E_G(T)$. In bulk c-Si, the PL peak energy position and line-shape temperature dependencies are explained by taking into account the exciton binding energy ($E_{exc} \approx 10$

meV), the phonon-assisted nature of the band-to-band recombination involving mostly TO phonons ($E_{ph} \approx 60$ meV) and the temperature dependence of population of energy states in the energy bands [32]. Thus, the band-to-band recombination related PL peak photon energy is $E_{PL} = E_G - (E_{ph}+E_{exc})$, and in bulk c-Si at low temperature it is close to 1.1 eV. The temperature dependencies of $E_G(T)$ and $E_{PL}(T)$ in c-Si are shown in Figure 4.8.

In Si/Ge NW HJs, the two major PL peaks exhibit a very different dependence on temperature. As the temperature increases, the PL1 peak shows an almost continuous shift toward higher photon energies (Figure 4.8), and above 170 K it crosses the expected bulk c-Si PL peak position. Assuming that this PL is associated with band-to-band recombination within the Si NW segment, this behavior indicates the presence of significant thermal stress. Note that at elevated temperatures (T > 250 K), the PL intensity decreases significantly. Thus, the PL measurements require a high ($\geq$ 600 W/cm^2) excitation intensity, and laser induced NW heating takes place, which is discussed below. Also, at elevated temperatures a broad and weak PL peak appears at 1.2 -1.25 eV, which is most likely associated with NW surface defects, and it becomes comparable in intensity with the PL1 peak (see the PL spectrum at 300 K in Figure 4.7).

We find that the PL2 peak (presumably associated with the NW Si/Ge interface region) follows the direction of the Si CTE temperature dependence. As temperature increases from 20 to 60 K, the Si CTE first decreases and then increases with a minimum around 70 K [177], while the Ge CTE monotonically increases (Figure 4.9). We believe that the PL2 peak position is affected by temperature dependent strain in Si/Ge NW HJs due to the large difference in the Si and Ge CTE temperature dependencies [55].
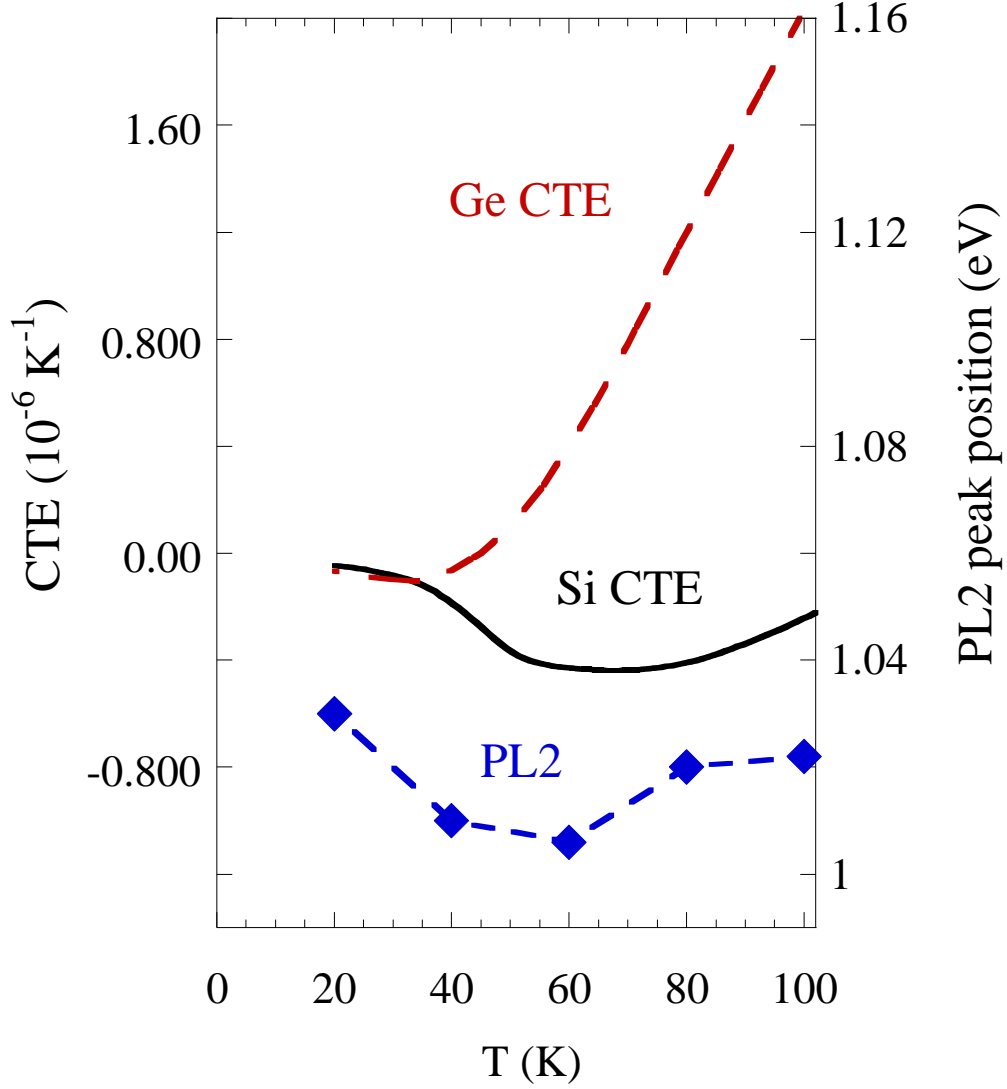
Figure 4.9 Comparison of the temperature dependences of the coefficient of CTE in c-Si and c-Ge and the PL2 peak position in Si/Ge NW HJs. Note that the experimentally measured temperature is the sample holder temperature.
Source: [32].

4.2.2 Raman Scattering

Figure 4.10 shows first-order Raman spectra in Si/Ge NW sample covering a spectral range of 200-600 cm^{-1} at three excitation wavelengths of 458nm, 477nm and 514nm. Raman spectra are normalized and the signal-to-noise ratio is approaching 10,000. We observed

three main Ge-Ge (at ~ 300 cm^{-1}), Si-Ge (at ~ 410 cm^{-1}) and Si-Si (at ~ 520 cm^{-1}) Raman features and two weak peaks centered near 280 cm^{-1}, 500 cm^{-1} (Figure 4.10), emerge in the highest (514nm) and lowest (458nm) excitation wavelengths we have. The intensity of non-resonant Raman scattering is proportional to the scattering volume associated with the light penetration depth from the sample surface, and the light penetration depth in our samples strongly depends on excitation wavelength. As the excitation wavelength increases, the light penetration depth increases, and a low intensity Raman signal is from Si-Si mode at 520 cm^{-1} is observed with excitation at 514 nm compared to 458 nm, while a high Raman signal from Ge-Ge mode at 300 cm^{-1}. The low (~ 300 cm^{-1}) and high (~ 520 cm^{-1}) frequency features connect to the modes of the pure Si and Ge crystals, respectively. The intermediate mode is intimately related to a mode observed in Si/Ge superlattice structures when the Si/Ge interface is rough. Raman spectra confirm strong SiGe intermixing (the peak near 410 cm^{-1}). Interestingly, this Raman peak of Si-Ge mode at ~410 cm^{-1} is slightly shifted to higher wavenumbers under 458 nm laser excitation compared to that under 514 nm excitation, and which is most likely due to the resonant effect in Raman scattering. The softening with respect to Si-Si stretching in the pure Si crystal, the shoulder of the 520 cm^{-1} peak, corresponding to the main Si-Si Raman feature in the alloy (~500 cm^{-1}), is attributed to a mode effect due to the quasi inert Ge atoms with a large mass. A common feature with previous calculations of Alonso and Winter [178] is that, globally, the Si centered units with increasing number of Ge atoms at the vertices tend to generate Raman signals at lower frequencies. This broad Raman peak near 500 cm^{-1} associated with Si-Si vibration in $Si_{1-x}Ge_x$ indicates a nonuniform strain, while the Raman signal associated with the Si substrate is found at 520 cm^{-1}. The vibration pattern of local

Ge-Ge stretching (~280 cm^{-1}) close to Si generated by the Si-induced strain is just identical to that found for the local Si-Si mode (~500 cm^{-1}) close to an isolated Ge atom in Si. A weak feature below 260 cm^{-1} is attributed to a superposition of 2TA and disorder-induced 1LA contributions. The latter includes local strain effects by higher-order interatomic force constants.
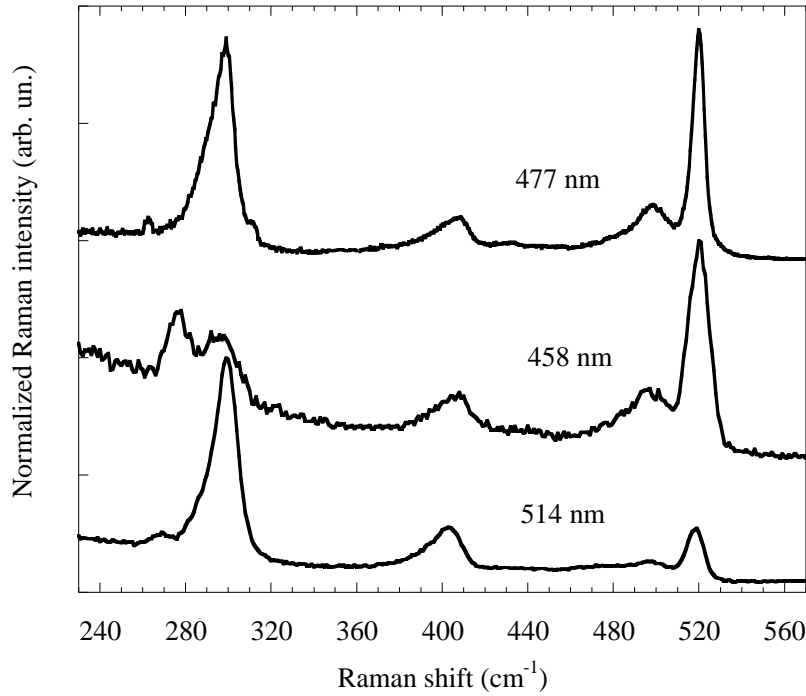
Figure 4.10 Raman spectra at room temperature measured using 458nm, 477nm and 514nm excitation in Si/Ge NW sample.

Figure 4.11 shows Raman spectra of Si/Ge NW HJs measured using argon laser excitation at different wavelengths. Under 514.5 nm excitation, we observe three distinct Raman peaks associated with Si-Si (~ 520 cm^{-1}), Si-Ge (~ 400 cm^{-1}) and Ge-Ge (~ 300 cm^{-1}) vibrations with the main Raman peak at 300 cm^{-1}. Using 458 nm excitation, we find the same peaks but with the main Raman peak at ~ 520 cm^{-1}. This difference is due to a strong

spectral dependence of the Raman scattering cross-section and well-known Raman resonances in Ge at 2.2-2.5 eV associated with E_1 and $E_1+\Delta_1$ optical transition [179]. Note that a peak at ~ 280 cm^{-1} is, most likely, an argon plasma line. A Raman peak at ~ 500 cm^{-1} is best observed using 458 nm excitation and is associated with the Si-Si vibration in the presence of a neighboring Ge atom or Si-Si(Ge) [179]. The Raman spectra are also sensitive to the excitation intensity.
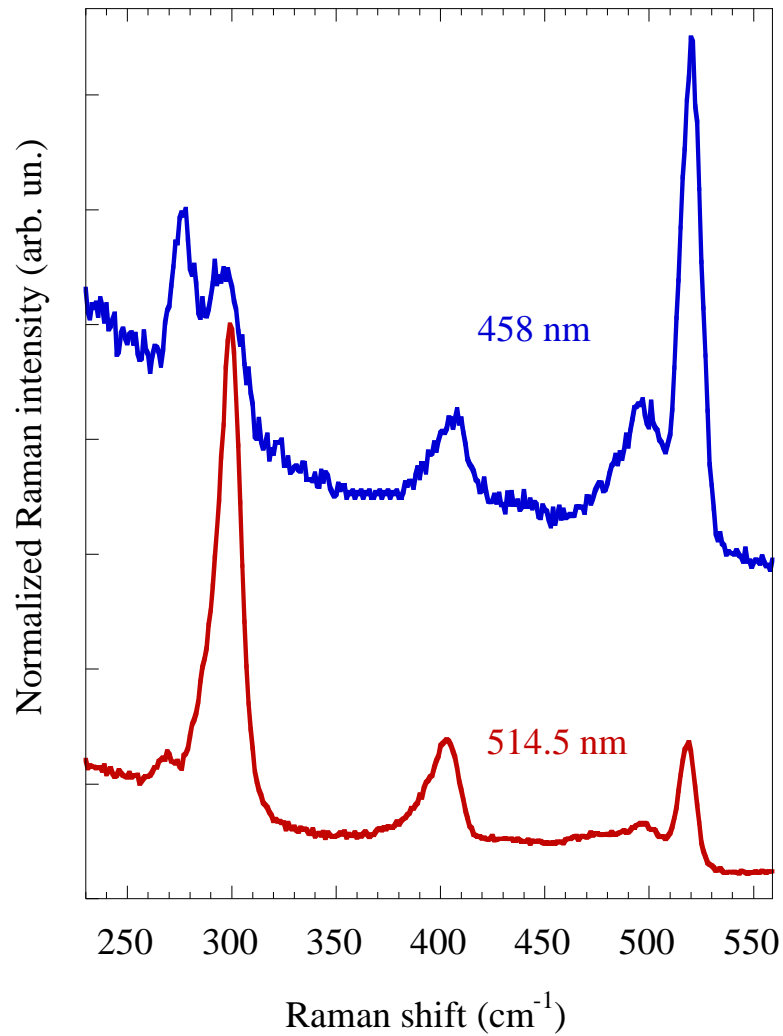
Figure 4.11 Raman spectra of Si/Ge NW HJs obtained under different (indicated) excitation wavelengths.
Source: [32].

Raman spectra are measured using various excitation laser power in the range of 6-40 kW/cm^2 (Figure 4.12) and find significant changes in the relative intensities, FWHMs, and positions of Raman peaks associated with the major Si-Si vibration mode and local Si-Si (in the presence of Ge) mode. As the excitation intensity increases, the major Raman peak at ~ 520 cm^{-1} broadens and shifts toward lower wavenumbers (similar behavior is observed for the Raman peaks at 400 and 300 cm^{-1}, not shown). However, with increasing excitation intensity the Raman peak at 500 cm^{-1} shifts in the opposite direction.
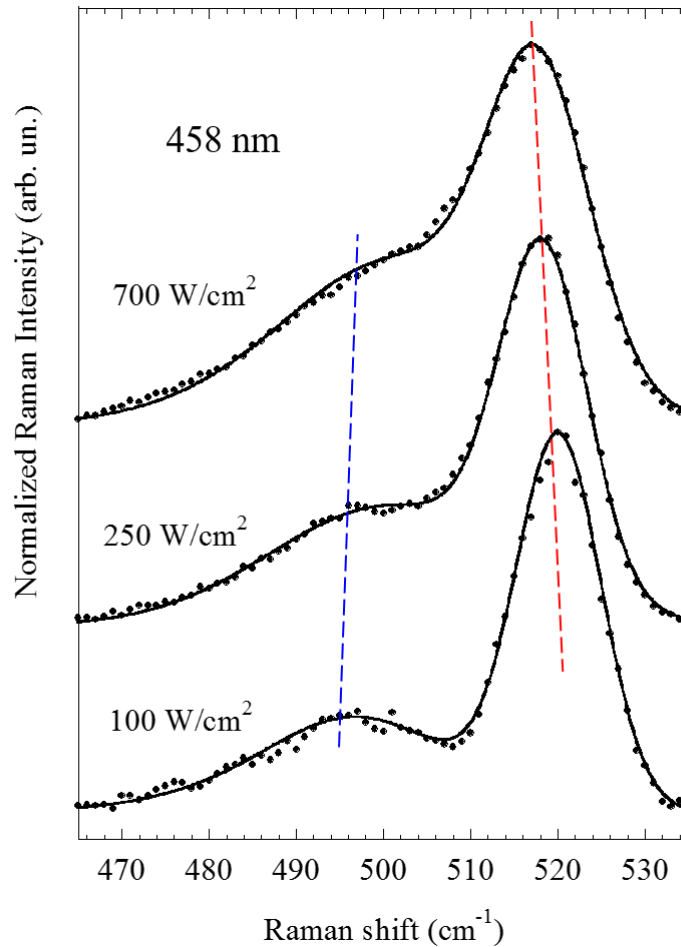
Figure 4.12 Background-corrected Raman spectra obtained under 458nm wavelength excitation and different (indicated) excitation intensities.
Source: [32].

Figure 4.12 shows Raman spectra recorded using three different excitation intensities. We curve fitted these two peaks using a Voigt profile to estimate the peak positions and FWHMs accurately. The results of fitting including the Raman peak spectral position, full width at half maximum (FWHM) and ratio of integrated intensities for Raman peaks at 520 and 500 cm^{-1} as function of excitation intensity are shown in Figure 4.13. Fitted data are used to plot Raman peak positions and FWHMs in the function of laser powers respectively (Figure 4.13(a) and (b)). Using curve fitting, we find that the peak frequency of major Si-Si vibration mode peak shifts considerably from 520.14 to 517.55 cm^{-1} when the laser excitation power increases from 30 to 200 mW with the peak FWHM from 28.70 to 33.06 cm^{-1}. Since the typical effect of laser irradiation on nanoscale samples is heating, this is the result of the effect of heating on the Raman spectra. The usual way to increase the temperature of samples during Raman spectroscopy measurements is to increase the incident irradiation power. Clearly, the Raman line shape becomes increasingly asymmetric as the incident power is increased (Figure 4.12). A shift of the peak position towards lower wavenumbers is also clear. This tendency that the Raman band downshifts and asymmetrically broadens on the low-frequency side with increasing laser illumination can be clearly seen (red lines in the Figure 4.13(a) and (b) and the black line in Figure 4.13(b)). Similar to the behavior of the major Si-Si vibration mode peak FWHM displayed in Figure 4.13(b), the related strained local Si-Si (in the presence of Ge) mode peak FWHM also broadens (from 11.41 to 13.65 cm^{-1}) with the laser power increased from 6 to 40 kW/cm^2. However, the peak position evolution of strained local Si-Si (in the presence of Ge) mode peak is turn out to be the inverse of the main Si-Si vibration mode peak, which rises from 496.82 to 501.38 cm^{-1} when the laser excitation power increases

from 6 to 40 kW/cm^2. Note that at 458 nm excitation, 10^2 W/cm^2 is the minimum excitation intensity allowing the recording of quality Raman spectra (where reasonable fitting is possible) and the application of more than 10^3 W/cm^2 produces irreversible changes in the spectrum, most likely due to laser damage of the studied samples.
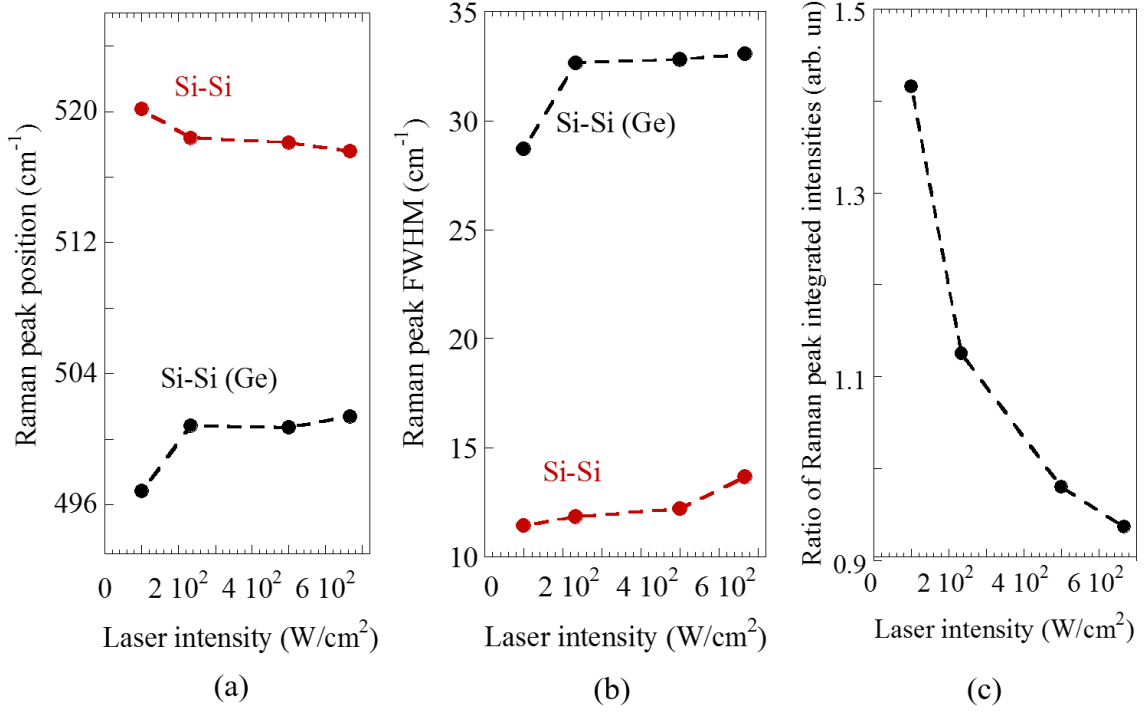
Figure 4.13 Comparison of the Raman signals associated with Si-Si and Si-Si(Ge) vibrations in Si/Ge NW HJs: (a) Raman peak position, (b) Raman peak FWHM, and (c) ratio of Si-Si to Si-Si(Ge) Raman peak integrated intensities as a function of the 458nm excitation intensity.
Source: [32].

Figure 4.14 shows normalized and fitted angular Raman polarization diagrams of the major Si-Si vibrational mode at 520 cm^{-1} for the Si/Ge NW samples under 30mW and 50mW laser powers, as well as the polarization Raman dependence for the Si–Si vibration at 520cm^{-1} measured in (111) single-crystal Si as a reference. Raman spectra are normalized and fitted using sinewave functions for comparison. It is known that the Raman

intensity depends on the orientation of polarization vectors of the incident and scattered light relative to the crystallographic axes of the sample. The observed angular dependencies in the major Si-Si vibration Raman mode of 30mW excitation is nearly identical to that in a (111) Si single crystal at room temperature. However, for the samples under 50 mW laser power we observe quite different behavior in the Raman polarization dependence for the Si–Si vibration at 520 cm^{-1}. The observed lower Raman intensity of samples under 50 mW laser power compared to intensity of samples under 30 mW laser power demonstrates that heat induced strain emerges by increasing the laser power. This significant localization of strain in the Si matrix, because the crystal structure and local environment in Si/Ge NWs significantly deviates from the (111) oriented single crystal Si substrate, is consistent with our previous work and confirms that an additional temperature dependent strain in Si/Ge NW HJs. The explanation and details of the temperature dependent strain during Raman scattering measurements in our samples are given in Local Strain and Stress section. The intensity of Raman scattering at ~ 500 cm^{-1} as a function of the polarization angle and compares the data with similar measurements using (111)-oriented c-Si. It is clearly observed that at the lowest excitation intensity, the Raman signal polarization dependence is the same as for (111) c-Si and Si/Ge NW HJs, which is due to their (111) crystallographic orientation. However, at higher excitation intensity, the Raman scattering polarization dependence in Si/Ge NW HJs becomes considerably weaker.
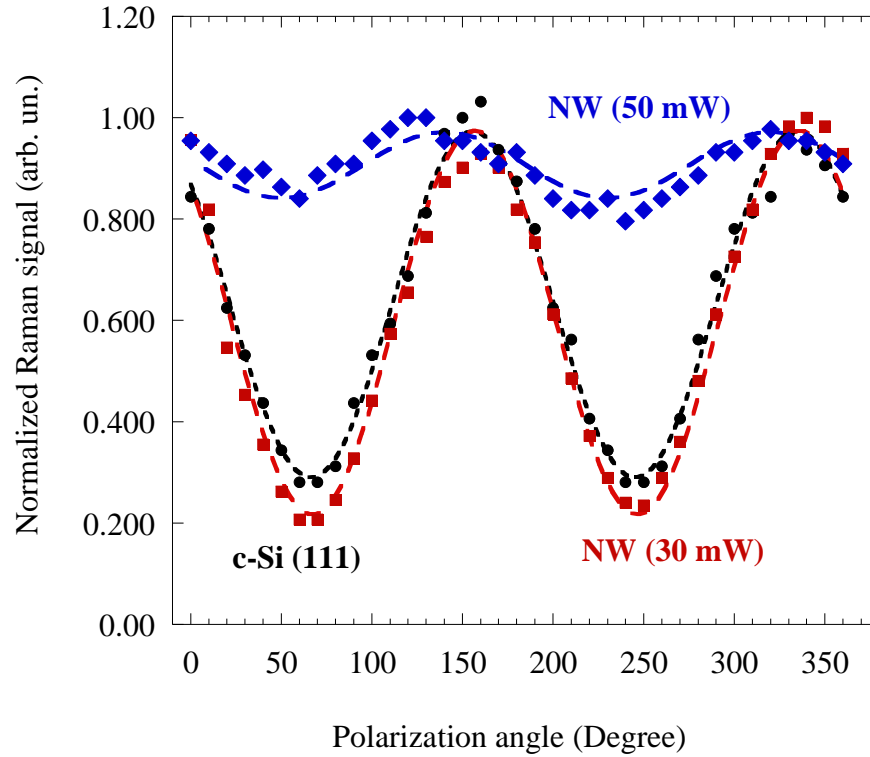
Figure 4.14 Normalized (squares) and fitted (dashed lines) angular polarization dependence of the Raman signal in the range of the major Si–Si vibration mode under 514 nm excitation wavelength with 30mW and 50mW laser powers. The polarization dependence of the Raman signal from a (111) single-crystal Si substrate is shown as a reference.
Source: [32].

The VLS growth mode of Si NWs and Si/Ge NW-based HJs has been intensively investigated [59, 180-182]. It was shown that in lattice-mismatched NW HJs, structural relaxation can be associated with defects in the form of twin boundaries parallel to the growth axis and directly related to the NW kinking [181]. Also, a rough NW surface typically indicates a high density of surface defects, and in many cases the NW diameter continuously decreases producing so-called "tapered" NWs [183]. It was demonstrated that introducing chlorine containing species in the gas phase (e.g., SiH4-HCI-H2 and GeH4 mixed with HCl) greatly inhibits the uncatalyzed material deposition rate, thus yielding

NWs with a smooth surface and uniform diameter along their entire length [184]. These results explain why in our samples the majority of NWs have smooth surfaces and nearly constant diameters (except for the lateral expansion of the Ge segment of the NW HJ).

HR-TEM studies, analyses of lattice fringes, and EDX measurements (Figure 4.1-4.5) indicate that close to the center of the NW in the vicinity of the Si/Ge HJ the lattice mismatch induced strain is partially relaxed via spontaneous intermixing and the formation of an 8nm thick $Si_{1-x}Ge_x$ transition layer. Additional structural relaxation occurs by gradual (within 100nm from the Si/Ge heterointerface) lateral expansion (i.e., increase in diameter) of the Ge segment of the NW (Figure 4.1). Close to the NW surface, we find a distortion in the lattice fringe patterns, which is easily detected by TEM-based FFT analysis (Figure 4.3 inset). These structural imperfections are located within a 2-3nm thick interface layer between the NW core and an oxide layer at the NW surface, and they are slightly extended (up to 5-6nm) toward the NW core in the vicinity of the Si/Ge NW HJs (Figure 4.3). We find that the Si/Ge NW HJs with a diameter approaching 70-100nm can have a nearly perfect crystalline core and overall smaller density of structural defects (due to a smaller surface-to-volume ratio) compared to thinner NWs.

Examination of the spacing between the lattice fringes in different regions of the central portion of the NW (Figure 4.2) shows that 15-20nm away from the Si/Ge heterointerface the lattice constants are similar to those of the respective bulk materials. Starting at the Si-Ge interface, the lattice constant increases from that of Si to that of Ge in parallel with the increase in the Ge concentration, and thus the lattice-mismatch strain expected between Si and Ge is largely relieved during growth by the smooth alloy composition variation in the 8nm thick transition region (Figure 4.5).

4.2.2.1 Strain and chemical composition dependence of the Raman spectrum. First, we estimate x using the Raman peak integrated intensity to start our structural properties analysis. Assuming random mixing in the $Si_{1-x}Ge_x$ alloy, the relative integrated intensities of the Raman modes are expected to vary with the Ge mole fraction (x). In Si/Ge NWs, the relative number of bonds comprising the Si-Si, Si-Ge, and Ge-Ge phonon modes are estimated as $(1-x)^2$, 2x(1-x), and x^2, respectively. The ratio of the integrated peak intensities related to the relative number of bonds of the corresponding phonon modes are as follows:

$$I_{SiSi}/I_{SiGe} = A(1-x)/2x \tag{4.1}$$

and

$$I_{GeGe}/I_{SiGe} = Bx/2(1-x) \tag{4.2}$$

where coefficients A and B are related to the frequencies of the optical modes in the $Si_{1-x}Ge_x$ alloy.

A and B are determined experimentally for each wavelength and vary weakly with alloy composition. For 458nm excitation, A is found experimentally to be 1.85 and B is 3.2 [185]. The intensity method for determining the value of x is independent of strain in the alloy layer and depends on the integrated intensity of the phonon bands. Thus, proper base line correction is required to estimate the intensity with accuracy in Raman spectra. The Ge content (x) are calculated as 0.37 ± 0.1 and 0.51 ± 0.1 using Eqs. (4.1) and (4.2) with the values of A and B indicated. We have found the intensity ratios calculated from Raman data to be in good agreement with EDX data indicating preferential alloy compositions of

lower x close to the Si NW part than x close to the Ge NW part. And we discovered in our previous work (photoluminescence measures) that preferential alloy compositions of x≈0.15–0.2 close to the Si part of the Si/Ge NW and x≈0.5 close to the Ge part of the Si/Ge NW [55]. Because the Ge–Ge peak for a $Si_{1-x}Ge_x$ alloy is quite weak, in particular for small x≤0.2, in which we can neglect the intensity of Ge–Ge peak [55]. This calculated results meets our expectation that x≈0.5 near the Ge part while x ≈ 0.35 (the average of 0.2 and 0.5) with a non-neglected Ge–Ge peak intensity in x=0.5 and neglected Ge-Ge peak intensity in x=0.2 as well as a non-neglected Si-Si peaks intensity averaged both in x=0.2 and 0.5.

Then, we analyze Ge content in a different method: the peak position in wavenumbers, by which strain can also be calculated. The Raman spectrum of a strained $Si_{1-x}Ge_x$ HJ alloy consists of three distinct peaks whose energies and therefore the peak positions depend on the Ge content x and the strain ε. These three first-order Raman lines shown in Figure 4.11 in Raman spectra are due to the atomic vibrations of Si–Si(Ge) (at ~500 cm^{-1}), Si–Ge (at ~410 cm^{-1}) and Ge–Ge (Si) (at ~290 cm^{-1}) bonds in the $Si_{1-x}Ge_x$ alloy. We curve fitted the major phonon bands mostly using a Gaussian profile to estimate the peak positions accurately.

The shift of the Si band relative to the strain-free position is given by [186]

$$\Delta\omega_{Si-Si} = \omega_{strain} - \omega_{Si} = \left(\frac{1}{\omega_o}\right)\left\{\frac{pS_{12}}{(S_{11}+S_{12})} + q\right\}\varepsilon = b\varepsilon \tag{4.3}$$

where S_{11} and S_{12} are elastic compliance constants, p and q are phenomenological parameters, and ε is the in-plane strain. Here, b is the strain-shift coefficient, ω_{Si} and

ω_{strain} are the frequencies of the Si modes in the strain-free and strained Si layers, respectively.

For the strained $Si_{1-x}Ge_x$, Eq. (4.3) can then be rewritten as in the literature describing the peak position of $Si_{1-x}Ge_x$ layer under strain.

$$\omega_{Si-Si} = \omega_{Si} - ax - b\varepsilon \qquad (4.4)$$

Where the coefficient a is the so-called composition-shift coefficient, then an important parameter to evaluate individual shifts due to Ge composition and strain in a $Si_{1-x}Ge_x$ alloy. We adopted $\omega_{Si} = 520$, a=70.5 and b=830 as reported experimentally. With the same dependence of the Si–Si, Si-Ge and Ge-Ge band frequency on the Ge composition and strain in the $Si_{1-x}Ge_x$ alloys are also examined. The wavenumbers of the three different phonon modes are

$$\omega_{Si-Si} = 520.7 - 70.5x - 830\varepsilon \qquad (4.5)$$

$$\omega_{Si-Ge} = 400.5 + 16x - 575\varepsilon \qquad (4.6)$$

$$\omega_{Ge-Ge} = 282.5 + 16x - 384\varepsilon \qquad (4.7)$$

The linear dependence in Si part of the $Si_{1-x}Ge_x$ from Eqs. (4.5) and (4.6), strained Ge composition is given by

$$x = \frac{(\omega_{Si-Ge} - 400.5) - 0.6928(\omega_{Si-Si} - 520)}{64.84}, \qquad (4.8)$$

and strain ε calculation by the following expression

$$\varepsilon = \frac{0.23(520-\omega_{Si-Si})-(\omega_{Si-Ge}-400.5)}{766.9},$$ (4.9)

From Eqs. (4.5) and (4.6), we obtain the following expressions for Ge part x and ε

calculations:

$$x = \frac{1.497(\omega_{Ge-Ge}-282.5)-(\omega_{Si-Ge}-400.5)}{7.96},$$ (4.10)

$$\varepsilon = \frac{(\omega_{Ge-Ge}-282.5)-(\omega_{Si-Ge}-400.5)}{191},$$ (4.11)

Table 4.1 Estimated Values of Ge Content and Strain for Alloys using Raman Scattering Data Collected under 458nm Excitation

		Equation (4.1)	Equation (4.8)	Equation (4.2)	Equation (4.10)	Equation (4.9)	Equation (4.11)
Ge content, x	Si part	0.37	0.37±0.01	-	-	-	−
	Ge part	-	-	0.51	0.5±0.01	-	−
Compressive strain ε (%)	Si part	-	-	-	-	0.81±0.02	-
	Ge part	-	-	-	-	-	2.4729

From the Raman analysis, taking into account the local strain fluctuations in the NW HJs, the strain was precisely calculated. The calculated values of x and ε using the Raman data are summarized in Table 4.1. We find a reasonably good correlation of Ge content value between Raman shifts and intensities data.

4.2.2.2 Temperature dependence of the Raman spectrum. The laser beam by itself could be a significant source of thermal power delivered to the NWs. In addition to Stokes/anti-Stokes Raman peak ratio, Raman peak position and FWHM are also sensitive to the sample temperature. As the temperature increase, the pure-Si phonon band gradually shifts toward low frequencies and broadens. This temperature behavior of the phonon spectrum is typical of single-crystalline silicon and, as a rule, is associated with the anharmonic phonon-phonon interaction and the thermal expansion of the crystal as the

temperature grows. The temperature dependence of the frequency shift of the Si optical band at the Brillouin zone center is described, in the general case, by the relation [187]:

At constant pressure:

$$\Delta\omega = [\frac{d\omega}{dT}]_V \Delta T + [\frac{d\omega}{dV}]_T [\frac{dV}{dT}]_P \Delta T = \Delta\omega_1(T) + \Delta\omega_2(T) \tag{4.12}$$

$$\Delta\omega_1(T) = A(1 + \frac{2}{e^x - 1}) + B\left(1 + \frac{3}{e^y - 1} + \frac{3}{(e^y - 1)^2}\right) \tag{4.13}$$

where $x = h\omega_0/2kT$, $y = h\omega_0/3kT$, and A= -3.44 cm^{-1} and B= -0.0015 cm^{-1} are anharmonicity constants.

$$\Delta\omega_2(T) = \omega_0(\exp\left(-3\gamma \int_0^T \alpha(T)dT\right) - 1) \tag{4.14}$$

where ω_0 is the frequency of the phonon band location at T=0K, γ is the Grüneisen parameter and $\alpha(T)$ is the temperature dependence of CTE. The first term in Eq. (4.13) corresponds to the phonon band shift under the action of a phonon vibration anharmonicity at elevated temperatures. The second term, in Eq. (4.14) describes the thermal expansion effect.

Based on Eq. (4.12), the linear dependence of a local temperature in Si, Si$_{1-x}$Ge$_x$ on the power density of the exciting laser radiation is demonstrated and reported earlier [188] based on both experimental and theoretical data. With increasing temperature, the Raman peaks are shifted to lower wavenumbers and broadened. The linear dependence for Raman

peak position $\Delta\omega_{Si-Si}$ and Raman spectrum FWHM $\Delta\Gamma_{Si-Si}$ as a function of temperature in the major Si-Si vibration mode can be simplified as

$$\Delta\omega_{Si}(T)/cm^{-1} = \text{-}0.025(\Delta T/K), \tag{4.15}$$

and

$$\Delta\Gamma_{Si}(T)/cm^{-1} = \text{-}0.011(\Delta T/K), \tag{4.16}$$

We estimate the local temperature of the pure Si part in the Si/Ge NWs from the experimentally measured peak position shifts of the major Si-Si vibration mode Raman line in accordance with Eq. (4.12). The temperatures we estimated here are 403.64K for 200mW excitation laser power, 370.14K for 70mW and 300K for 30mW.

However, we expected the temperature growth is accompanied by the thermally induced strain resulting from the difference between the temperature dependences of CsTE for Si and Ge. The additional temperature-dependent elastic strains mapped shift $\Delta\omega_3(T)$ is a rather complicated problem which is absent from Eq. (4.12). Before we estimate temperature-dependent elastic strains, we need to know the local temperature of strained Si-Si Raman mode.

4.2.2.3 Thermal Transport and Local Temperature Gradient. In our measurements, we use an intense and focused laser beam with a short penetration depth and create a hot spot close to the sample surface. Heat can dissipate vertically and laterally. Due to the much larger Si substrate thermal conductivity compared to Ge and $Si_{1-x}Ge_x$, it is reasonable to assume that in our sample heat dissipation is mostly controlled by a vertical heat flow. As we have the pure Si part temperature, the temperature gradient observed between different

parts of the sample can be evaluated via the thermal conductivity (κ). According to the Fourier law of heat conduction, the temperature gradient can be calculated using

$$\Delta T = \frac{P \times L}{\kappa \times A}, \tag{4.17}$$

where P is the laser power absorbed by a sample with a thickness (L) in the direction normal to a surface of a cross sectional area (A) due to a temperature gradient (ΔT). In our measurements, we use an intense and focused laser beam with a short penetration depth and create a hot spot close to the sample surface. In the case of a $Si_{1-x}Ge_x$ (0.2<x<0.85) alloy, the thermal conductivity is depend on Ge content x as following

$$\kappa = 0.046 + 0.084x \ (Wcm^{-1}K^{-1}), \tag{4.18}$$

At room temperature, the thermal conductivity of the strained $Si_{1-x}Ge_x$ near Si part is $0.0628 Wcm^{-1}K^{-1}$, the thermal conductivity of the strained $Si_{1-x}Ge_x$ near Ge part is 0.088 $Wcm^{-1}K^{-1}$. The Si thermal conductivity is $1.3 \ Wcm^{-1}K^{-1}$, the Ge thermal conductivity is $0.58 \ Wcm^{-1}K^{-1}$, which are both order of magnitude larger than that of the strained $Si_{1-x}Ge_x$. The length of nanowire sample is 1500-2000nm (assume Si length and Ge length are 800nm for the following estimation), the entire thickness of the strained $Si_{1-x}Ge_x$ is 8nm (5nm in Si part, 3nm in Ge part in Figure 4.5).

For our specific excitation laser power, temperature over per unit length is

$$\frac{\Delta T}{L} = \frac{P}{\kappa \times A} \tag{4.19}$$

$$In\ Ge\ part,\ \left(\frac{\Delta T}{800nm}\right)_{Ge} : \left(\frac{\Delta T}{4nm}\right)_{SiGe} \approx 1:9 \tag{4.20}$$

$$In\ Si\ part,\ \left(\frac{\Delta T}{800nm}\right)_{Si} : \left(\frac{\Delta T}{4nm}\right)_{SiGe} \approx 1:15 \tag{4.21}$$

Thus, the temperature gradient $\frac{dT}{dL}$ established between the peak 1 (Figure 4.12) temperature at the $Si_{1-x}Ge_x$ alloy layer in the main Si mode and the peak 2 temperature of the $Si_{1-x}Ge_x$ alloy layer in the strained Si mode is in the order of 10 K and decays with increasing temperature from room temperature (proportional to T^α and α~ -1 to -2), and this temperature gradient is dominant representing the NWs for the heating effect and heat-induced bending effect while temperature gradient over long and pure Si or Ge can be neglected compared to that of the strained Si and main Si phonon modes. We use calculated local temperatures for our estimations for accuracy.

On considering the Raman measurements, we anticipate that under the applied laser excitation intensity of 10^2-10^3 W/cm^2 the sample temperature increases, and such temperature increase can be detected by monitoring the Raman peak wavenumber and FWHM temperature dependencies [190, 191]. Generally, as temperature increases the Raman peak shifts toward lower wavenumber due to thermal expansion and changes in the self-energy of the vibrational mode [189]. At the same time, the Raman peak FWHM increases, mainly due to energy relaxation processes (i.e., the decay of the Raman phonon into various optical/acoustical phonons, etc.) [190]. Thus, by knowing the initial (room temperature) Raman peak wavenumber/FWHM and their temperature dependencies [190,

191], one can accurately calculate the sample temperature by measuring the shift and broadening of the Raman spectra.

Compared to the experimental data reported by Hart and Aggarwal, our estimated temperatures according to Raman peak shifts are depicted in peak position and peak FWHM respectively (in Figure 4.15). Figure 4.15(a) confirms the estimated temperatures from frequency shift of the major Si-Si vibration Stokes Raman line set up consistency of the former reported experimental data. At these temperatures, the major Si-Si vibration Stokes Raman peak FWHM of our samples are found broadened, but after implement of a simple linear regression we find the two linear extrapolations are parallel with 7 cm^{-1} upshifts (Figure 4.15(b)). With increasing laser illumination, the temperature dependent local Si-Si (in the presence of Ge) peak upshifts while temperature dependent major Si-Si vibration mode peak downshifts. This downshifting can be due to a laser heating effect of the nanowires where the lattice constant increases as the temperature of the sample increases and the bonds between atoms become weaken. The asymmetric line shape is due to a Fano interference between the k=0 optic phonon scattering and electronic continuum scattering from laser-induced electrons in the conduction band [191]. The unusual upshifting of local Si-Si (in the presence of Ge) mode Raman line observed here is produced by a change in Si/Ge NW strain due to the large difference in Si and Ge CsTE. This mismatch in Si and Ge CsTE creates an additional, temperature dependent strain in Si/Ge NW HJs. The explanation and details of the temperature dependent strain during Raman scattering measurements in our samples are given in discussion part.
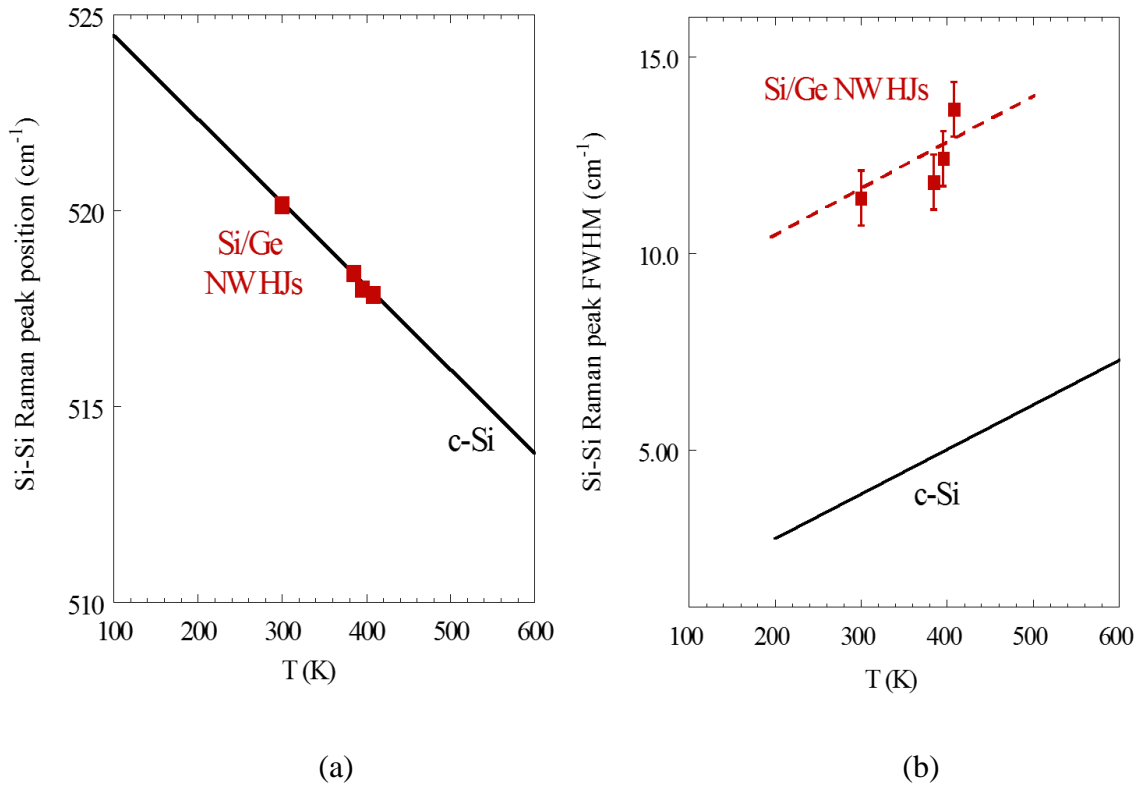
Figure 4.15 (a) Frequency shift of the major Si-Si vibration Stokes Raman line versus temperature. (b) Plot of the FWHM for the Stokes component of the major Si-Si vibration Stokes Raman line in silicon as a function of temperature. The red squares represent our estimated Raman points. The black circles represent the Raman frequency shift as calculated based on the theory. The dashed line is a smooth curve drawn through the points with linear regression (deviation).
Source: [32].

Figure 4.15 compares the Si-Si Raman peak position and FWHM in Si/Ge NW HJs with the theoretically predicted and experimentally confirmed temperature dependencies of that in bulk c-Si [190, 191]. The Si-Si Raman peak position in Si/Ge NW HJs is in full agreement with the bulk c-Si Raman temperature dependence calculated by using Ref. 190 (Figure 4.15 (a)), and under 700 W/cm^2 excitation the sample temperature is estimated to be ~ 410K. This significant laser heating of our samples is due to a reduced thermal conductivity of the Si/Ge NW HJs compared to that in c-Si.

The Si-Si Raman peak FWHM temperature dependence in Si/Ge NW HJs follows that in bulk c-Si [191] but with an almost four times greater value (Figure 4.15(b)). The initial broadening of the Si-Si Raman peak in Si/Ge NW HJs can be attributed to a non-uniform strain, which is also expected to reduce the sample thermal conductivity. Also, the reduced ratio of Si-Si to Si-Si (Ge) Raman peak intensities under higher laser intensity (Figure 4.13(c)) is consistent with the assumption that at higher temperature light absorption in Si/Ge NW HJs increases and a smaller number of photons reach the c-Si substrate.

4.2.2.4 Local Strain and Stress. Peak 1 and Peak 2 have opposite Raman shift behaviors even though they have the same delta temperature. A relative compressive strain of Peak 1 is observed in Figure 4.13(a). This relative compressive strain is introduced by the mismatch of thermal expansion. Strain due to the 4.2% difference in the lattice constant between Ge and Si should be absent beyond the initial stage of the laser power rise [193]. However, the increase from the room temperature to the temperature increment causes a strain due to the difference in CsTE between Ge and Si. The strained Si-Si (Ge) mode peaks red-shift to the left side of the Si bulk peak. The red-shift of Si-Si (Ge) mode indicates it has longer wavelengths compared with the Si bulk Si-Si mode.

Thermal mismatch strain is given as [192]:

$$\varepsilon_{th} = \int_{T_0}^{T_1}[\alpha_{Si1-xGex}(T) - \alpha_{Si}(T)]\, dT, \tag{4.22}$$

where $\alpha_{Si1-xGex}(T)$ and $\alpha_{Si}(T)$ are the CsTE of $Si_{1-x}Ge_x$ and Si respectively.

$$\alpha_{Si}(T) = 3.725 \times 10^{-6}\left[1 - e^{5.88 \times 10^{-3}}(T + 149015)\right] + 5.548 \times 10^{-10}T, \tag{4.23}$$

$$\alpha_{Ge}(T) = 6.050 \times 10^{-6} + 3.60 \times 10^{-9}T - 0.35 \times 10^{-12}T^2, \tag{4.24}$$

For $Si_{1-x}Ge_x$, the coefficient can be linearly interpolated between the values for Si and Ge given in Eq. (4.23) and (4.24), where T is in Celsius. T_0 and T_1 are the starting and ending temperature for the heating process step. At room temperature, the CsTE of Si and Ge are 2.7×10^{-6} K^{-1} and 5.9×10^{-6} K^{-1}, respectively. $Si_{1-x}Ge_x$ CTE is determined by $(2.6+2.55x) \times 10^{-6}$ K^{-1} (x<0.85). Strain from heating is due to the volume change that occurs when materials have different expansion rates. Because $Si_{1-x}Ge_x$ has a larger expansion coefficient, the increase of the lattice constant of the Ge inside Si during heating is suppressed by the Si, resulting in a permanent compressive strain of around 0.01-0.02% in Si-Si(Ge) vibration mode depending on the temperature difference. The thermoelastic stress is given by

$$\sigma_{th} = Y \times \varepsilon_{th}, \tag{4.25}$$

where Y is Young's modulus. Young's modulus decreases as the temperature increases.

Similar to estimate strain, the magnitudes of local stress are estimated in Raman shifts by a general expression. The relation between the measured Raman shift and uniaxial stress is then obtained to be

$$\Delta\omega_{Si-Si}(\sigma) = \left(\frac{\sigma}{\omega_o}\right)\{pS_{12} + q(S_{11} + S_{12})\}, \tag{4.26}$$

where ω_o is the LO-TO phonon band frequency in unstressed Si-Si bond, the elastic constants are $S_{11} = 7.68{\times}10^{-12}Pa^{-1}$ and $S_{12} = -2.14{\times}10^{-12}Pa^{-1}$, and the phonon deformation potentials are $p = -1.43\omega_0^2$ and $q = -1.89\omega_0^2$ [193]. Because the frequency stress-free Si–Si phonon band is only sensitive to the temperature and Ge content x, ω_o should be corrected by Eq. (4.4) and (4.15), turning out to be

$$\omega_o = 520.7 - 70.5x + \Delta\omega_{Si}(T), \qquad\qquad (4.27)$$

According to Eqs. (4.3) and (4.26), the magnitudes of the compressive elastic strain and stress that result in the high-frequency shift of the Si-Si(Ge) phonon band are calculated and organized in Table 4.2.

Table 4.2 Estimated Values of Local Strain and Stress at Different Temperatures using Various Methods

		6	14	40
Laser Power (kW/cm²)		6	14	40
Peak 2 Temperature (K)		300	370.14	403.64
Peak 1 Temperature (K) From Eq.(4.17)		300	388.14	420.64
Local Strain ε (%)	**Peak 1**	0.73	1.01	1.26
		From Eq.(4.9)	From Eq.(4.3)	From Eq.(4.3)
Local Stress σ(GPa)	**Peak 1 From Eq.(4.26)**	1.47	2.17	2.74
	Peak 1 From Eq.(4.25)	1.32	1.82	2.27
Thermoelastic Strain ε_{th}(%)	**From Eq.(4.3)**		0.28	0.25
	From Eq.(4.22)		0.02	0.01
Thermoelastic Stress σ_{th}(GPa)	**Peak 1 From Eq.(4.25)**		0.5	0.45

Due to the calculated local stress is in the order of 1GPa, the Si-Si vibration mode peaks have large pressure shifts to higher energy with increasing local pressure. The calibration is represented by the quadratic least-squares fit. The equation of this fit is [194]:

$$\omega_{Si-Si}(P) = 519.5 \pm 0.8 + (0.52 \pm 0.03)P + (-0.0007 \pm 0.0002)P^2 \qquad (4.28)$$

where P is the pressure in kbar. We are able to accurately calibrate $\Delta\omega_{Si-Si}(P)$ using 14.7kbar, 2.17kbar and 2.74kbar under three different power excitations. After comparing with Raman raw data from experiments, we conclude the estimation of stress in Table 4.2 is reasonable.

The estimated strain arises from lattice parameter mismatch is the more significant than the difference in CsTE between Si and Ge. Because the lattice constants of Si (a_{Si}) and Ge (a_{Ge}) at room temperature are 5.431Å and 5.658Å, respectively. The $Si_{1-x}Ge_x$ lattice parameters [195] deviate slight from Vegard's law $a(x) = a_{Si} + x(a_{Ge} - a_{Si})$, which expressed as:

$$a(x) = (5.431 + 0.20x + 0.027x^2) \text{ Å}, \qquad (4.29)$$

Lattice mismatch between Si and $Si_{1-x}Ge_x$ is approximately 0.7564×10^{-2}, which is consistent with our calculated data from Eq. (4.9). Thus, temperature dependent thermal strains in our sample should be about one order of magnitude less than lattice mismatch strains. However, in our estimation in Table 4.2, thermoelastic strain is several times larger than the estimation from CsTE. It is found that the thickness smaller than about 20nm increase dramatically with decreasing size, and is significantly higher than that of bulk silicon [196]. The thickness of $Si_{1-x}Ge_x$ in our NWs is very small about 5nm. Thus, CTE of $Si_{1-x}Ge_x$ may be implanted by a higher number than we estimate using Eq. (4.22) in Table 4.2. Another possibility is due to even larger Ge CTE than $Si_{1-x}Ge_x$ CTE, stress on

Ge part is not only horizontal but also vertical. This vertical stress will pass down to $Si_{1-x}Ge_x$ part and bend it. Stress on $Si_{1-x}Ge_x$ is no longer evenly distributed over the entire cross-section. The non-uniformly distributed stress means that is more than a few times in the center than both ends.

With the previous estimated data, we split strained Si-Si peak and main Si-Si peak from the 40 kW/cm^2 laser intensity Raman spectrum shown in Figure 4.16(a) red curves. Then we remove shifts induced by strain of thermal expansion, the accumulated Raman line shape of strained Si-Si peak and main Si-Si peak in Si/Ge NWs is estimated shown in Figure 4.16(b) red curves. The Raman line without thermal strain is supposed to shift to left compared with the experimental date we get. We conclude that with increasing temperature, the local Si-Si (in the presence of Ge) peak abnormal upshifts is produced by a change in Si/Ge NW strain due to the large difference in Si and Ge CsTE. This mismatch in Si and Ge CsTE creates an additional, temperature dependent strain in Si/Ge NW HJs.
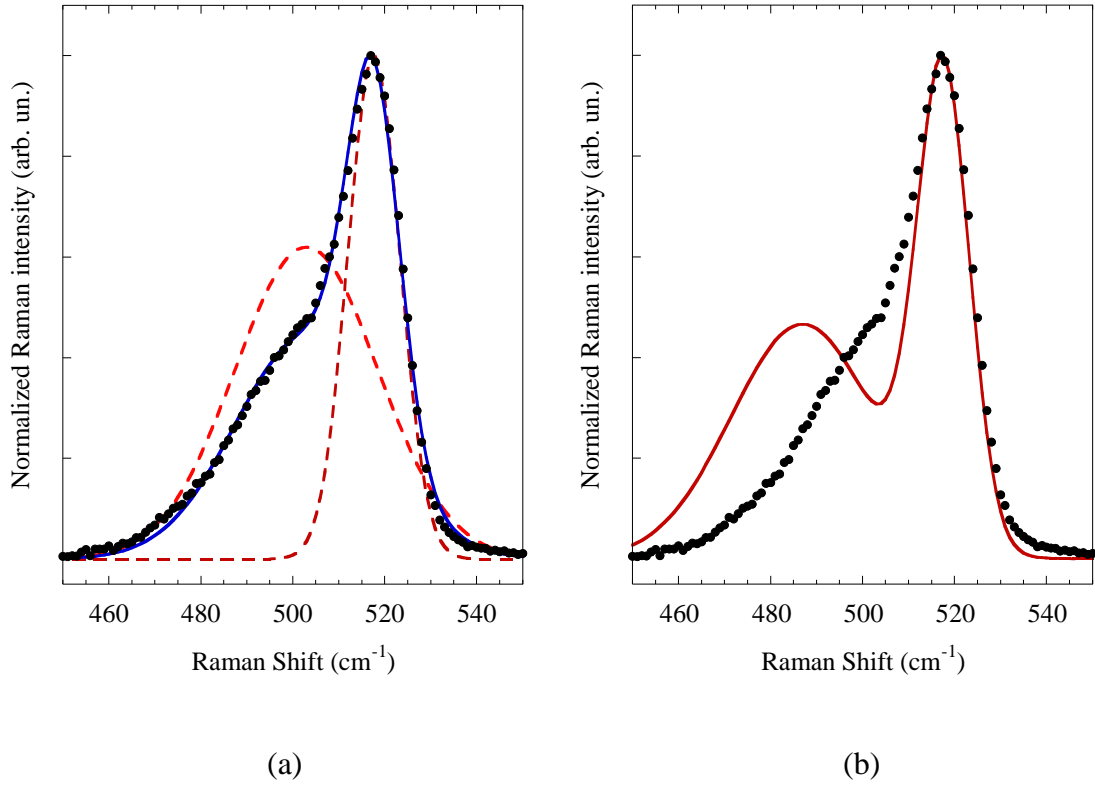
Figure 4.16 (a) The Raman spectra of curve fitted strained Si-Si peak and main Si-Si peak (dashed red lines) in Si/Ge NWs from experiments, (b) The accumulated Raman spectra of main Si-Si peak combined with strained Si-Si peak in Si/Ge NWs from estimations when strain of thermal expansion is removed, at laser intensity 40 kW/cm^2 using 458 nm radiation compared with the raw Raman line shape (black dots). The blue line is the accumulated Raman spectrum.
Source: [32].

While the Si-Si Raman peak shift toward lower wavenumbers in Si/Ge NW HJs under increasing laser excitation is explained by the sample temperature increase due to absorption of the intense laser radiation, the Si-Si(Ge) Raman peak under the same conditions shifts in the opposite direction (Figure 4.13a). Figure 4.16(a) compares the experimental Raman spectrum with the Raman spectrum simulated under the assumption that both Si-Si and Si-Si(Ge) Raman peaks due to the temperature increase should shift toward lower wavenumbers. The discrepancy in the simulated (Figure 4.16(a)) and

113

experimentally (Figure 4.16(b)) observed positions of the Si-Si(Ge) Raman peak is $\sim 15 \text{ cm}^{-1}$, and it can be associated with a considerable laser heating induced thermal stress of the order of 2-3 GPa [197, 198]. Stress is known to affect the Raman polarization dependence in Si/SiGe nanostructures [45], and this notion explains the experimental data shown in Figure 8. Also, assuming that the PL1 feature is attributed to band-to-band radiative carrier recombination in the Si segment close to the Si/Ge NW HJ, the estimated value of stress (2-3 GPa) is consistent with the compressive stress required to shift the PL1 peak toward higher photon energy by ~ 60 meV. Note that at room temperature the PL measurements were performed using an excitation intensity approaching 600 W/cm^2.

Under 600-700 W/cm^2 intensity of laser excitation, the sample temperature increase of $\Delta T \approx 110$ K is quite large. Most of the 458 nm laser radiation is absorbed by the top (Ge) segment of the Si/Ge NW HJs, and heat flow is directed toward the c-Si substrate, which can be considered as a heat sink. The Si and Ge segments of the Si/Ge NW HJs are at least 500 nm long and the $Si_{1-x}Ge_x$ interface alloy layer is only 8 nm thick, but the difference in their thermal conductivity could be more than 50 times; thus, all segments of the NW (Ge, Si and $Si_{1-x}Ge_x$) contribute to the overall thermal conductivity and the observed temperature increase. Using bulk c-Si, c-Ge and $Si_{1-x}Ge_x$ alloy parameters (e.g., CTE, Young's modulus, etc.), the estimated thermal stress at the Si/Ge heterointerface, due to the mismatch in Si and Ge CTEs, is ~ 0.5 GPa. The discrepancy thus found compared with the number determined above (2-3 GPa) can be explained by assuming that laser induced heating also slightly bends NWs, possibly due to a non-uniform heat flow, and it creates additional stress in the vicinity of the Si/Ge HJ where the large mismatch in thermal expansion takes place.

4.2.2.5 Temperature Dependence of Absorption Coefficient and Bandgaps. When light is absorbed in passing through a medium from the point r_1 to another point r_2, the absorption coefficient α of the medium is defined by [199]:

$$I(r_2) = I(r_1)exp(-\alpha|r_2 - r_1|), \tag{4.30}$$

where $I(r)$ denotes the intensity at r. From Figure 4.17, the relative intensity of Si-Si peak related to Si-Si(Ge) peak is decreased with increased temperature. The calculated absorption coefficient of Si/Ge NWs in Si part as function of temperature $\alpha(T)$ is depicted by Figure 4.17.
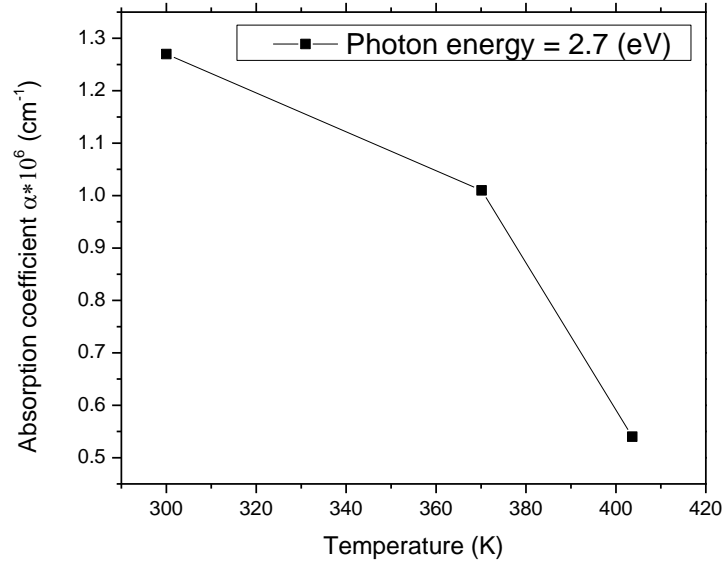
Figure 4.17 The absorption coefficient of Si/Ge NWs in Si part vs. different temperatures at 2.7eV photon energy

The theoretical value of α in Si$_{1-x}$Ge$_x$ (x=0.35) alloy is about $1.3\times10^6\ cm^{-1}$ [200], which is consistent with our estimated data $\alpha = 1.27\times10^6\ cm^{-1}$. It is clearly seen that α

of the Si/Ge NWs in Si part decreases with increased temperature. This suggests α increases starting at a lower energy position than that in room temperature, indicating a shift of absorption edge toward lower energy, i.e., shrinkage of the bandgap.

With increasing temperature at constant pressure, the energy bands (E_g) of semiconductors, and therefore the various absorption edges and interband critical points, exhibit large shifts reported early [201]. These shifts are originated from two sources. The first is due to the thermal expansion of the lattice coupled with the change of the electron energies with volume. The second contribution is the direct renormalization of band energies by electron-phonon interactions. The total shift can be expressed in the following derivatives:

$$[\frac{\partial E_g}{\partial T}]_P = [\frac{\partial E_g}{\partial T}]_V + [\frac{\partial E_g}{\partial T}]_{therm\,exp}, \tag{4.31}$$

with

$$[\frac{\partial E_g}{\partial T}]_{therm\,exp} = [\frac{\partial lnV}{\partial T}]_P [\frac{\partial p}{\partial lnV}]_T [\frac{\partial E_g}{\partial p}]_T = -3\alpha B [\frac{\partial E_g}{\partial p}]_T, \tag{4.32}$$

where $\alpha = L^{-1}(\partial L/\partial T)_P$ is the CTE and $B = -V(\partial p/\partial V)_T$ is the bulk modulus. The effect of temperature dependence of energy bandgap is quantified by the linear expansion coefficient of a material with the fact that α is strongly dependent on T.

For simple estimation, the application of the Varshni's relation fit to the temperature dependence of semiconductor bandgaps is justified on both practical and theoretical grounds [202] as a function of the temperature T:

$$E_g(T) = E_g(0) - \frac{\alpha T^2}{T+\beta}, \tag{4.33}$$

where $E_g(0)$, α and β are the fitting parameters. For pure Silicon, the bandgap at 0K is $E_g(0) = 1.16948eV$ with $\alpha = 4.73 \times 10^{-4}eV/K$ and $\beta = 636K$. For pure Ge, the bandgap at 0K is $E_g(0) = 0.742eV$ with $\alpha = 4.8 \times 10^{-4}eV/K$ and $\beta = 235K$. For $Si_{1-x}Ge_x$, the bandgap is derived as [203]:

$$E_g^{SiGe} = E_g^{Si}(1-x) + E_g^{Ge}x + C_g(1-x)x, \tag{4.34}$$

with the temperature dependent bandgaps of the constituents E_g^{Si} and E_g^{Ge} as well as the bowing factor $C_g = -0.4eV$.

The energy bandgap of semiconductors tends to decrease as the temperature is increased, estimated in Table 4.3. This behavior can be better understood because the interatomic spacing increases with the intensification of the amplitude of the atomic vibrations due to the heating. The potential built by the electrons is reduced by this interatomic spacing, making the effect further to shrink the energy bandgap. From previous reported experimental data, the bandgap of $Si_{1-x}Ge_x$ (x=0.5) at room temperature is 0.917 which is larger than our calculated one 0.7925. The reason is due to the special case of the technologically strained $Si_{1-x}Ge_x$ grown on Si using one-valley bandgap fit. The tensile stress, also causes a decrease of the bandgap. This indicate that the strain-induced bandgap varies reversibly with strain and changes the number of free carries at Fermi energy, which strongly interact with phonon modes.

Table 4.3 Estimated Values of Bandgaps at Different Temperatures using the Varshni's Relation

Temperature (T)	Bandgaps (eV)			
	Si	Ge	$Si_{1-x}Ge_x$ (x=0.5)	$Si_{1-x}Ge_x$ (x=0.2)
300	1.124	0.661	0.7925	0.9674
370.14	1.105	0.633	0.7840	0.9466
403.64	1.095	0.620	0.7575	0.9360

4.2.2.6 Thermal Buckling and Bending of Heated Si/Ge NW HJs. In order to investigate the suitability of the prediction by fitting experimental measurements with numerical estimations, analytical approaches have been proposed to incorporate the elastic behavior of bending NWs. The expression of critical thermal buckling temperature (CTBT) is dependent on effective elastic modulus under bending and axial deformation of NWs [204]:

$$\theta_{cr} = \frac{n^2\pi^2 I}{\alpha l^2 A} \frac{E_{Bending}}{E_{Axial}} \tag{4.35}$$

where $E_{Bending}$ and E_{Axial} are Young's moduli under bending and axial deformation, and α is the effective CTE of NWs, respectively; I and A are the inertia moment and the cross-

section area of NWs; l the length of NWs; n is a positive integer. The smallest eigen value in this case corresponds to n = 1, that is, the first buckling model [205].

For a rough estimation, the local surface elasticity is treated as nonlocal theory. The influence of the size-dependent CTE of NWs on their thermal buckling behaviors has neglected yet. Thus, the CTBT is

$$\theta_{cr} = \frac{n^2\pi^2 I}{\alpha l^2 A} \tag{4.36}$$

After inserting the moment of inertia of a rod with constant cross-section, the CTBT becomes

$$\theta_{cr} = \frac{d^2\pi^2}{4\alpha l^2} \tag{4.37}$$

where d is the diameter of NWs.

For uniform temperature change$\Delta T \leq \theta_{cr}$, indicating the maximum allowed wire length corresponding to ΔT is determined by

$$l_{max} = \sqrt{(\frac{d^2\pi^2}{4\alpha\Delta T})} \tag{4.38}$$

The CTE is highly sensitive to temperature as well as composition, $l_{max} \sim$ 5-6 um. Based on static mechanics, we deduce the following two equations from Three-Point Bending Model:

$$F_{Si\text{-}part} + F_{Ge\text{-}part} = F \tag{4.39}$$

$$\sum M = -F * \frac{L}{2} + F_{si\text{-}part} * L = 0 \tag{4.40}$$

where F is the force. M is the moment.

For a circular cross section, the flexural stress is [206]

$$\sigma = \frac{FL}{\pi R^3} \tag{4.41}$$

Combining the polar moment of inertia:

$$I = \frac{\pi R^4}{2} \tag{4.42}$$

The bending calculation made from the different material parameters of Si and Ge is listed in Table 4.4:

Table 4.4 Estimated Bending Parameters of Si and Ge Part in Si/Ge NW HJs

Methods	Force	Deflection	Stiffness	Strain
Si part	1.1×10^{-6} N	$1.3 nm$	$846\ N/m$	0.16%
Ge part	1.3×10^{-6} N	$1.9 nm$	$684\ N/m$	0.26%

4.3   Electrical Properties of Si/Ge NW HJs

Studies of electrical properties of axial Si/Ge NW HJs are critically important for understanding of carrier transport in 2D device prototypes, however they are less common. The main reason is that such electrical measurements are complicated by formation of reliable contacts to NWs. Traditional techniques involving NW removal from substrates and placing them between pre-fabricated electrical leads were applied to elemental NWs. However, for axial NW HJs this technique is less effective because during the removal from substrates the NWs often break at the vicinity the HJ, especially in the case of lattice mismatching materials like Si and Ge. Alternative techniques are either very complex (e.g., growth of bridging NWs between micro-machined vertical walls, use of micro-probes inside an electron microscope chamber for in-situ measurements), or not reliable (e.g., use of liquid conductors with possible leak between NWs).

In this section, we present studies of electrical properties of axial Ge-Si NW HJs obtained using a simple, highly reproducible and minimally distractive formation of electrical contacts. Performing these measurements, we find that Ge-Si axial NW HJs under applied dc forward bias exhibit current instabilities and well-defined damped oscillations with frequency of 10-30 MHz. The results are explained assuming that electron transitions from Ge to Si NW segments require momentum scattering; this process disrupts flow of charge carriers and creates current oscillations with frequencies limited by various electrical components (series resistance, parasitic capacitance, HJ inductance, etc.).

By Applying effective forward bias (i.e., "+" on a p-type Si substrate), we measure current throughout only highly conducting (presumably, higher quality axial Ge-Si NW HJs with a good electrical contact), while lower electrical conductivity (presumably

defective or higher series resistance NWs) do not contribute to the measured electric current. At the same time, under 'reverse' bias we mostly measure current leaking throughout defective Ge-Si NW HJs. Thus, we discuss only measurements performed under 'forward bias'.

4.3.1 Results

Figure 4.18(a) shows current density-voltage (J-V) characteristics measured under the described conditions. The J-V characteristics are clearly non-linear, and at voltage greater than 1.3V, current instabilities are observed (Figure 4.18 (a)). Current density as function of temperature under reverse bias V=0.2V is illustrated in Figure 4.18(b).

(a)   (b)
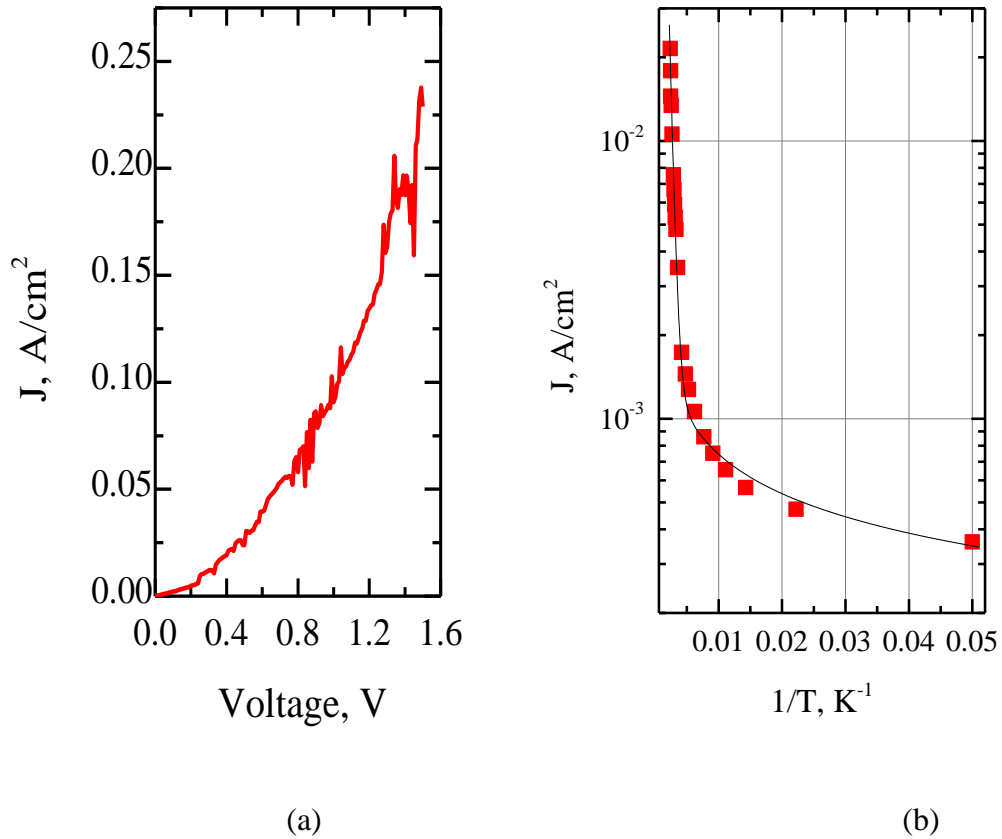
Figure 4.18 (a) I-V characteristics of NWs, (b) current density as function of temperature under reverse bias V=0.2V.
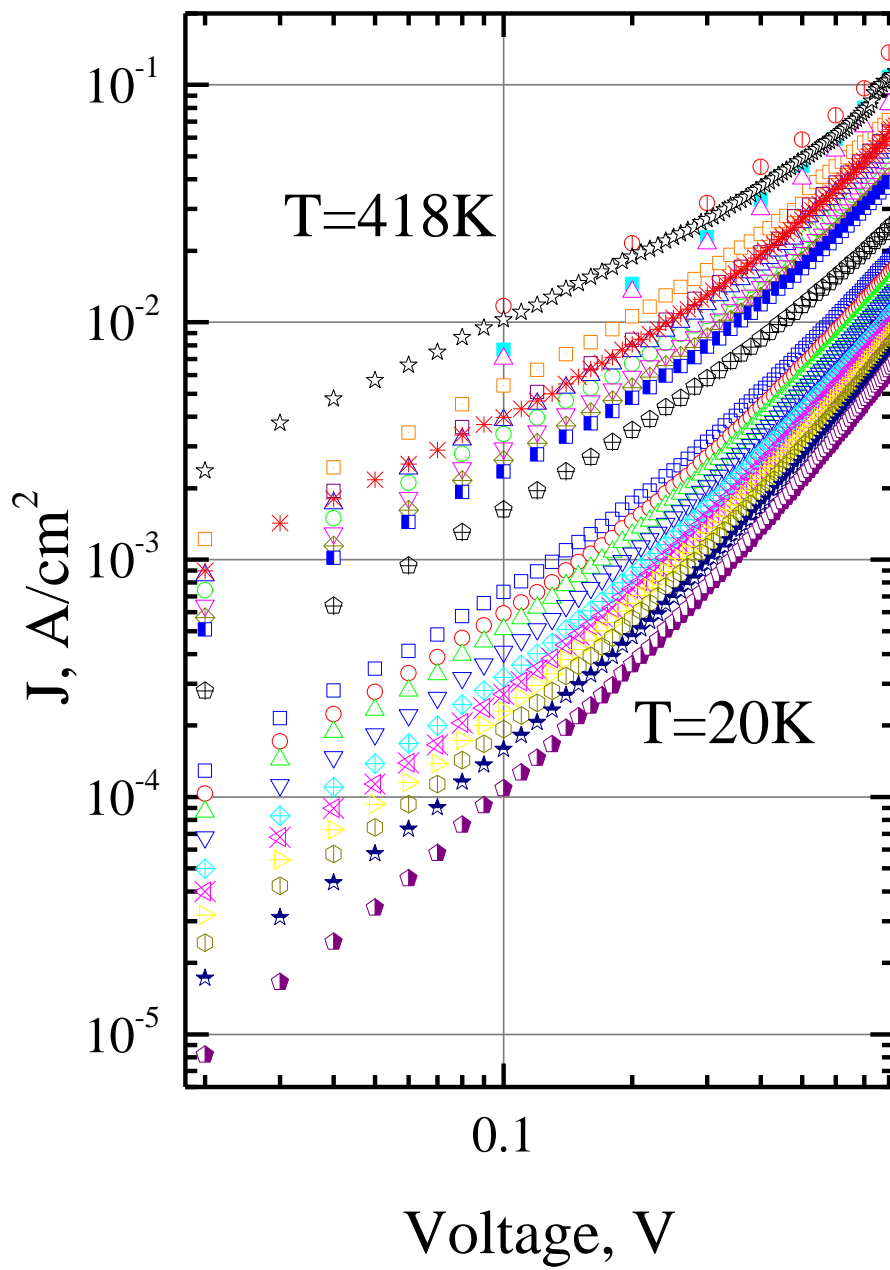
Figure 4.19 J-V characteristics of NWs at different temperatures under reverse bias.

Figure 4.20 shows current as function of time at applied voltage of 6 V. We clearly see that within the $10^{-7} - 10^{-6}$ s time domain, these instabilities have both stochastic and periodic components.
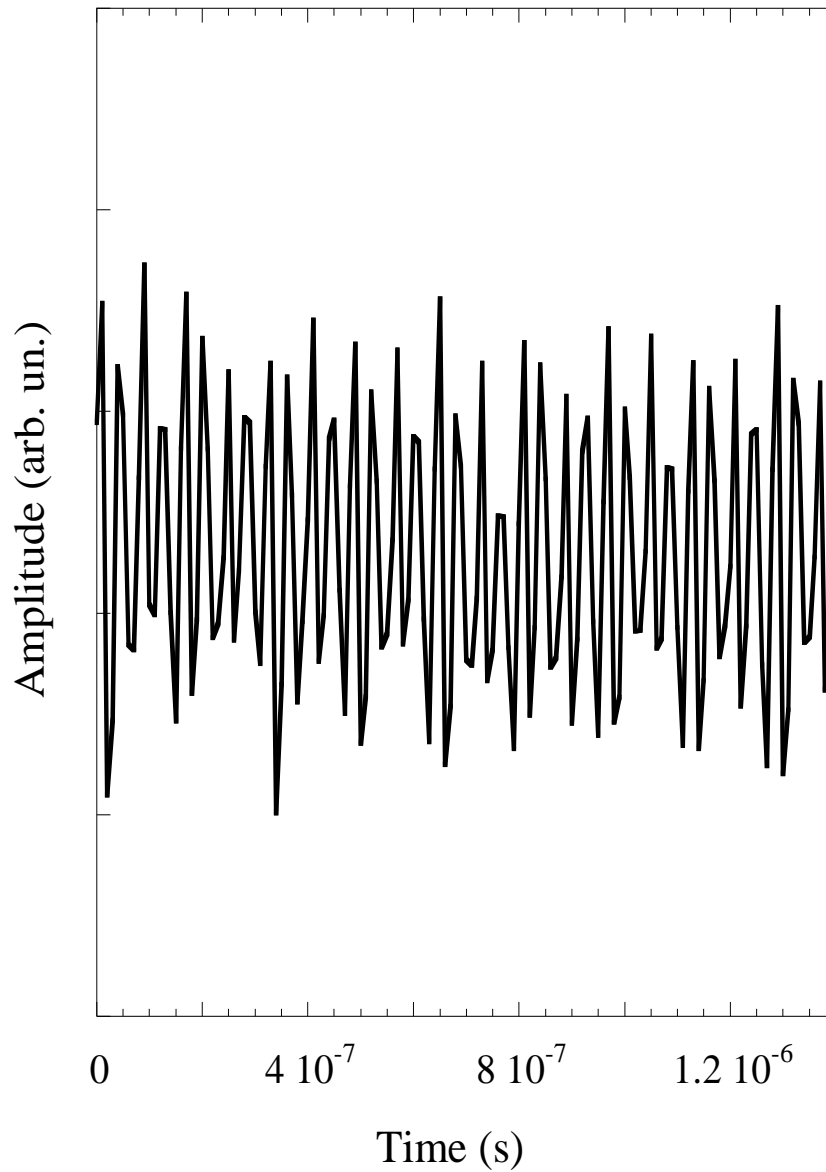
Figure 4.20 Current as function of time at applied voltage of 6V.
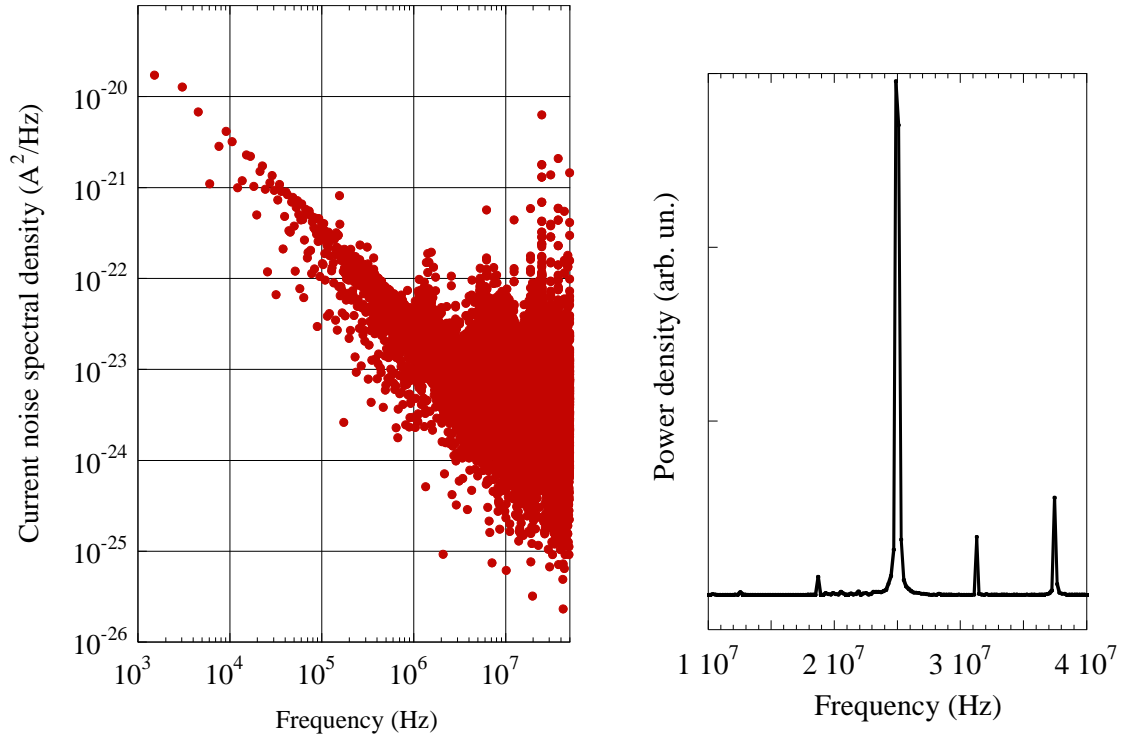
Figure 4.21 (a) Current noise spectral density and (b) power density frequency dependence at frequency domain.

Figure 4.21(a) shows current noise spectral density frequency dependence, which has a dominant 1/f frequency component up to $f \approx 10^6$ Hz. At the same time, a peak near $2.5 \cdot 10^7$ Hz is observed. Figure 4.21(b) confirms presence of a reasonably narrow peak at this frequency with, most likely, harmonics at lower and higher frequencies.

4.3.2   Discussion

We found the temperature dependence in the I-T curve from two parts. Those low temperature emissions are suggested relating localized states or carriers, while high temperatures increase the density of states, and the thermal generated carriers.

These dependences were fitted the following two formulas:

For T> 80K,

$$y = A*exp(R0*x)+y0*(x^\wedge A0) \qquad (4.43)$$

For T ≤ 80K,

$$y =y0*(x^\wedge A0) \qquad (4.44)$$

where *y0, A0, R0, A* are fitting parameters, their values are listed in the inset of Figure 4.22. Activation energy is estimated to be 170mV.
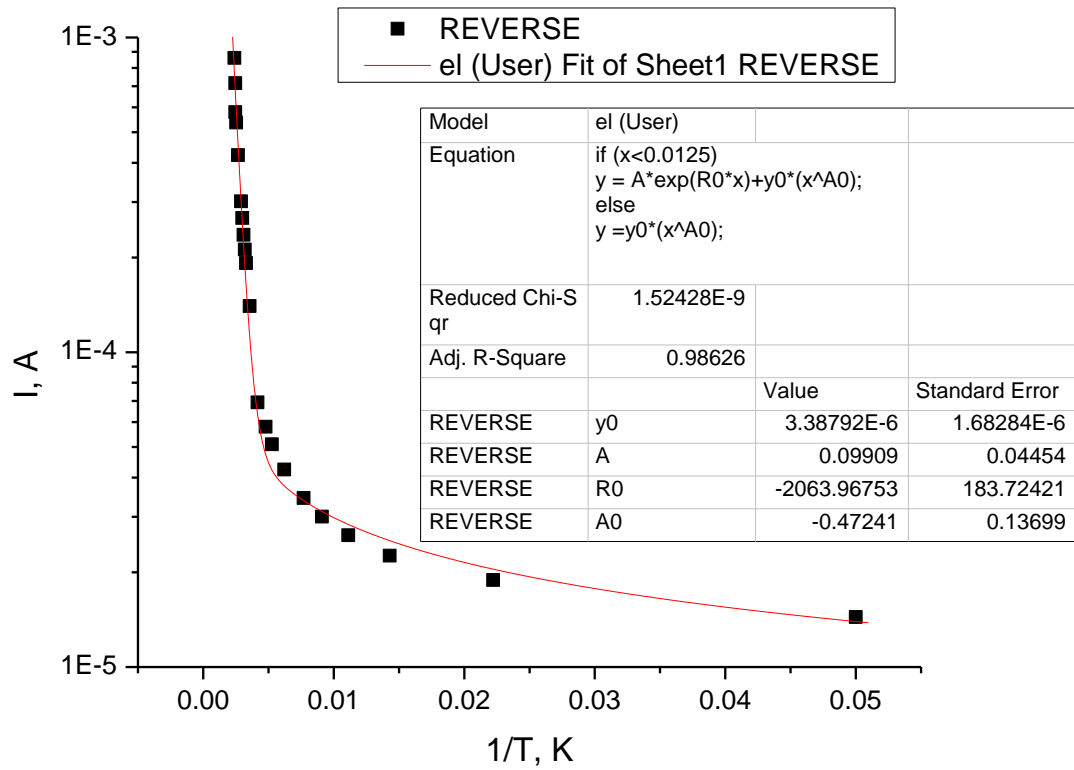
Figure 4.22 Current dependence on temperature at V= 0.2 V for reverse bias.

Averaging current instabilities 100 or more times, we find almost pure damped oscillations with frequency of 25 MHz (Figure 4.23).
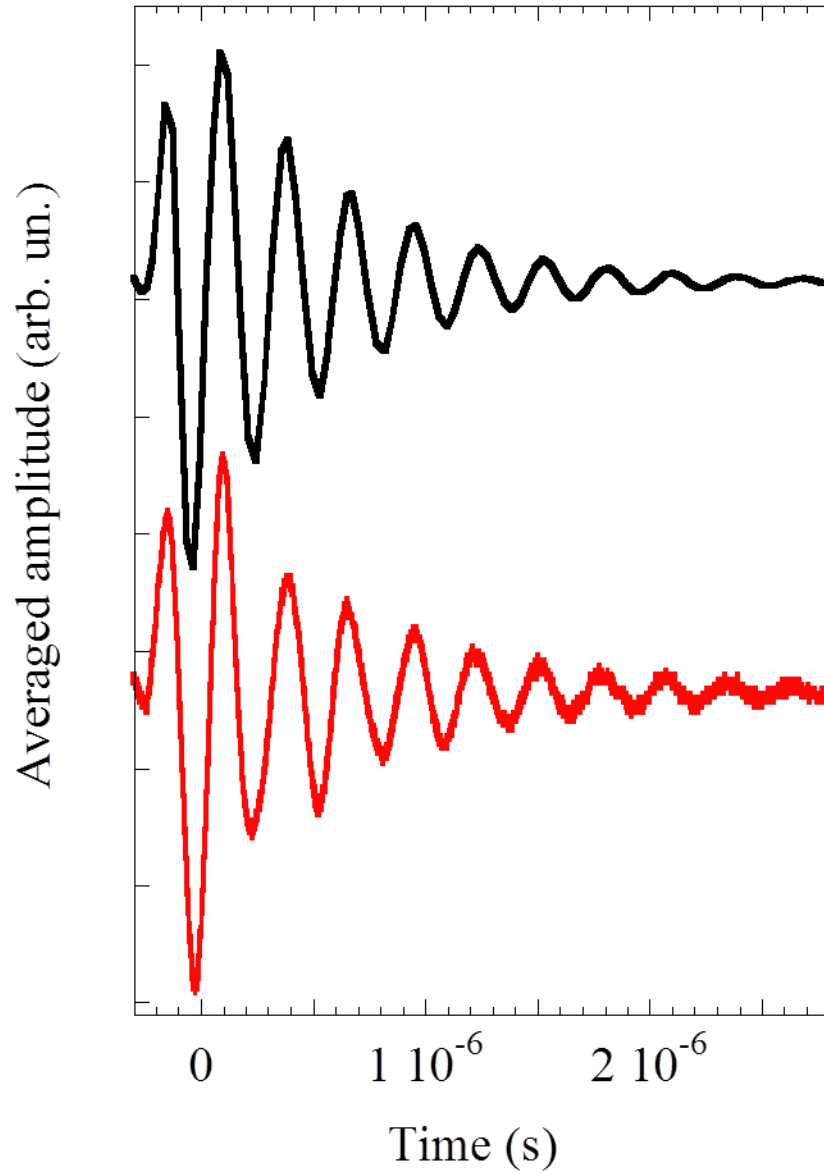
Figure 4.23 Time domain current instabilities (red) and circuit simulated pure damped oscillations (black) with frequency of 25 MHz biased in 0.5V DC coupling.

Typically, electrical measurements in elemental group IV semiconductor NWs show linear, or close to linear, I-V characteristics with resistivity estimated to be close to bulk resistance of an undoped Si or Ge.

Our Si/Ge NW lengths and diameters are similar to the reported in Ref. [208], but the resistance is two-three orders of magnitude higher (Figure 4.18(a)). This could be due a higher series resistance at the NW/probe interface (which is unlikely, because similarly to Ref. [208] the NW tips are covered by Au) or due to presence of the Ge-Si NW HJs. The observed non-linearity in I-V characteristics suggests that a NW Ge-Si HJ, not a series resistance, controls electric current.

Current noise in semiconductor nanostructures has been studied intensively [209-212]. Usually, such studies are focused on various noise components. To separate the noise contributions to our NW samples. There are four distinctly different sources: NW surface, NW bulk NW contact and NW HJ. NW surface has a large number of surface defects. From the oldest McWhorther's model [137], flicker noise is attributed to electron random trapping and detrapping in surface states. In Hooge's model [138, 213], the flicker noise is attributed to carrier density and mobility fluctuation mechanisms. Some surface treatments also affect carrier mobility. The surface generates only a fraction of the flicker noise. A wide range of mechanisms including thermal modulation effects, diffusivity fluctuations, trapping mechanisms with distributed time constants, and variations in surface recombination velocity. Either white noise or shot noise drive to stochastic component. shot noise is depressed by space charge. The potential developed by the space charge could further eliminate the number of carriers emitted, the various arrivals of the carriers are reduced.

Thermal current noise density is frequency independent, and it can be estimated as $N_i = \frac{4k_BT}{R}$, where k_B is the Boltzmann constant, T is temperature and R is the sample resistance. The estimated at room temperature thermal noise is many orders of magnitude lower than the experimentally observed in this study. Current noise spectral density is in the frequency range of 10^3-10^8 Hz (Figure 4.21(a)), and it can be neglected. Strong flicker noise with the 1/f frequency dependence (which is in our measurements the dominant current noise component from 10^3 to 10^6 Hz) has been observed in many nanostructures including carbon nanotubes, semiconductor and metal nanowires and others [214, 215]. There are three distinctly different sources of current noise in semiconductor NWs: NW surface, NW bulk and NW contacts. In general, semiconductor NW surface has a large number of surface defects. Charge carriers are captured on and escaped from these defects, and the fluctuating localized charges interfere with mobile carriers within bulk of the NWs. A large surface-to-volume ratio in thin (< 30 nm diameter) NWs is responsible for a significant impact on electron transport through NWs, and various surface treatments might affect the NW carrier mobility and current noise [216]. However, most of the Ge-Si NWs in this study have a larger diameter ($\sim$ 100 nm), and the surface component of current noise is expected to be less important. Current noise associated with the NW electrical contact is proportional to contact resistance, and in the case of bulk resistance being greater than contact resistance can be neglected as well. The observed non-linear current I-V characteristics in our measurements (Figure 4.18(a)) suggest that electrical conductivity and current noise are mostly controlled by the Ge-Si axial NW HJ. Also, compared to elemental Si NWs [208], current noise spectral density in Ge-Si axial NW HJs is 10^4-10^5 times greater.
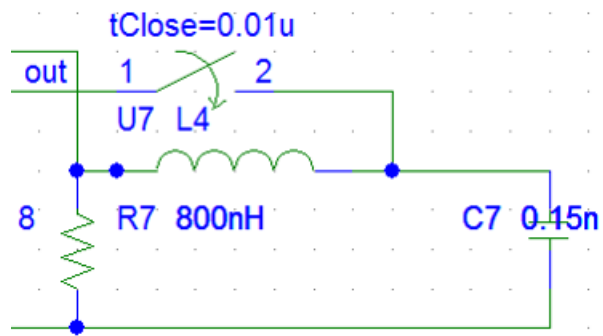
Figure 4.24 Spice simulation circuit biased in 0.5V DC coupling.

CHAPTER 5

CONLUSION AND FUTURE WORK

5.1   Conclusion

The axial Si/Ge NW HJs with quality core crystallinity are demonstrated through Au-catalyzed VLS growth fabrication procedure. Spontaneous intermixing at the Si/Ge heterointerface and lateral expansion of the Ge segment of the nanowire partially relieves the lattice mismatch induced strain. The Raman and PL spectra confirmed the existence of this Si/Ge nanowire heterointerface and the lattice mismatch induced strain. With a Si/Ge NW diameter in the range 70–120nm, surface-related structural defects and imperfections do not fully control carrier recombination in the Si/Ge NW HJs, and the PL signal associated with band-to-band electron-hole recombination at the Si/Ge NW HJ has been measured and attributed to the $Si_{1-x}Ge_x$ alloy composition revealed by EDX. The PL associated with the Si segment of the Si/Ge NW HJ exhibits a peak shift toward higher photon energy as the temperature increases from 20K to above room temperature, indicating compressive stress due to the mismatch in Si and Ge CTEs and, possibly, NW bending. Raman scattering measurements performed under laser excitation varying from 100 to 700W/cm^2 clearly show that Si/ Ge NW temperature can increase by as much as 110K. The effect of heating induced by this laser irradiation results in an additional shift of the Raman peak position and asymmetric broadening. In particular, the observed asymmetric line shape of the first order phonon Raman peak is associated with the formation of high excitation power densities create a high density of free carriers, which can interfere with the phonon scattering. This temperature increase produces an unexpected

shift of the Raman peak associated with Si-Si (Ge) vibration mode toward higher wavenumbers indicating strong (2–3 GPa) compressive strain. This conclusion is supported by the Raman polarization dependence in Si/Ge axial NW HJs.

Performed electrical measurements demonstrate the predicted strong current instabilities and quasi-periodic oscillations in Si/Ge NW HJs. The noise power spectra are consistent with flicker noise with an additional high-frequency component at ~ 25 MHz. Flicker noise is attributed to carrier capture on and release from NW surface states. The proposed explanation of high frequency oscillations involves electron transitions from Ge to Si segments of the NWs, which requires momentum scattering and leads to electron deceleration and current flow disruption at the Ge/Si heterointerface.

5.2   Future Work

The following issues have to be resolved to further understand the properties of VLS grown axial Si/Ge NW HJs.

I.   Additional measurements on Raman scattering with different diameter of Si/Ge NW HJs samples can be performed. Because the smaller diameter wires are proposed to be resonantly selected by shorter-wavelength excitation, thus they exhibit a larger downshift of the Raman band.

II. Additional measurements on modulation spectroscopy can be performed using NWs of different diameters.

III. More measurements of Raman scattering polarization dependence in Si/Ge NW HJs samples can be used to identify the disorder and associated structural defects. These measurements can be combined with studies of resonant Raman scattering in Si/Ge NW HJs samples.

IV. Additional measurements on the expected and weak observed negative photoconductivity in Si/Ge NW HJs samples (e.g., as function of temperature, light intensity, etc.) and model the obtained experimental results. Because the photoconductivity has been the parameter most often used to characterize the quality of material.

V. Developments in the growth technology can be developed in concurrent improvements in the photoconductivity and some of the other optoelectronic properties of the nanowire.

Our results show the used VLS growth method provides limited control over the compositional modulation and properties of the SiGe transition layer at the hetero-interface. The key to improve this control is to find a catalyst which could lead to a lower solubility of Si and Ge; thus, the reservoir effect that accounts for the smearing of compositional changes could be avoided. We believe that this can be done using VLS as well as Vapor-Solid-Solid (VSS) techniques. We think that a solid catalyst could be similarly advantageous in forming abrupt doping profiles, such as are required for the high-subthreshold slope devices such as tunnel and avalanche field-effect transistors and high-speed ETDs. Also, Si and Ge device fabrication that requires sophisticated control of composition at low temperature can be addressed using this approach.

REFERENCES

[1] D. Ahn, C. Hong, J. Liu, W. Giziewicz, M. Beals, L. C. Kimerling, J. Michel, J. Chen, and F. X. Kärtner, "High performance, waveguide integrated Ge photodetectors." Opt. Express, vol. 15, p. 3916, 2007.

[2] J. Michel, J. Liu, and L. C. Kimerling, "High-performance Ge-on-Si photodetectors." Nat. Photonics vol. 4, p. 527, 2010.

[3] S. Assefa, F. Xia, S. W. Bedell, Y. Zhang, T. Topuria, P. M. Rice, and Y. A. Vlasov, "Reinventing germanium avalanche photodetector for nanophotonic on-chip optical interconnects." Opt. Express, vol. 18, p. 4986, 2010.

[4] T. Yin, R. Cohen, M. M. Morse, G. Sarid, Y. Chetrit, D. Rubin, and M. J. Paniccia, "31GHz Ge *n-i-p* waveguide photodetectors on Silicon-on-Insulator substrate." Opt. Express, vol. 15, p. 13965, 2007.

[5] J. Liu, X. Sun, R. Camacho-Aguilera, L. C. Kimerling, and J. Michel, "Ge-on-Si laser operating at room temperature." Opt. Lett., vol. 35, p. 679, 2010.

[6] R. E. Camacho-Aguilera, Y. Cai, N. Patel, J. T. Bessette, M. Romagnoli, L. C. Kimerling, and J. Michel, "An electrically pumped germanium laser." Opt. Express, vol. 20, p. 11316, 2012.

[7] J. Liu, X. Sun, L. C. Kimerling, and J. Michel, "Direct-gap optical gain of Ge on Si at room temperature." Opt. Lett., vol. 34, p. 1738, 2009.

[8] D. J. Paul, "Si/SiGe heterostructures: from material and physics to devices and circuits." Semicond. Sci. Technol., vol. 19, pp. R75-R108, 2004.

[9] Y. Shiraki and A. Sakai, "Fabrication technology of SiGe hetero-structures and their properties." Surf. Sci. Rep., vol. 59, p. 153, 2005.

[10] H. Ye and J. Yu, "Germanium epitaxy on silicon." Sci. Technol. Adv. Mater., vol. 15, p. 024601, 2014.

[11] K. Saraswat, C. O. Chui, T. Krishnamohan, D. Kim, A. Nayfeh, and A. Pethe, "High performance germanium MOSFETs." Mater. Sci. Eng. B, vol. 135, p. 242, 2006.

[12] S. S. Iyer, G. L. Patton, J. Stork, B. S. Meyerson, and D. L. Harame, "Heterojunction bipolar transistors using Si-Ge alloys." IEEE Trans. Electron Devices, vol. 36, p. 2043, 1989.

[13] D. K. Nayak, K. Goto, A. Yutani, J. Murota, and Y. Shiraki, "High-mobility strained-Si PMOSFET's." IEEE Trans. Electron Devices, vol. 43, p. 1709, 1996.

[14] V. A. Shah, A. Dobbie, M. Myronov, and D. R. Leadley, "Reverse graded SiGe/Ge/Si buffers for high-composition virtual substrates." J. Appl. Phys., vol. 107, p. 064304, 2010.

[15] Y. W. Mo, D. E. Savage, B. S. Swartzentruber, and M. G. Lagally, "Kinetic pathway in Stranski-Krastanov growth of Ge on Si (001)." Phys. Rev. Lett., vol. 65, p. 1020, 1990.

[16] O. G. Schmidt, O. Kienzle, Y. Hao, K. Eberl, and F. Ernst, "Modified Stranski–Krastanov growth in stacked layers of self-assembled islands." Appl. Phys. Lett., vol. 74, p. 1272, 1999.

[17] J. M. Baribeau, X. Wu, N. L. Rowell, and D. J. Lockwood, "Ge dots and nanostructures grown epitaxially on Si." J. Phys.: Condens. Matter, vol. 18, p. R139, 2006.

[18] H. K. Shin, D. J. Lockwood, and J. M. Baribeau, "Strain in coherent-wave SiGe/Si superlattices." Solid State Commun., vol. 114, p. 505, 2000.

[19] A. P. Levitt, Whisker Technology, New York, NY: John Wiley 1970.

[20] T. I. Kamins, X. Li, R. S. Williams, and X. Liu, "Growth and structure of chemically vapor deposited Ge nanowires on Si substrates." Nano Lett., vol. 4, p. 503, 2004.

[21] J. B. Hannon, S. Kodambaka, F. M. Ross, and R. M. Tromp, "The influence of the surface migration of gold on the growth of silicon nanowires." Nature, vol. 440, p. 69, 2006.

[22] N. D. Zakharov, P. Werner, G. Gerth, L. Schubert, L. Sokolov, and U. Gösele, "Growth phenomena of Si and Si/Ge nanowires on Si (111) by molecular beam epitaxy." J. Cryst. Growth, vol. 290, p. 6, 2006.

[23] L. J. Lauhon, M. S. Gudiksen, D. Wang, and C. M. Lieber, "Epitaxial core–shell and core–multishell nanowire heterostructures." Nature, vol. 420, p. 57, 2002.

[24] J. Xiang, W. Lu, Y. Hu, Y. Wu, H. Yan, and C. M. Lieber, "Ge/Si nanowire heterostructures as high-performance field-effect transistors." Nature, vol. 441, p. 489, 2006.

[25] G. Kästner and U. Gösele, "Stress and dislocations at cross-sectional heterojunctions in a cylindrical nanowire." Philos. Mag., vol. 84, p. 3803, 2004.

[26] E. Ertekin, P. A. Greaney, D. C. Chrzan, and T. D. Sands, "Equilibrium limits of coherency in strained nanowire heterostructures." J. Appl. Phys., vol. 97, p. 114325, 2005.

[27] Q.-T. Zhao, S. Richter, C. Schulte-Braucks, L. Knoll, S. Blaeser, G. V. Luong, S. Trellenkamp, A. Schaefer, A. Tiedemann, J.-M. Hartmann, K. Bourdelle, and

135

S.Mantl, "Strained Si and SiGe nanowire tunnel fets for logic and analog applications." IEEE J. Electron Devices Soc., vol.3, pp. 103–114, 2015.

[28] J. Teherani, W. Chern, D. Antoniadis, and J. Hoyt, "Simulation of enhanced hole ballistic velocity in asymmetrically strained germanium nanowire trigate p-MOSFETs." IEEE IEDM, pp. 32.4.1–32.4.4, 2013.

[29] Y. Jiang et. al., "Ge-rich (70%) SiGe nanowire MOSFET fabricated using pattern-dependent Ge-condensation technique." IEEE Electron Device Lett., vol. 29, no. 6, pp. 595–598, 2008.

[30] M. T. Björk, B. J. Ohlsson, C. Thelander, A. I. Persson, K. Deppert, L. R. Wallenberg, and L. Samuelson, "Nanowire resonant tunneling diodes." Appl. Phys. Lett., vol. 82, pp. 4458-4460, 2002.

[31] C. Thelander, T. Mårtensson, M. T. Björk, B. J. Ohlsson, M. W. Larsson, L. R. Wallenberg, and L. Samuelson, "Single-electron transistors in heterostructure nanowires." Appl. Phys. Lett., vol. 83, pp. 2052-2054, 2003.

[32] X. Wang, L. Tsybeskov, T. I. Kamins, X. Wu, and D. J. Lockwood, "Structural and optical properties of axial silicon-germanium nanowire heterojunctions." J. Appl. Phys., vol. 118, p. 234301, 2015.

[33] U. Givan, M. Kwiat, F. Patolsky, "The Influence of Doping on the Chemical Composition, Morphology and Electrical Properties of $Si_{1-x}Ge_x$ Nanowires." J. Phys. Chem. C, vol. 114, p. 4331, 2001.

[34] S. J. Whang, S. J. Lee, W. F. Yang, B. J. Cho, D. L. Kwong, "Study on the synthesis of high quality single crystalline $Si_{1-x}Ge_x$ nanowire and its transport properties." Appl. Phys. Lett. vol. 91, p. 072105, 2007.

[35] S. A. Dayeh, R. M. Dickerson, S. T. Picraux, "Advanced core/multishell germanium/silicon nanowire heterostructures: Morphology and transport." Appl. Phys. Lett., vol. 99, p. 113105, 2011.

[36] S. T. Le, P. Jannaty, X. Luo, A. Zaslavsky, D. E. Perea, S. A. Dayeh, S. T. Picraux, "Axial SiGe heteronanowire tunneling field-effect transistors." Nano Lett. vol. 12, p. 5850, 2012.

[37] M. H., Huang, S. Mao, H. Feick, H. Yan, Y. Wu, H. Kind, E. Weber, R. Russo, and P. Yang. "Room-temperature ultraviolet nanowire nanolasers." Science, vol. 292, pp. 1897-1899, 2001.

[38] M. Amato, M. Palummo, R. Rurali, S. Ossicini, "Silicon-germanium nanowires: chemistry and physics in play, from basic principles to advanced applications." Chem. Rev., vol. 114, pp. 1371–1412, 2014.

[39] N. P. Dasgupta, J. Sun, C. Liu, S. Brittman, S. C. Andrews, J. Lim, H. Gao, R. Yan, and P. Yang, "Semiconductor nanowires – synthesis, characterization, and applications." Adv. Mater., vol. 26, pp. 2137–2184, 2014.

[40] A. Potié et al., "Growth and characterization of gold catalyzed SiGe nanowires and alternative metal-catalyzed Si nanowires." Nanoscale Res. lett., vol. 6, p. 187, 2011.

[41] E. Dornel, T. Ernst, J. C. Barbé, J. M. Hartmann, V. Delaye, F. Aussenac, C. Vizioz, S. Borel, V. Maffini-Alvaro, C. Isheden, and J. Foucher, "Hydrogen annealing of arrays of planar and vertically stacked Si nanowires." Appl Phys Lett, vol. 91, p. 233502, 2007.

[42] B. V. Kamenev, J.-M. Baribeau, D.J. Lockwood, L. Tsybeskov, "Optical properties of Stranski–Krastanov grown three-dimensional $Si/Si_{1-x}Ge_x$ nanostructures." Phys. E: Low-dimensional Systems and Nanostructures, vol. 26, pp. 174-179, 2005

[43] D. J. Eaglesham and M. Cerullo, "Dislocation-free Stranski-Krastanow growth of Ge on Si (l00)." Phys. Rev. Lett., vol. 64, p. 1943, 1990.

[44] F. K. LeGoues, B. S. Meyerson, and J. F. Morar, "Anomalous strain relaxation in SiGe thin films and superlattices." Phys. Rev. Lett., vol. 66, p. 2903, 1991.

[45] B. V. Kamenev, H. Grebel, L. Tsybeskov, T. I. Kamins, R. S. Williams, J. M. Baribeau, and D. J. Lockwood, "Polarized Raman scattering and localized embedded strain in self-organized Si/Ge nanostructures." Appl. Phys. Lett., vol. 83, pp. 5035-5037, 2003.

[46] D. J. Lockwood, X. Wu, J.-M. Baribeau, S. A. Mala, X. Wang, and L. Tsybeskov, "Si/SiGe interfaces in three-, two-, and one-dimensional nanostructures and their influence on SiGe light emission." Electrochem. Soc., pp. 2096-2096, 2016.

[47] R. S. Wagner and W. C. Ellis, "Vapor-Liquid-Solid mechanism of single crystal growth." Appl. Phys. Lett., vol. 4, p. 89, 1964.

[48] Y. Wu and P. Yang, "Direct observation of vapor-liquid-solid nanowire growth." J. Am. Chem. Soc., vol. 123, pp. 3165-3166, 2001.

[49] A.M. Morales and C.M. Lieber, "A Laser ablation method for the synthesis of crystalline semiconductor nanowires." Science, vol.279, pp. 208-211, 1998.

[50] Y. Wu, H. Yan, M. Huang, B. Messer, J.H. Song, P. Yang, "Inorganic semiconductor nanowires: rational growth, assembly, and novel properties." Chem. Eur. J., vol. 8, p. 1260, 2002.

[51] J. Westwater, D. P. Gosain, S. Tomiya, S.Usui, and H.Ruda, "Growth of silicon nanowires via gold/silane vapor–liquid–solid reaction." J. Vac. Sci. Technol. B, vol. 15, p. 554, 1997.

[52] A. I. Hochbaum, R. Fan, R. He, and P. Yang, "Controlled growth of Si nanowire arrays for device integration." Nano Lett., vol. 5, pp. 457–460, 2005.

[53] L. Gangloff, E. Minoux, K.B.K. Teo, P. Vincent, V. Semet, V.T. Binh, M.H. Yang, I.Y.Y. Bu, R.G. Lacerda, G. Pirio, J.P. Schnell, D. Pribat, D.G. Hasko, G.A.J. Amaratunga, W.I. Milne and P. Legagneux. "Self-aligned, gated arrays of individual nanotube and nanowire emitters." Nano Lett., vol. 4, p. 1575, 2004.

[54] M. S. Islam, S. Sharma, T.I. Kamins, R.S. Williams, "Ultrahigh-density silicon nanobridges formed between two vertical silicon surfaces." Nano technol., vol. 15, p. L5, 2004.

[55] H. Y. Chang, L. Tsybeskov, S. Sharma, T. I. Kamins, X. Wu, and D. J. Lockwood, "Photoluminescence and Raman scattering in axial Si/Ge nanowire heterojunctions." Appl. Phys. Lett., vol. 95, p. 133120, 2009.

[56] S. Sharma, T. I. Kamins, and R. S. Williams, "Synthesis of thin silicon nanowires using gold-catalyzed chemical vapor deposition." Appl. Phys. A, vol. 80, p. 1225, 2005.

[57] B. V. Kamenev, V. Sharma, L. Tsybeskov, and T. I. Kamins, "Optical properties of Ge nanowires grown on Si (100) and (111) substrates: Nanowire–substrate heterointerfaces." Phys. Status Solidi A, vol. 202, p. 2753, 2005.

[58] L. Vincent, R. Boukhicha, N. Cherkashin, S. Reboh, G. Patriarche, C. Renard, V. Yam, F. Fossard and D. Bouchier, "Composition and local strain mapping in Au-catalyzed axial Si/Ge nanowires." Nano technol., vol. 23, p. 395701, 2012.

[59] R. Dujardin, V. Poydenot, T. Devillers, V. Favre-Nicolin, P. Gentile, and A. Barski, "Growth mechanism of Si nanowhiskers and SiGe heterostructures in Si nanowhiskers: X-ray scattering and electron microscopy investigations." Appl. Phys. Lett., vol. 89, p. 153129, 2006.

[60] C.-Y. Wen, M. C. Reuter, J. Bruley, J. Tersoff, S. Kodambaka, E. A. Stach, F. M. Ross, "Formation of compositionally abrupt axial heterojunctions in silicon-germanium nanowires." Science, vol. 326, p. 1247, 2009.

[61] F. G. Adams, Macroeconomics for Business and Society: A Developed/Developing Country Perspective on the "New Economy", Singapore, Singapore.: World Scientific, 2002.

[62] Y. Wu, R. Fan, P. Yang, "Block-by-block growth of single-crystalline Si/SiGe superlattice nanowires." Nano Lett., vol. 2, pp. 83–86, 2002.

[63] F. C. Frank and J. H. van der Merwe, "One-dimensional dislocations. I. Static theory." Proc. R. Soc. London, Ser. A, vol. 198, p. 205, 1949.

[64] J. H. Van der Merwe, "Crystal interfaces. Part II. Finite Overgrowths." J. Appl. Phys., vol. 34, pp. 123–127, 1963.

[65] J. W. Matthews, and A. E. Blakeslee, "Defects in epitaxial multilayers: I. misfit dislocations." J. Cryst. Growth, vol. 27, p. 118, 1974.

[66] J. W. Matthews, "Defects associated with the accommodation of misfit between crystals." J. Vac. Sci. Technol., vol. 12, p. 126, 1975.

[67] J. D. Cressler, G. Niu, Silicon-germanium Heterojunction Bipolar Transistors, London, England: Artech House, 2002.

[68] W. R. Stone, Review of Radio Science: 1999-2002 URSI, New York, NY: John Wiley & Sons, 2002.

[69] B. Jalali, M. Paniccia, and G. Reed, "Silicon photonics." IEEE Microw. Mag., vol. 7, pp. 58–68, 2006.

[70] A. K. Sood, J. W. Zeller, R. A. Richwine, Y. R. Puri, H. Efstathiadis, P. Haldar, N. K. Dhar, and D. L. Polla. "SiGe based visible-NIR photodetector technology for optoelectronic applications." Chapter in Advances in Optical Fiber Technology: Fundamental Optical Phenomena and Applications, edited by M. Yasin, H. Arof, and SW Harun, Croatia: Intech, 2015.

[71] T. E. Clark, P. Nimmatoori, K.-K. Lew, L. Pan, J. M. Redwing, and E. C. Dickey, "Diameter dependent growth rate and interfacial abruptness in Vapor–Liquid–Solid Si/Si$_{1-x}$Ge$_x$ heterostructure nanowires." Nano Lett., vol. 8, pp. 1246-1252, 2008.

[72] L. Vivien, L. Pavesi, Handbook of Silicon Photonics, Boca Raton, CA: Taylor& Francis, 2016.

[73] J. P. Dismukes, L. Ekstrom, and R. J. Paff, "Lattice parameter and density in germanium-silicon alloys." J. Phys. Chem., vol. 35. pp. 3021-3027, 1964.

[74] R. W Olesinski, G. J. Abbaschian, "The Ge−Si (Germanium-Silicon) system." Bull. Alloy Phase Diagr., vol. 5, pp. 180-183, 1984.

[75] L. Colace, G. Masini, V. Cencelli, F. DeNotaristefani, and G. Assanto, "A near-infrared digital camera in polycrystalline germanium integrated on silicon." IEEE J. Sel. Top. Quant. Electron., vol. 43, pp. 311-315, 2007.

[76] J. Liu, R. Camacho-Aguilera, J. T. Bessette, X. Sun, X. Wang, Y. Cai, L. C. Kimerling, and J. F. Michel, "Ge-on-Si optoelectronics." Thin Sol. Films, vol. 520, pp. 3354-3360, 2012.

139

[77] R. K. Schaevitz, J. E. Roth, S. Ren, O. Fidaner, and D. A. B. Miller, "Material properties in Si-Ge/Ge quantum wells." IEEE J. Sel. Top. Quantum Electron., vol. 14, pp. 1082-1089, 2008.

[78] Y. Ishikawa, K. Wada, D. D. Cannon, J. Liu, H. Luan, and L. C. Kimerling, "Strain-induced band gap shrinkage in Ge grown on Si substrate." Appl. Phys. Lett., vol. 82, p. 2044, 2003.

[79] D. D. Cannon, J. Liu, Y. Ishikawa, K. Wada, D. T. Danielson, S. Jongthammanurak, J. Michel, and L. C. Kimerling, "Tensile strained epitaxial Ge films on Si (100) substrates with potential application in Lband telecommunications." Appl. Phys. Lett., vol. 84, p. 906, 2004.

[80] J. M. Hartmann, A. Abbadie, A. M. Papon, P. Holliger, G. Rolland, T. Billon, J. M. Fédéli, M. Rouvière, L. Vivien, and S. Laval, "Reduced pressure–chemical vapor deposition of Ge thick layers on Si (001) for 1.3–1.55- μm photodetection." J. Appl. Phys., vol. 95, p.5905, 2004.

[81] Y. Ishikawa, K. Wada, J. F. Liu, D. D. Cannon, H. C. Luan, J. Michel and L. C. Kimerling, "Strain-induced enhancement of near-infrared absorption in Ge epitaxial layers grown on Si substrate." J. Appl. Phys., vol. 98, pp. 013501-013501-9, 2005.

[82] C. Van de Walle, "Band lineups and deformation potentials in the model-solid theory." Phys. Rev. B, vol. 39, no. 3, pp. 1871–1883, 1989.

[83] J. F. Liu, R. Camacho-Aguilera, X. Sun, X. X. Wang, Y. Cai, L.C. Kimerling, J. Michel, Reprinted from Thin Solid Films, Ge-on-Si Optoelectronics, Amsterdam, Netherlands: Elsevier, vol. 520, pp. 3354–3360, 2011.

[84] A. Abudukelimu, W. Yasenjiang, K. Kakushima, P. Ahmet, M. Geni, K. Natori and H. Iwai, "Influence of strained drain on performance of ballistic channel devices." Semicond. Sci. Technol., vol. 27, p. 055001, 2012.

[85] L. Yang, J. R. Watling, R. C W Wilkins, M. Boriçi, J. R Barker, A. Asenov and S. Roy, "Si/SiGe heterostructure parameters for device simulations." Semicond. Sci. Technol., vol. 19, pp. 1174–1182, 2004.

[86] C. Pickering, R. T. Carline, D. J. Robbins, W. Y. Leong, S. J. Barnett, A. D. Pitt, and A. G. Cullis, "Spectroscopic ellipsometry characterization of strained and relaxed $Si_{1-x}Ge_x$ epitaxial layers." J. Appl. Phys., vol. 73, p. 239, 1993.

[87] F. H. Pollak, Effects of Homogeneous Strain on The Electronic and Vibrational Levels in Semiconductors and Semimetals, New York, NY: Academic, 1990.

[88] F. Schäffler, "High-mobility Si and Ge structures." Semicond. Sci. Technol., vol. 12, pp. 1515-1549, 1997.

[89] D. V. Lang, R. People, J. C. Bean, and A. M. Sergent, "Measurement of the band gap of $Si_{1-x}Ge_x$ /Si strained-layer heterostructures." Appl. Phys. Lett., vol. 47, pp. 1333-1335, 1985.

[90] L. Ruiz, "Extraction of large valence-band energy offsets and comparison to theoretical values for strained-Si/strained-Ge type-II heterostructures on relaxed SiGe substrates." Phys. Rev. B, vol. 85, p. 205308, 2012.

[91] F. F. Fang, "2DEG in strained Si/SiGe heterostructures." Surf. Sci., vol. 305 pp. 301-306, 1994.

[92] T. E. whall and E. H. C. Parker, "SiGe heterostructures for FET applications." J. Phys. D: Appl. Phys., vol. 31, pp. 1397-1416, 1998.

[93] F. Stern and S. E. Laux, "Charge transfer and low-temperature electron mobility in a strained Si layer in relaxed $Si_{1-x}Ge_x$." Appl. Phys. Lett., vol. 61, p. 1110, 1992.

[94] J. S. Yuan, SiGe, GaAs and InP Heterojunction Bipolar Transistors, Chapter 2, New York, NY: Wiley, 1999.

[95] W. X. Ni, J. Knall and G.V. Hansoon, "New method to study band offsets applied to strained $Si/Si_{1-x}Ge_x$ (100) heterojunction interfaces." Physics Rev. B, vol. 36, pp. 7744-7748, 1987.

[96] C. H. Gan, J.A. del Alamo, B.R. Bennett, "Si/Si1-xGex valence band discontinuity measurements using a semiconductor-insulator semiconductor (SIS) heterostructure." IEEE Trans. on Electron Devices, vol. 41, pp. 2430-2439, 1994.

[97] A. Nduwimana, X.-Q Wang, "Core and shell states of silicon nanowires under strain." J. Phys. Chem. C, vol. 114, pp. 9702–9705, 2010.

[98] R. N. Musin, X.Q. Wang, "Structural and electronic properties of epitaxial core–shell nanowire heterostructures." Phys. Rev. B, vol. 71, p. 155318, 2005.

[99] D. B. Migas and V. E. Borisenko, "Structural, electronic, and optical properties of ⟨001⟩-oriented SiGe nanowires." Phys. Rev. B, vol. 76, p. 035440, 2007.

[100] X. Peng, and P. Logan, "Electronic properties of strained Si/Ge core-shell nanowires." Appl. Phys. Lett., vol. 96, p. 143119, 2010.

[101] G. Abstreiter, "Physics and perspectives of Si/Ge heterostructures and superlattices." Phys. Scr., vol. T49, pp. 42-45, 1993.

[102] T. Manku and A. Nathan, "Effective mass for strained p-type $Si_{1-x}Ge_x$." J. Appl. Phys., vol. 69, pp. 8414-8416, 1991.

[103] F. Schaffler, in Properties of Advanced Semiconductor Materials GaN, AlN, InN, BN, SiC, SiGe, New York, NY: John Wiley & Sons, Inc., pp. 149-188, 2001.

[104] S. L. Wong, D. Kinder, R. J. Nicholas, T. E. Whall, and R. Kubiak, "Cyclotron-resonance measurements on p-type strained-layer $Si_{1-x}Ge_x$ /Si heterostructures." Physics Rev. B, vol. 51, p. 13499, 1995.

[105] D. Shiri, Y. Kong, A. Buin, and M. P. Anantram. "Strain induced change of bandgap and effective mass in silicon nanowires." Appl. Phys. Lett., vol. 93, p. 073114, 2008.

[106] T. Krishnamohan, Z. Krivokapic, K. Uchida, Y. Nishi, and K. C. Saraswat, "High-mobility ultrathin strained Ge MOSFETs on bulk and SOI with low band-to-band tunneling leakage: Experiments." IEEE Trans. Electron Devices, vol. 53, p. 990, 2006.

[107] D. K. Nayak and S. K. Chun, "Low-field hole mobility of strained Si on (100) $Si_{1-x}Ge_x$ substrate." Appl. Phys. Lett., vol. 64, pp. 2514–2516, 1994.

[108] D. K. Nayak, J. C. S. Woo, J. S. Park, K. L. Wang, and K. P. MacWilliams, "High-mobility p-channel metal-oxide-semiconductor field-effect transistor on Strained Si." Appl. Phys. Lett., vol. 62, pp. 2853-2855, 1993.

[109] K. Ismail, J. O. Chu, and B. S. Meyerson, "High hole mobility in SiGe alloys for device applications." Appl. Phys. Lett., vol. 64, pp. 3124-3126, 1994.

[110] M. V. Fischetti and S. E. Laux, "Band structure, deformation potentials, and carrier mobility in strained Si, Ge, and SiGe alloys." J. Appl. Phys., vol. 80, p.2234, 1996.

[111] G. Abstreiter, H. Brugger, T. Wolf, H. Jorke, and H. J. Herzog, "Strain-induced two-dimensional electron gas in selectively doped Si/ $Si_{1-x}Ge_x$ superlattices." Appl. Phys. Lett., vol. 54, p. 2441, 1985.

[112] C. W. Leitz, M. T. Currie, M. L. Lee, Z.-Y. Cheng, D. A. Antoniadis and E. A. Fitzgerald, "Hole mobility enhancements and alloy scattering-limited mobility in tensile strained Si/SiGe surface channel metal–oxide–semiconductor field-effect transistors." J. Appl. Phys., vol. 92, p. 3745, 2002.

[113] J. Welser, J.L. Hoyt, S. Takagi, and J.F. Gibbons, "Strain dependence of the performance enhancement in strained-Si n-MOSFETs." in IEEE IEDM Tech. Dig., pp. 373-376, 1994.

[114] T. Currie, C. W. Leitz, T. A. Langdo, G. Taraschi, E. A. Fitzgerald, and D. A. Antoniadis, "Carrier mobilities and process stability of strained Si n- and p-PMOSFET's on SiGe virtual substrates." J. Vac. Sci.Tech. B, vol. 19, no. 6, pp. 2268–2279, 2001.

[115] B. V. Zeghbroeck, Principles of semiconductor devices, 2004, book published on the web at http://ece-www. colorado. edu/~ bart/book/book/index. html, 2007.

[116] H. Miyata, T. Yamada, and D. K. Ferry, "Electron transport properties of a strained Si layer on a relaxed Si1-xGex substrate by Monte Carlo simulation." Appl. Phys. Lett., vol. 62, p. 24, 1993.

[117] G. Sasso, N. Rinaldi, G. Matz, and C. Jungemann, "Analytical models of effective DOS, saturation velocity and high-field mobility for SiGe HBTs numerical simulation." SISPAD, vol. B.2, p.15, 2010.

[118] F. M. Bufler, P. Graf, B. Meinerzhagen, B. Adeline, M. M. Rieder, H. Kibbel, and G. Fischer, "Low- and high-field electron-transport parameters for unstrained and strained $Si_{1-x}Ge_x$." IEEE Electron Device Lett., vol. 18, pp. 264-266, 1997.

[119] A. Zunger, "Theoretical predictions of electronic materials and their properties." Curr. Opin. Solid State Mater. Sci., vol. 3, pp. 32-37, 1998.

[120] E. Kasper, K. Lyutovich, Properties of Silicon Germanium and SiGe:Carbide, Edison, NJ: IET, 2000.

[121] C. J. Suresh, M. Willander, Silicon-Germanium Strained Layers and Heterostructures, New York, NY: Academic Press, Inc., 2003.

[122] C. G. Van de Walle and R. M. Martin, "Theoretical calculations of heterojunction discontinuities in the Si/Ge system." Phys. Rev. B, vol. 34, p. 5621, 1986.

[123] C. G. Van de Walle and R. M. Martin, "Theoretical calculations of semiconductor heterojunction discontinuities," J. Vac. Sci. Technol. B, vol. 4, pp. 1055-1059, 1986.

[124] N. A. Hill, S. Pokrant, and A. J. Hill, "Optical properties of Si-Ge semiconductor nano-onions," J. Phys. Chem. B, vol. 103, pp. 3156-3161, 1999.

[125] M. Amato, M. Palummo, and S. Ossicini, "Reduced quantum confinement effect and electron-hole separation in SiGe nanowires." Phys. Rev. B, vol. 79, p. 201302, 2009.

[126] http://www.bls.gov/iif/oshwc/osh/case/ostb1023.pdf. (accessed on 9/29/2016).

[127] J. B. Gunn, "Microwave oscillations of current in III–V semiconductors." Solid State Commun., vol. 1, pp. 88-91, 1963.

[128] http://www.bls.gov/iif/oshwc/osh/case/ostb1023.pdf. (accessed on 9/29/2016).

[129] http://www.bls.gov/iif/oshwc/osh/case/ostb1023.pdf. (accessed on 9/29/2016).

[130] K. C. Kao, Dielectric Phenomena in Solids: With Emphasis on Physical Concepts of Electronic Processes, San Diego, CA: Elsevier Academic Press, 2004.

[131] A. Van der Ziel, Solid State Physical Electronics, Upper Saddle River, NJ: Prentice-Hall Inc., 1976.

[132] M.A. Lampert, P. Mark, Current Injection in Solids, New York, NY: Academic, 1970.

[133] K. C. Kao, "Double injection in solids with non-ohmic contacts. I. Solids without defects." J. of Phys. D: Appl. Phys., vol. 17, p. 1433, 1984.

[134] E. H. Rhoderick, Metal-Semiconductor Contacts, Oxford: Oxford University Press, 1978.

[135] A. Bid, A Bora and A K Raychaudhuri, "1/f noise in nanowires." Nanotechnol., vol. 17, p. 152, 2006.

[136] F. Hooge, "Comparison of 1/f noise theories and experiments." In Noise in Physical Systems and 1/f Noise - 1985: Proceedings of the 8th International Conference on 'Noise in Physical Systems' and the 4th International Conference on '1/f Noise' held in Rome, 1985, New York, NY: Elsevier Science Publishing Company, 1986.

[137] A. McWhorter, "1/f noise and germanium surface properties." Sem.Surf.Phys, 207, 1957.

[138] Buckingham, M. J. Noise in Electronic Devices and Systems. New York, NY: John Wiley & Sons, 1983.

[139] D. M. Fleetwood, and N. Giordano. "lUPhJ Ncf (2)." In Noise in Physical Systems and 1/f Noise: Proceedings of the 7th International Conference on 'Noise in Physical Systems' and the 3rd International Conference on '1/f Noise,' Montpellier, North Holland, vol. 7, p. 201. 1983.

[140] D. M. Fleetwood, and N. Giordano. "Effect of strain on the 1 f noise of metal films." Phys. Rev. B, vol. 28, p. 3625, 1983.

[141] M. B. Weissman, "1/f noise and other slow, nonexponential kinetics in condensed matter." Rev. Mod. Phys., vol. 60, p. 537, 1988.

[142] P. Dutta and P. M. Horn, "Low-frequency fluctuations in solids: 1/f noise." Rev. Mod. Phys., vol. 53, p. 497, 1981.

[143] S. Bandyopadhyay, M. Cahay, and A. Svizhenko, "Noise in nanoscale devices." In Noise in Physical Systems and 1/f Fluctuations: ICNF, World Scientific Publishing Company Incorporated, 2001.

[144] F. E. Terman, Radio Engineers' Handbook (first ed.), New York, NY: McGraw-Hill, pp. 286–294, 1943.

[145] J. Anaya, J. Jiménez, and T. Rodríguez. Thermal Transport in Semiconductor Nanowires. Rijeka, Croatia: InTechOpen, 2012.

[146] A. I. Boukai, Y. Bunimovich, J. TahirKheli, J. K. Yu, W. A. GoddardIii, J. R. Heath, "Silicon nanowires as efficient thermoelectric materials." Nature, vol. 451,pp. 168–171, 2008.

[147] A. I. Hochbaum, R. Chen, R. D. Delgado, W. Liang, E. C. Garnett, M. Najarian, A. Majumdar, P. Yang, "Enhanced thermoelectric performance of rough silicon nanowires." Nature, vol. 451, pp. 163–167, 2008.

[148] J. Garg, N. Bonini, and N. Marzari, "High thermal conductivity in short-period superlattices." Nano lett., vol. 11, pp. 5135-5141, 2011.

[149] M. Hu, and D. Poulikakos, "Si/Ge superlattice nanowires with ultralow thermal conductivity." Nano lett., vol. 12, pp. 5487-5494, 2012.

[150] S. Liu, X. Xu, R. Xie, G. Zhang, B. Li, "Anomalous heat conduction and anomalous diffusion in low dimensional nanoscale systems." Eur. Phys. J. B, vol.85, p.1, 2012.

[151] D. Li, Y. Wu, P. Kim, L. Shi, P. Yang, A. Majumdar, "Thermal conductivity of individual silicon nanowires." Appl. Phys. Lett., vol. 83, p. 2934, 2003.

[152] L. Yin, E. K. Lee, J. W. Lee, D. Whang, B. L. Choi, C. Yu, "The influence of phonon scatterings on the thermal conductivity of SiGe nanowires." Appl. Phys. Lett., vol. 101, p. 043114, 2012.

[153] J. A. Martinez, P. P. Provencio, S. T. Picraux, J. P. Sullivan, B. S. Swartzentruber, "Enhanced thermoelectric figure of merit in SiGe alloy nanowires by boundary and hole-phonon scattering." . J. Appl. Phys., vol. 110, p. 074317, 2011.

[154] H. Kim, Y.-H. Park, I. Kim, J. Kim, H.-J. Choi, W. Kim, "Effect of surface roughness on thermal conductivity of VLS-grown rough SiGe nanowires." Appl. Phys. A: Mater. Sci. Process., vol. 104, p. 23, 2011.

[155] M. Shelley, A. A. Mostofi, "Prediction of high ZT in thermoelectric silicon nanowires with axial germanium heterostructures." Europhys. Lett., vol. 94, p. 67001, 2011.

[156] E. K. Lee, L. Yin, Y. Lee, J. W. Lee, S. J. Lee, J. Lee, S. N. Cha, D. Whang, G. S. Hwang, K. Hippalgaonkar, A. Majumdar, C. Yu, B. L.Choi, J. M. Kim, K. Kim, "Large thermoelectric figure-of-merits from SiGe nanowires by simultaneously measuring electrical and thermal transport properties." Nano Lett., vol. 12, p. 2918, 2012.

[157] D. B. Migasand V. E. Borisenko, "Structural, electronic, and optical properties of ⟨001⟩-oriented SiGe nanowires." Phys. Rev. B, vol. 76, p. 035440, 2007.

[158] R. Peköz, O. B. Malcıoğlu, J.-Y. Raty, "First-principles design of efficient solar cells using two-dimensional arrays of core-shell and layered SiGe nanowires." Phys. Rev. B, vol. 83, p. 035317, 2011.

[159] G. E. Jellison, T. E. Haynes, and H. H. Burke. "Optical functions of silicon-germanium alloys determined using spectroscopic ellipsometry." Opt. Mater., vol. 2, pp. 105-117, 1993.

[160] E. D. Palik, Handbook of optical constants of solids, Chicago, IL: Academic press, 1998.

[161] M. N. Wybourne, Properties of Silicon, EMIS Data Review Series 4, London, England: INSPEC, 1988.

[162] S. Perkowitz, Optical characterization of semiconductors: infrared, Raman, and photoluminescence spectroscopy, San Diego, CA: Elsevier, 2012.

[163] Q. Lu, K. W. Adu, H. R. Gutierrez, G. Chen, K.-Ke. Lew, P. Nimmatoori, X. Zhang, E. C. Dickey, J. M. Redwing, and P. C. Eklund. "Raman scattering from $Si_{1-x}Ge_x$ alloy nanowires." J. Phys. Chem. C, vol. 112, pp. 3209-3215, 2008.

[164] B. Dietrich, E. Bugiel, J. Klatt, G. Lippert, T. Morgenstern, H. J. Osten, and P. Zaumseil, "Measurement of stress and relaxation in $Si_{1-x}Ge_x$ layers by Raman line shift and x-ray diffraction." J. Appl. Phys., vol. 74, p. 3177, 1993.

[165] http://www.bls.gov/iif/oshwc/osh/case/ostb1023.pdf. (accessed on 08/29/2016).

[166] P. M. Fauchet, Monolithic silicon light sources, L. Pavesi and D. J. Lockwood, Eds., Si Photonics, New York, NY: Springer, 2003, p. 177.

[167] K. N. Shinde, S.J. Dhoble, H.C. Swart, K. Park, Phosphate Phosphors for Solid-State Lighting, Berlin Heidelberg: Springer Science & Business Media, 2012.

[168] http://www.bls.gov/iif/oshwc/osh/case/ostb1023.pdf. (accessed on 08/03/2016)

[169] G. Grupp et. al., "Peak Firing Temperature Dependence of the Microstructure of Ag Thickfilm Contacts on Silicon Solar Cells." 20th EPSEC, Barcelona, Spain, June 2005.

[170] J. Jeong, et al., "Enhanced silicon solar cell performance by rapid thermal firing of screen printed metals." Electron Devices, IEEE 48, Issue 12 Dec. 2001, pp. 2836-2841.

[171] M. M. Hilali and A. Rohatgi, "A review and understanding of screen-printed contacts and selective emitter formation." 14th Workshop on Crystalline Silicon Solar Cells and Modules, vol. 1617, pp. 80401-3393 2004.

[172] K. Brunner, "Si/Ge nanostructures." Rep. Prog. Phys., vol. 65, p. 27, 2001.

[173] B. V. Kamenev, L. Tsybeskov, J-M. Baribeau, and D. J. Lockwood. "Photoluminescence and Raman scattering in three-dimensional Si/Si1-xGex nanostructures." Appl. Phys. Lett., vol. 84, pp. 1293-1295, 2004.

[174] L. Tsybeskov, L., K. L. Moore, D. G. Hall, and P. M. Fauchet. "Intrinsic band-edge photoluminescence from silicon clusters at room temperature." Phys. Rev. B, vol. 54, p. R8361, 1996.

[175] N. Modi, D. J. Lockwood, X. Wu, J-M. Baribeau, and L. Tsybeskov. "Excitation wavelength dependent photoluminescence in structurally non-uniform Si/SiGe-island heteroepitxial multilayers." J. Appl. Phys., vol. 111, p. 114313, 2012.

[176] L. Tsybeskov, and D. J. Lockwood. "Silicon-germanium nanostructures for light emitters and on-chip optical interconnects." Proc. IEEE, vol. 97, pp. 1284-1303, 2009.

[177] R. R. Reeber, and Kai Wang. "Thermal expansion and lattice parameters of group IV semiconductors." Materials Mater. Chem. Phys., vol. 46, pp. 259-264, 1996.

[178] M. I. Alonso, and K. Winer. "Raman spectra of c-$Si_{1-x}Ge_x$ alloys." Phys. Rev. B, vol. 39, p. 10056, 1989.

[179] F. Cerdeira, W. Dreybrodt, and Manuel Cardona. "Resonant Raman scattering in germanium." Solid State Commun., vol. 10, pp. 591-595, 1972.

[180] B.-I., Moshit, and F. Patolsky. "From crystalline Germanium–silicon axial heterostructures to silicon nanowire–nanotubes." Nano lett., vol. 12, pp. 1121-1128, 2012.

[181] C. Mouchet, L. Latu-Romain, C. Cayron, E. Rouviere, C. Celle, and J. P. Simonato, "Growth of one-dimensional Si/SiGe heterostructures by thermal CVD." Nanotechnol., vol. 19, p. 335603, 2008.

[182] M. Hanke, C. Eisenschmidt, P. Werner, N. D. Zakharov, F. Syrowatka, F. Heyroth, P. Schäfer, and O. Konovalov. "Elastic strain relaxation in axial Si/Ge whisker heterostructures." Phys. Rev. B, vol. 75, pp. 161303, 2007.

[183] Y. Wang, V. Schmidt, S. Senz, and U. Gösele. "Epitaxial growth of silicon nanowires using an aluminium catalyst." Nat. Nanotechnol., vol. 1, pp. 186-189, 2006.

[184] S. Sharma, T. I. Kamins, and R. Stanley Williams. "Diameter control of Ti-catalyzed silicon nanowires." J. Cryst. Growth, vol. 267, pp. 613-618, 2004.

[185] P. M. Mooney, F. H. Dacol, J. C. Tsang, and J. O. Chu. "Raman scattering analysis of relaxed Ge_xSi_{1-x} alloy layers." Appl. Phys. Lett., vol. 62, pp. 2069-2071, 1993.

[186] S. Nakashima, T. Mitani, M. Ninomiya, and K. Matsumoto. "Raman investigation of strain in Si/SiGe heterostructures: Precise determination of the strain-shift coefficient of Si bands." J. Appl. Phys., vol. 99, p. 053512, 2006.

[187] A. S. Nikolenko, "Temperature dependence of raman spectra of silicon nanocrystals in oxide matrix." Ukr. J. Phys., vol. 58, pp. 980-986, 2013.

[188] H. H. Burke, and I. P. Herman. "Temperature dependence of Raman scattering in Ge $1-$ x Si x alloys." Phys. Rev. B, vol. 48, p. 15016, 1993.

[189] T. R. Hart, R. L. Aggarwal, and B. Lax, "Temperature dependence of Raman scattering in silicon." Phys. Rev. B, 1, p. 638, 1970.

[190] J. Menéndez and M. Cardona, "Temperature dependence of the first-order Raman scattering by phonons in Si, Ge, and $\alpha-$ S n: Anharmonic effects." Phys. Rev. B, vol. 29, p. 2051, 1984.

[191] R. Gupta, Q. Xiong, C. K. Adu, U. J. Kim, and P. C. Eklund. "Laser-induced Fano resonance scattering in silicon nanowires." Nano Lett., vol. 3, pp. 627-631, 2003.

[192] A. P. Knights, and J. D. B. Bradley. "Optical Detection Technologies for Silicon Photonics." Silicon Photonics: The State of the Art, pp. 191-227, 2008.

[193] E. Anastassakis, A. Pinczuk, E. Burstein, F. H. Pollak, and M. Cardona, "Raman scattering under uniaxial stress." Solid State Comm., vol. 8, p. 133, 1970.

[194] S. Adachi, Sadao. Properties of semiconductor alloys: group-IV, III-V and II-VI semiconductors, John Wiley & Sons, 2009.

[195] W. K. Liu, and M. B. Santos, Thin Films: Heteroepitaxial Systems, Singapore, Singapore: World Scientific, 1999.

[196] S. Pathak, and V. B. Shenoy, "Size dependence of thermal expansion of nanostructures." Phys. Rev. B, vol. 72, p. 113404, 2005.

[197] B. A. Weinstein and G. J. Piermarini, "Raman scattering and phonon dispersion in Si and GaP at very high pressure." Phys. Rev. B, vol. 12, p. 1172, 1975.

[198] S. H. Wei and A. Zunger, "Predicted band-gap pressure coefficients of all diamond and zinc-blende semiconductors: Chemical trends." Phys. Rev. B, vol. 60, p. 5404, 1999.

[199] P. Y. Yu, and Manuel Cardona, Fundamentals of Semiconductors: Physics and Materials Properties. 3rd rev. & enl. ed., eBook Series: Advanced texts in physics, 2001.

[200] J. Humlicek, and E. Kasper. Properties of Strained and Relaxed Silicon Germanium, London, UK: INSPEC, the Institute of Electrical Engineers, 1995.

[201] P. Lautenschlager, P. B. Allen, and M. Cardona, "Temperature dependence of band gaps in Si and Ge." Phys. Rev. B, vol. 31, p. 2163, 1985.

[202] K. P. O'Donnell, X. Chen, "Temperature dependence of semiconductor band gaps." Appl. Phys. Lett., vol. 58, pp. 2924-2926, 1991.

[203] S. Adachi, Optical properties of crystalline and amorphous semiconductors: Materials and fundamental principles. Springer Science & Business Media, 2012.

[204] Y. Wang, Z.-Q. Wang, and J.-G. Lv. "Size-dependent thermal buckling of heated nanowires with ends axially restrained." Phys. Lett. A, vol. 378, pp. 899-903, 2014.

[205] S. Saha, and A. R. Md Ali. "Thermal buckling and postbuckling characteristics of extensional slender elastic rods." J. Mech. Eng., vol. 40, pp. 1-8, 2009.

[206] J. S. Temenoff, and A. G. Mikos. Biomaterials: the intersection of biology and materials science, Upper Saddle River, NJ: Pearson Prentice-Hall, 2014.

[208] S. Reza, G. Bosman, M. S. Islam, T. I. Kamins, S. Sharma, R. S. Williams, "Noise in silicon nanowires." IEEE Trans. Nanotechnol., vol. 5, pp. 523-529, 2006.

[209] G. Giacomelli, M. Giudici, S. Balle, J. R. Tredicce, "Experimental evidence of coherence resonance in an optical system." Phys. Rev. Lett., vol. 84, p. 3298, 2000.

[210] V. V. Sherstnev, A. Krier, A. G. Balanov, N. B. Janson, A. N. Silchenko, P. V. McClintock, "Mid-infrared lasing induced by noise." Fluct. Noise Lett., vol. 3, pp. L91-L95, 2003.

[211] G. Konstantatos, E. H. Sargent, "Nanostructured materials for photon detection." Nat. Nanotechnol., vol. 5, pp. 391-400, 2010.

[212] G. Stegemann, A. G. Balanov, E. Schöll, "Noise-induced pattern formation in a semiconductor nanostructure." Phys. Rev. E, vol. 71, p. 016221, 2005.

[213] F. N. Hooge, T. G. M. Kleinpenning, L. K. J. Vandamme, "Experimental studies on 1/f noise." Rep. Prog. Phys, vol. 44, p. 479, 1981.

[214] R. H. Baek, C. K. Baek, H. S. Choi, J. S. Lee, Y. Y Yeoh, K. H. Yeo, Y. H. Jeong, "Characterization and modeling of 1/noise in Si-nanowire FETs: effects of cylindrical geometry and different processing of oxides." IEEE Tran. Nanotech., vol. 10, pp. 417-423, 2011.

[215] S. Kim, S. Kim, D. B. Janes, S. Mohammadi, J. Back, M. Shim, "DC modeling and the source of flicker noise in passivated carbon nanotube transistors." Nanotech., vol. 21, p. 385203, 2010.

[216] D. Lynall, K. Byrne, A. Shik, S. V. Nair, H. E. Ruda, "Surface properties from transconductance in nanoscale systems." Nano Lett., vol. 16, pp. 6028-6035, 2016.